



Politecnico di Bari

Repository Istituzionale dei Prodotti della Ricerca del Politecnico di Bari

Advancements in Control, Design, and Parameter Identification of Permanent Magnet Synchronous Machines

This is a PhD Thesis

Original Citation:

Advancements in Control, Design, and Parameter Identification of Permanent Magnet Synchronous Machines / Brescia, Elia. - ELETTRONICO. - (2022). [10.60576/poliba/iris/brescia-elia_phd2022]

Availability:

This version is available at <http://hdl.handle.net/11589/237899> since: 2022-04-16

Published version

DOI:10.60576/poliba/iris/brescia-elia_phd2022

Publisher: Politecnico di Bari

Terms of use:

(Article begins on next page)



Department of Electrical and Information Engineering
ELECTRICAL AND INFORMATION ENGINEERING

Ph.D. Program

SSD: ING-IND/32–CONVERTERS, ELECTRICAL
MACHINES AND DRIVES

Final Dissertation

Advancements in Control, Design, and Parameter Identification of Permanent Magnet Synchronous Machines

by

Elia Brescia

Supervisor:

Prof. Francesco Cupertino

Prof. Giuseppe L. Cascella

Coordinator of Ph.D. Program:

Prof. Mario Carpentieri

Course n°34, 01/11/2018-28/02/2022



LIBERATORIA PER L'ARCHIVIAZIONE DELLA TESI DI DOTTORATO

Al Magnifico Rettore
del Politecnico di Bari

Il/la sottoscritto/a Brescia Elia nato a Putignano il 19/02/1992, residente a Monopoli in via Rimembranze n.11, e-mail elia.brescia@outlook.it, iscritto al 3° anno di Corso di Dottorato di Ricerca in Ingegneria Elettrica e dell'Informazione, ciclo XXXIV ed essendo stato ammesso a sostenere l'esame finale con la prevista discussione della tesi dal titolo:
Advancements in Control, Design, and Parameter Identification of Permanent Magnet Synchronous Machines

DICHIARA

- 1) di essere consapevole che, ai sensi del D.P.R. n. 445 del 28.12.2000, le dichiarazioni mendaci, la falsità negli atti e l'uso di atti falsi sono puniti ai sensi del codice penale e delle Leggi speciali in materia, e che nel caso ricorressero dette ipotesi, decade fin dall'inizio e senza necessità di nessuna formalità dai benefici conseguenti al provvedimento emanato sulla base di tali dichiarazioni;
- 2) di essere iscritto al Corso di Dottorato di ricerca ___ Ingegneria Elettrica e dell'Informazione ___ ciclo ___XXXIV___, corso attivato ai sensi del "Regolamento dei Corsi di Dottorato di ricerca del Politecnico di Bari", emanato con D.R. n.286 del 01.07.2013;
- 3) di essere pienamente a conoscenza delle disposizioni contenute nel predetto Regolamento in merito alla procedura di deposito, pubblicazione e autoarchiviazione della tesi di dottorato nell'Archivio Istituzionale ad accesso aperto alla letteratura scientifica;
- 4) di essere consapevole che attraverso l'autoarchiviazione delle tesi nell'Archivio Istituzionale ad accesso aperto alla letteratura scientifica del Politecnico di Bari (IRIS-POLIBA), l'Ateneo archiverà e renderà consultabile in rete (nel rispetto della Policy di Ateneo di cui al D.R. 642 del 13.11.2015) il testo completo della tesi di dottorato, fatta salva la possibilità di sottoscrizione di apposite licenze per le relative condizioni di utilizzo (di cui al sito <http://www.creativecommons.it/Licenze>), e fatte salve, altresì, le eventuali esigenze di "embargo", legate a strette considerazioni sulla tutelabilità e sfruttamento industriale/commerciale dei contenuti della tesi, da rappresentarsi mediante compilazione e sottoscrizione del modulo in calce (Richiesta di embargo);
- 5) che la tesi da depositare in IRIS-POLIBA, in formato digitale (PDF/A) sarà del tutto identica a quelle **consegnate**/inviata/da inviarsi ai componenti della commissione per l'esame finale e a qualsiasi altra copia depositata presso gli Uffici del Politecnico di Bari in forma cartacea o digitale, ovvero a quella da discutere in sede di esame finale, a quella da depositare, a cura dell'Ateneo, presso le Biblioteche Nazionali Centrali di Roma e Firenze e presso tutti gli Uffici competenti per legge al momento del deposito stesso, e che di conseguenza va esclusa qualsiasi responsabilità del Politecnico di Bari per quanto riguarda eventuali errori, imprecisioni o omissioni nei contenuti della tesi;
- 6) che il contenuto e l'organizzazione della tesi è opera originale realizzata dal sottoscritto e non compromette in alcun modo i diritti di terzi, ivi compresi quelli relativi alla sicurezza dei dati personali; che pertanto il Politecnico di Bari ed i suoi funzionari sono in ogni caso esenti da responsabilità di qualsivoglia natura: civile, amministrativa e penale e saranno dal sottoscritto tenuti indenni da qualsiasi richiesta o rivendicazione da parte di terzi;
- 7) che il contenuto della tesi non infrange in alcun modo il diritto d'Autore né gli obblighi connessi alla salvaguardia di diritti morali od economici di altri autori o di altri aventi diritto, sia per testi, immagini, foto, tabelle, o altre parti di cui la tesi è composta.

Luogo e data _____ 12/04/2022 _____

Firma _____ 

Il/La sottoscritto, con l'autoarchiviazione della propria tesi di dottorato nell'Archivio Istituzionale ad accesso aperto del Politecnico di Bari (POLIBA-IRIS), pur mantenendo su di essa tutti i diritti d'autore, morali ed economici, ai sensi della normativa vigente (Legge 633/1941 e ss.mm.ii.),

CONCEDE

- al Politecnico di Bari il permesso di trasferire l'opera su qualsiasi supporto e di convertirla in qualsiasi formato al fine di una corretta conservazione nel tempo. Il Politecnico di Bari garantisce che non verrà effettuata alcuna modifica al contenuto e alla struttura dell'opera.
- al Politecnico di Bari la possibilità di riprodurre l'opera in più di una copia per fini di sicurezza, back-up e conservazione.

Luogo e data _____ 12/04/2022 _____

Firma _____ 



Politecnico
di Bari

Department of Electrical and Information Engineering
ELECTRICAL AND INFORMATION ENGINEERING

Ph.D. Program

SSD: ING-IND/32–CONVERTERS, ELECTRICAL
MACHINES AND DRIVES

Final Dissertation

Advancements in Control, Design, and Parameter Identification of Permanent Magnet Synchronous Machines

by

Elia Brescia



Referees:

Prof. Davide Barater

Prof. Christopher Gerada

Supervisor:

Prof. Francesco Cupertino

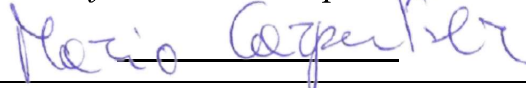


Prof. Giuseppe Cascella



Coordinator of Ph.D Program:

Prof. Mario Carpentieri



Course n°34, 01/11/2018-28/02/2022

Extended Abstract (en)

In this work, advancements in control, design, and parameter identification of permanent magnet synchronous machines (PMSMs) are presented. These advancements take up opportunities and challenges offered by novel applications and technologies. In fact, PMSMs are increasingly adopted thanks to high efficiency and versatility, covering a wide range of applications. In particular, the use of PMSMs in the industry of small-scale wind turbines is becoming dominant. In this application, direct drive topologies coupled with variable speed and fixed pitch wind turbines are a promising solution because of their simplicity, efficiency, and reliability. In fact, this solution avoids the use of gearboxes and mechanical systems for the control of the pitch angle, reducing losses, costs, and failure risks. In this architecture, the aerodynamic power regulation is entirely entrusted to the control of the permanent magnet synchronous generator (PMSG). While several methods have been developed to achieve the maximum power point tracking, poor effort has been made to regulate the power for wind speeds above the rated one. In this work, this challenge has been addressed by proposing an innovative control scheme in which an aerodynamic torque observer and a wind speed estimator are involved. The aim of the designed solution is to achieve the maximum power point tracking for wind speeds below the rated one and to extend the power generation in the high wind speed region. In this region, the respect of the safety mechanical limits of the system is the crucial issue. The proposed control scheme has been tested on an experimental setup in the laboratory of Electrical Machines and Drives of the Politecnico di Bari. The achieved results show that the reference power regulation characteristic has been tracked with a good accuracy covering the whole wind speed range of the system.

In the context of the design of PMSMs, novel modular topologies are gaining increasing interest, especially in applications where large machines are

employed. Thanks to this technology, several advantages in the manufacturing, transporting, and assembling over conventional PMSMs can be achieved. A drawback of PMSMs with modular stators is the presence of additional harmonic components of the cogging torque, with higher amplitudes and lower frequencies than the ones of PMSMs with a one-piece stator. The minimization of these harmonics is essential to increase the control accuracy and reduce undesired noise and vibrations. Despite several methods have been developed for the cogging torque minimization, these mostly deal with conventional PMSMs. In this work, two novel methods to minimize the cogging torque of modular PMSMs are proposed and compared. Both analytical studies and heuristic procedures are adopted to solve the problem. Simulation results with the finite element method have been presented to validate the proposed methods. The results achieved exhibit a reduction of the cogging torque over 90% and show that conventional methods used for one-piece stator PMSMs are not effective against the additional harmonic components produced by modular stators.

Also, the spread of the IoTs (Internet-of-Things), edge and cloud computing technologies offers novel perspectives on the monitoring and maintenance of PMSMs. Although data-driven approaches can be considered dominant in this context thanks to the availability of big data, the potential of model-based approaches has not been considered and exploited in this novel scenario. Model-based approaches are based on the parameter identification of the system. Many well-known solutions have been developed to identify the parameters of PMSMs, but these are not feasible in large-scale applications because these are not designed for straight-through processing where the human component is negligible and IoTs and edge-cloud computing can give their best. Therefore, in the present work, the problem of the automated parameter identification processing data produced by the PMSM drive without ad-hoc tests or control actions is considered. This problem has been addressed by means of the design of an innovative algorithm based on coupled Adaline Neural Networks. Data

produced by the PMSM during its ordinary operations are used to feed the Adaline Neural Networks. Moreover, an analytical study has been performed for the convergence and estimation errors analysis of the proposed algorithm. Finally, simulation and experimental investigations have been performed for verification purposes. The results achieved show a good accuracy of the parameter identification, with experimental estimation errors lower than 15% without any manual action.

Keywords

Adaline neural networks, Artificial neural networks, Cogging torque, Finite element analysis, Genetic algorithm, Modular stators, Parameter identification, Permanent magnet synchronous machines, Segmented stators, Small wind turbines, Surrogate models, Variable-speed fixed-pitch wind turbines.

Extended Abstract (it)

In questo lavoro sono presentati avanzamenti nella progettazione, controllo e identificazione parametrica di macchine sincrone a magneti permanenti, cogliendo le opportunità e le sfide offerte da tecnologie e applicazioni innovative. Infatti, tali macchine sono impiegate in misura crescente in diversi campi di applicazione grazie alla loro elevata efficienza e versatilità. In particolar modo, la scelta di queste macchine sta diventando dominante nell'industria delle piccole turbine eoliche. In questa applicazione, macchine direttamente accoppiate a turbine eoliche a velocità variabile e angolo di pitch fisso sono considerate una promettente soluzione per la semplicità, efficienza e affidabilità del sistema. Infatti, questa soluzione evita l'uso di trasmissioni e sistemi meccanici per il controllo dell'angolo di pitch, riducendo perdite, costi e rischi di guasto. In questa architettura, la regolazione della potenza aerodinamica è interamente affidata al controllo del generatore sincrono a magneti permanenti. Mentre il problema di massimizzare la potenza prodotta è stato ampiamente affrontato con diversi metodi, il problema della regolazione della potenza per velocità del vento superiori a quella nominale non ha ricevuto la stessa attenzione. Nel presente lavoro, questo problema è stato trattato proponendo uno schema di controllo innovativo che include un osservatore della coppia aerodinamica ed uno stimatore della velocità del vento. L'obiettivo dello schema progettato è duplice: massimizzare la potenza aerodinamica per velocità del vento fino a quella nominale ed estendere la capacità di produrre energia per velocità superiori a quella nominale, rispettando i limiti meccanici di sicurezza del sistema. Lo schema di controllo proposto è stato testato mediante un setup sperimentale presso il laboratorio di Macchine e Azionamenti Elettrici del Politecnico di Bari. I risultati ottenuti mostrano che la curva di riferimento di regolazione della potenza è stata rispettata con una buona precisione nell'intero range di velocità del vento.

Nell'ambito della progettazione delle macchine sincrone a magneti permanenti, le topologie modulari stanno riscuotendo un crescente interesse, specialmente nelle applicazioni in cui sono impiegate macchine di taglia elevata. Grazie alla tecnologia modulare possono essere conseguiti numerosi vantaggi in termini di produzione, trasporto e assemblaggio rispetto alle topologie convenzionali. Un inconveniente delle topologie modulari è costituito dalla presenza di componenti armoniche aggiuntive della coppia di cogging, caratterizzate da ampiezze più elevate e frequenze più basse rispetto a quelle presenti in topologie con statore intero. Minimizzare queste armoniche è di fondamentale importanza per incrementare la precisione del controllo e ridurre rumori e vibrazioni indesiderate. Nonostante siano stati sviluppati diversi metodi per minimizzare la coppia di cogging, questi sono per lo più concepiti per macchine convenzionali. Pertanto, nel presente lavoro sono proposti e confrontati due metodi innovativi per minimizzare la coppia di cogging di macchine modulari. Sia studi analitici che procedure euristiche sono stati impiegati per risolvere tale problema mentre sono state effettuate simulazioni con il metodo degli elementi finiti per testare e validare le soluzioni proposte. I risultati ottenuti sulle macchine ottimizzate mostrano una riduzione della coppia di cogging superiore al 90% e dimostrano che metodi convenzionali usati per macchine con statore intero non sono efficaci nei confronti delle componenti armoniche aggiuntive causate da statori modulari.

Un'altra problematica presa in considerazione in questo lavoro è il monitoraggio e la manutenzione delle macchine sincrone a magneti permanenti. A tal proposito, la diffusione di tecnologie Internet-of-Things, Edge and Cloud Computing offre nuove ed interessanti prospettive. Mentre gli approcci cosiddetti "data-driven" possono essere considerati dominanti in questo scenario tecnologico grazie alla disponibilità dei big data, il potenziale di approcci alternativi "model-based" non è stato ancora adeguatamente considerato. Tali approcci richiedono l'identificazione parametrica del sistema. Sebbene

parecchie soluzioni siano disponibili per identificare i parametri di tali macchine, queste risultano poco praticabili in applicazioni su larga scala, dove i vantaggi forniti dalle tecnologie IoT e edge-cloud computing sono più evidenti e l'intervento di operatori umani deve essere limitato. Dunque, nel presente lavoro è stato considerato il problema dell'identificazione parametrica automatizzata di macchine sincrone a magneti permanenti sotto l'ipotesi di utilizzare dati ottenuti senza prove di laboratorio o azioni di controllo specifiche. Questo problema è stato affrontato progettando un algoritmo innovativo basato su reti neurali Adaline accoppiate e alimentate da dati ottenuti durante l'ordinario funzionamento delle macchine. È stato svolto uno studio analitico per analizzare la convergenza e gli errori di stima dell'algoritmo proposto e sono stati effettuati test in simulazione e sperimentali per verificare le prestazioni. I risultati mostrano una buona accuratezza dell'identificazione parametrica, con errori sperimentali inferiori al 15% senza alcun intervento manuale.

Choose a job you love, and you will never have to work a day in your life

Confucius

Acknowledgments

During my PhD course I had the privilege to work with many people and I wish to warmly thank them, starting with my tutor, Prof. Francesco Cupertino. First of all, I thank him for accepting me as his PhD student, and for always offering me his human and scientific support, despite his burdensome task as Rector of the Politecnico di Bari. His human and technical skills deeply motivated me to start and continue this experience. I am grateful to Prof. Leonardo Cascella for the method he taught and the time he spent for my training. Also, I thank him for the opportunity he gave me to approach the industrial world, which enhanced my professional skills. Finally, I wish to thank him for his support beyond academic matters, making me feel part of the team. I warmly thank Prof. Vito Monopoli, who supported me in research and publications, expressing his concern about my career and future. A heartfelt gratitude goes to Rinaldo Consoletti, who has always been friendly and helpful. I thank him for his teachings about the laboratory equipment and his inevitable irony.

Then, I wish to thank all the researchers of the Laboratory of Electrical Machines and Drives, with whom I worked and spent time in these years: Paolo Massenio, Marco Palmieri, Simone Borreggine, Gianvito Gallicchio, Donatello Costantino e Federico Marzo. Also, I thank the students with whom I performed part of the activities and studies presented in this thesis: Gioacchino Tricarico, Diego Calabrese, Donatello Costantino, Donato Facchini, Federico Marzo e Giovanni Rotondi. I am grateful to the group of Arol SpA Bari for the work done together. I thank Mauro di Nardo for the recent collaboration and for providing experimental data used for studies reported in this thesis. I am grateful to the referees for agreeing to evaluate my thesis.

I deeply thank my parents and my sister, who laid eyes on my experience with concern and participation. I am lucky to have them by my side.

Finally, I want to thank Viviana who always believed in me, cheering me unconditionally. Everything would have been harder without her.

Ringraziamenti

Nel corso del mio dottorato ho avuto il privilegio di lavorare a contatto con tante persone e desidero qui ringraziarle con affetto partendo dal mio tutor, il prof. Francesco Cupertino. Sono a lui innanzitutto grato per avermi accolto e come studente di dottorato. Nonostante il suo gravoso incarico come Rettore del Politecnico di Bari si è sempre mostrato disponibile nell'offrirmi il suo supporto umano e scientifico. Le sue doti umane e tecniche mi hanno profondamente motivato ad intraprendere questo percorso. Voglio ringraziare il prof. Leonardo Cascella per tutto ciò che mi ha insegnato in questi tre anni, per il metodo che mi ha trasmesso e per il tempo dedicato alla mia formazione. Lo ringrazio anche per l'opportunità che mi ha concesso di confrontarmi con il mondo aziendale, offrendomi una formazione completa anche dal punto di vista della gestione dei progetti. Lo ringrazio infine per aver manifestato il suo supporto anche al di là delle questioni professionali, facendomi sentire a pieno titolo parte del team. Ringrazio con affetto anche il prof. Vito Monopoli, che mi ha supportato nella ricerca e nelle pubblicazioni manifestando in più occasioni la sua premura nei confronti del mio percorso e futuro professionale. Rivolgo un caro ringraziamento anche all'Ing. Rinaldo Consoletti, che si è dimostrato un amico e un collega sempre disponibile in ogni occasione. Lo ringrazio per tutto ciò che ho imparato da lui sulla strumentazione di laboratorio e per la sua immancabile ironia.

Desidero poi ringraziare tutti gli altri ricercatori del laboratorio di Macchine e Azionamenti Elettrici con cui ho avuto modo di collaborare, confrontarmi e condividere del tempo in questi anni: Paolo Massenio, Marco Palmieri, Simone Borreggine, Gianvito Gallicchio, Donatello Costantino e Federico Marzo. Ringrazio i tesisti con cui ho svolto buona parte del lavoro presentato in questa tesi: Gioacchino Tricarico, Diego Calabrese, Donatello Costantino, Donato Facchini, Federico Marzo e Giovanni Rotondi. Ringrazio anche tutto il gruppo

di ricerca di Arol SpA Bari per l'amicizia ed il lavoro fatto assieme. Ringrazio Mauro Di Nardo per la recente collaborazione e per aver condiviso dei dati sperimentali utilizzati per attività di ricerca riportate in questa tesi. Ringrazio anche i revisori per aver accettato di valutare la mia tesi.

Ringrazio la mia famiglia, i miei genitori e mia sorella, che hanno seguito con premura e partecipazione il mio percorso, sostenendomi nei momenti più delicati e gioendo dei miei traguardi. Sono fortunato ad avere loro al mio fianco.

Ringrazio infine Viviana che ha sempre creduto in me, appoggiandomi incondizionatamente. Senza di lei sarebbe stato tutto più difficile.

Contents

1. Introduction	1
1.1. Permanent Magnet Synchronous Machines: Market, Novel Applications, Opportunities, and Challenges.	1
1.2. Goals and Outlines	4
1.3. The Methodology	4
1.4. Publications	6
2. Control of Permanent Magnet Synchronous Generators Fully Embedded in Small Ducted Wind Turbines in an Extended Wind Speed Range	8
2.1. Introduction and State of the Art	8
2.2. System Description	12
2.2.1. Ducted Wind Turbine	12
2.2.2. Annular Permanent Magnet Synchronous Generator	16
2.2.3. Power Conversion Stage	17
2.3. Control Scheme Description	17
2.3.1. Variable Structure Controller	18
2.3.2. Aerodynamic Torque Observer	23
2.3.3. Pulse-Width Modulation	24
2.3.4. Wind Speed Estimation	25
2.4. Experimental Results	29
2.4.1. Test Rig Overview	29
2.4.1. Results	31
2.5. Final considerations	38

2.6. Publications	39
3. Cogging Torque Minimization of Modular PMSM	40
3.1. Introduction and State of the Art	40
3.2. Cogging Torque of Modular PMSMs	44
3.3. The Case Study	45
3.4. Cogging Torque Minimization Based on the Stator Tooth Tips Topological Optimization	49
3.4.1. Theoretical Study and Design Formula	49
3.4.2. Topological Optimization of the Tooth Tips Shape	54
3.4.3. Heuristic Solution Based on Genetic Algorithm and Artificial Neural Networks Surrogate Models	56
3.4.4. Results	61
3.5. Cogging Torque Minimization Based on the Stator Tooth Tips Sinusoidal Shaping	76
3.5.1. Theoretical Study and Design Formula	76
3.5.2. Formulation of the Optimization Problem	77
3.5.3. Heuristic Solution	79
3.5.4. Results	80
3.6. Final considerations	85
3.7. Publications	86
4. Automated offline parameter identification of PMSMs	87
4.1. Introduction and State of the Art	87
4.2. PMSM Model with Actuation Delay	90
4.3. Proposed Automated Offline Parameter identification	92
4.3.1. SPMSM Steady-States Identification	92
4.3.2. Identification of the q -Axis Inductance	94

4.3.3. Identification of the Rotor Flux Linkage and Stator Resistance	96
4.3.4. Convergence Analysis	98
4.3.5. Analysis and Minimization of the Estimation Errors	100
4.4. Simulation Results	104
4.5. Experimental Results	113
4.6. Final Considerations	122
4.7. Publications	123
5. Conclusions and Future Developments	124
A. Nomenclature	126
B. Mathematical Model of the PMSM	131
C. Wind Speed Estimator	133
References	138

1. Introduction

1.1. Permanent Magnet Synchronous Machines: Market, Novel Applications, Opportunities, and Challenges.

There are about 8 billion electric motors in use in the EU, consuming about 50% of the electrical energy produced in the EU [1]. The global induction motor market reached a value of USD 17.5 billion in 2020 [2] while the global PMSM market was valued at USD 12.85 billion in the same year. This market is expected to grow at a Compound Annual Growth Rate (CAGR) of 7.4% over the period 2021 - 2026 [3]. The growth of the PMSM market is supported by the two following important factors.

- High efficiency and throughput: these motors ensure higher efficiency, power factor and power density than induction motors. Moreover, these motors cover a wide range of applications: factory automations, consumer goods, office automations, residential and commercial sector, energy sector, automotive, lab equipment's, medical equipment's, and military and aerospace.
- Electric vehicles are expected to boost the growth of the PMSM market. In 2020 the global electric car stock hit the 10 million mark, a 43% increase over 2019 [4]. In the same year, PMSMs shared the 77% of the electrical car motor market, while wound rotor motors and induction motors shared only the 6% and 17%, respectively [5]. With the leading automotive companies increasingly adopting permanent magnet motors into EVs, the global demand of PMSMs is expected to increase, further driving the market growth over the 2021-2026 period [6]. While there has been much publicity and technical development towards rare-earth reduction in vehicle motors, in practice the market is seeing an increase in the number of permanent magnet motors. In recent years, there has

been an increased shift towards more permanent magnet-based motors: 2019 saw this increase to 82% compared to 79% in 2015 (percentage of passenger cars using PMSMs) [7].

In such context of increasingly adoption of PMSMs, the advent of innovative technologies and applications offers novel challenges and opportunities in the design, control, modeling, condition monitoring, and maintenance. A sector in which the use of PMSMs is becoming dominant is the industry of small-scale wind generators [8]. Here, direct drive topologies, where the gearbox between the turbine and the shaft of the generator is omitted, can be considered the focus of researchers [9]-[15]. A low torque pulsation is essential for this application. Moreover, to further simplify the system, the use of fixed-pitch and variable-speed wind turbines is gaining increasing interest in this sector [16]-[19]. In this novel application, the wind turbine power regulation can be achieved only by means of the speed regulation of the PMSM. In this context, the design of control algorithms of the PMSM to achieve a maximum power point tracking and to extend the power generation capability over a wide wind speed range can be considered a challenging issue.

In the same context of wind energy and in other applications in which PMSMs with a large diameter are employed, the adoption of unconventional modular (segmented) PMSMs topologies has gained increasing attention [20], [21]. Compared to conventional one-piece-stator PMSMs, the modular technology ensures the reduction of material wastage, simplicity of the stator winding process, ease of transportation and assembling, etc., advantages particularly noticeably when large PMSMs are adopted. However, in the literature, the modular topology has also been proposed and studied for low power and small size PMSMs, as in [22]-[24]. Moreover, emerging studies have investigated the performances of these topologies and to derive accurate mathematical models [21]-[30], highlighting the importance of the topic. A

drawback of the modular stator structure is the introduction of additional harmonic components of the cogging torque, an undesired pulsation of the torque produced by PMSMs also at no-load condition, which causes vibrations, acoustic noise, and speed pulsations. The minimization of these harmonic components can be considered a novel challenge poorly addressed by the research community, despite the effort made in the study of modular PMSMs.

The development and spread of Internet-of-Things, Edge and Cloud Computing technologies also offers novel perspectives on the condition monitoring and maintenance of PMSMs. Crucial is the availability of resources to store and process the huge amount of data produced by electric drives. This potential leads to novel approaches that can overcome the limitations of conventional algorithms executed by the control software applications of the electric drives. Some manufacturers had already developed IoT-, Cloud-, and Big Data-based health management platforms in the field of electric drives used in the railway (Alstom, Bombardier, Siemens Mobility, Hitachi, CAF), elevators (KONE, Thyssenkrupp Elevator, Otis), and wind power (Siemens Gamesa, Vestas) sectors [31]. In this context, the dominant approach is the data-driven condition monitoring and fault diagnosis making use of Machine and Deep Learning. However, the model-based approaches, in which mathematical models replicate the physical behavior of the real system, can offer additional advantages if paired with the data-driven analysis. The parameter identification for the use of mathematical models is essential. Despite several techniques have been developed to identify the parameters of PMSMs, these rely on ad hoc laboratory tests or in proper control actions, such as the perturbation of the PMSM operating conditions. In the context considered, the main challenge is to identify the PMSM parameters exploiting the availability of the data produced without specific tests or control actions.

1.2. Goals and Outlines

Considering the challenges and motivations in the previous section, this work is structured as follows:

- in the chapter 2, a new solution to the control of a PM synchronous generator fully embedded in a small ducted wind turbine over and wide speed range is described;
- in the chapter 3, two different design approaches are proposed for the minimization of the cogging torque of a PMSM with a segmented stator;
- in the chapter 4 a straight-through-processing solution to the problem of the automated parameter identification of PMSMs in a cloud computing environment without specific tests or control actions is proposed;
- chapter 5 contains the main conclusions and future developments;
- in appendix A the symbology and acronyms adopted and defined in the main text are summarized for sake of readability;
- in appendix B the mathematical model of the PMSM is reported;
- in appendix C some mathematical proofs about the wind speed estimator are reported.

1.3. The Methodology

Artificial Intelligence, in the forms of Computational Intelligence and Machine Learning, is an instrument increasingly adopted which supports in many stages and fields the work of the design and research engineer. In particular, the use of Artificial Intelligence is crucial in problems where explicit mathematical models and solutions can be difficult or impossible to derive. Design optimization, observers and estimators, parameter tuning, and surrogate models are only some examples of the application of the Artificial Intelligence in the context of the design and control of PMSMs. However, the costs of this

instrument, i.e., computational time and resources, can be unsustainable if the problem to be solved is not adequately defined and formulated. In this case, human intelligence and the value of domain knowledge and expertise play a fundamental role.

In the present work, both Computational Intelligence and Machine Learning have been employed to address issues in the design, control, and parameter identification of PMSMs. The use of such instruments has been supported and integrated with results achieved by means of theoretical studies. In the chapter 2, a Shallow Neural Network is employed to estimate the wind speed. In this case, an analytical study has been performed to properly select the inputs of the neural network, ensuring good performances and reducing the computational requirements. In the chapter 3, a genetic algorithm and multilayer neural network-based surrogate models are used to optimize the PMSM design and minimize the cogging torque. In this case, the optimization problem has been partially solved by means of a theoretical study, ensuring the reduction of the design variables and, therefore, of the computational time required by the metaheuristic optimization. Finally, in the chapter 4, an algorithm based on two coupled Adaline Neural Networks is proposed to identify the parameter of the PMSM. In this case, an analytical study has been performed to derive a convergence criterion of the proposed algorithm. Moreover, an additional logic based on the domain knowledge has been adopted to properly choose the PMSM operating conditions used to feed the Adaline Neural Networks and to minimize the estimation errors.

To validate the proposed methods and solutions, both simulation and experimental results are presented. In the chapter 2, tests performed on an experimental setup in the laboratory of Electrical Machines and Drives of the Politecnico di Bari are presented. Instead, in the chapter 3, simulation results achieved with the finite element analysis are shown. In this case, to evaluate the

robustness of the proposed solution against the manufacturing errors, an extended analysis with the finite element method introducing manufacturing tolerances has been presented. Finally, in the chapter 4, both data provided by simulation and experimental tests have been used to feed the Adaline Neural Networks. The simulation tests have been performed using a PMSM drive modeled in Simulink environment. Instead, the experimental data have been kindly provided by the University of Nottingham using a custom high-speed PMSM drive.

1.4. Publications

Part of the contents and results presented in this thesis have been published in the following journals and conference papers.

Journals

1. D. Calabrese, G. Tricarico, E. Brescia, G. L. Cascella, V. G. Monopoli and F. Cupertino, "Variable Structure Control of a Small Ducted Wind Turbine in the Whole Wind Speed Range Using a Luenberger Observer," *Energies*, vol. 13, no.18: 4647, 2020.
2. E. Brescia, D. Costantino, P. R. Massenio, V. G. Monopoli, F. Cupertino and G. L. Cascella, "A Design Method for the Cogging Torque Minimization of Permanent Magnet Machines with a Segmented Stator Core Based on ANN Surrogate Models," *Energies*, vol. 14, no. 7: 1880, 2021.
3. E. Brescia, D. Costantino, F. Marzo, P. R. Massenio, G. L. Cascella and D. Naso, "Automated Multistep Parameter Identification of SPMSMs in Large-Scale Applications Using Cloud Computing Resources," *Sensors*, vol. 21, no. 14: 4699, 2021.

Conferences

1. E. Brescia, M. Palmieri, G. L. Cascella and F. Cupertino, "Optimal Tooth Tips Design for Cogging Torque Suppression of Permanent Magnet Machines with a Segmented Stator Core," *2020 International Conference on Electrical Machines (ICEM)*, 2020, pp. 1930-1936.
2. D. Costantino, E. Brescia, P. R. Massenio, P. Serafino, G. L. Cascella and F. Cupertino, "SuMRAS: a new SPMSM Parameter Identification in Cloud Computing Environment," *2021 IEEE Workshop on Electrical Machines Design, Control and Diagnosis (WEMDCD)*, 2021, pp. 297-302.
3. E. Brescia, P. Serafino, D. Cascella, G. Comitangelo, G. Conte and L. Chieco, "Automated Parameter Identification of SPMSMs Based on Two Steady States Using Cloud Computing Resources," *2021 International Conference on Electrical, Computer and Energy Technologies (ICECET)*, 2021.

2. Control of Permanent Magnet Synchronous Generators Fully Embedded in Small Ducted Wind Turbines in an Extended Wind Speed Range

2.1. Introduction and State of the Art

In recent years, wind energy has been the fastest growing among renewable energy sources [32]. In particular, micro and small wind turbines are an attractive solution for distributed generation in urban areas, self-energy production, and microgrids [32]-[42]. Among these, variable-speed and fixed-pitch (VSFP) wind turbines are the most common because this configuration reduces the complexity and cost of the system [19], [42]-[46]. Moreover, a direct-drive permanent magnet synchronous generator (PMSG) is usually equipped within this type of wind energy conversion system (WECS) because it avoids gearboxes, reduces costs, and increases reliability and efficiency [19], [40], [41], [43], [44].

The aerodynamic power and torque of VSFP WECS can be only regulated by means of the control of the PMSG, due to the absence of the pitch control. For wind speeds lower than the rated one, generally the maximum power point tracking (MPPT) is implemented. The aim of the MPPT is to extract the maximum available aerodynamic power for a given wind speed. In the literature, several MPPT methods for VSFP WECS have been proposed. The first approach is to consider the fluid dynamic model of the wind turbine to provide optimal references for the shaft speed ([18], [42], [47]-[50]), or torque ([19], [40], [51]), and power ([44], [52], [53]). These approaches have the advantage of being fast and stable, but are affected by inaccuracies due to production tolerances, model and parameter uncertainties, and time variance. Moreover, these methods generally require the measurement of wind, shaft speed and torque. To avoid the use of mechanical sensors, many sensorless algorithms have been proposed in

previous studies to achieve the MPPT. For a WECS with a diode rectifier and boost converter, the proposed solution is based on tracking the optimal boost converter voltage on the rectifier side using only voltage and current sensors [42], [44], [49], [53]. Others are based on the use of observers and estimators of shaft speed ([18], [47], [54], [55]), wind speed ([47], [50], [56]-[59]) and aerodynamic torque ([18], [40], [44], [56], [60]-[63]). A robust and parameter-independent approach is based on the perturb and observe concept that is widely treated in the literature in its many variants [41], [43]-[46], [52], [64]-[67]. This approach avoids the use of mechanical sensors and does not require prior knowledge of the WECS because the optimal rotor speed is achieved with a research algorithm performed during the operation of the wind turbine. However, this approach is slower than the first one for tracking the optimal speed, and its accuracy depends on the step size of the P&O algorithm. Finally, an innovative and robust approach was proposed in [68] in which an artificial neural network (ANN) was used to determine the reference shaft speed that maximises power extraction. However, this method requires a period of operation of the WESC in which the ANN has to be trained.

For wind speeds higher than the rated one, the power and torque produced by the wind should be limited to avoid mechanical and electrical failure. Due to the absence of the pitch control, the most common approach used for VSFP WECS operations under high wind speeds is the soft stall method [42], [44]-[46], [52], [69], [70], which reduces the shaft speed to force the turbine to operate below its maximum efficiency. A control strategy alternative to the soft stall method is based on the flux weakening operation of PMSGs connected to a full-bridge PWM rectifiers [19], [40], [71]. This approach differs from the soft stall method, because it is based on operating the WECS at shaft speeds above the rated speed to reduce the power extracted from the wind. The soft stall method has been largely applied to WECSs with a power converter topology consisting of a passive diode rectifier and DC/DC converter [18], [42], [44]-[46], [52], [70].

Instead, very few studies have addressed control at high wind speeds of VSFP WECSs with a PMSG and a three-phase inverter-based back-to-back converter, in case the soft stall method is adopted. This solution, despite its higher costs, is characterised by higher efficiency ([32], [60], [62], [72]) in comparison with the most commonly used topology for small-scale WECS, based on a 3-phase diode rectifier, a DC/DC converter, and a grid-connected three-phase inverter [32], [37], [42], [43].

The operation of the WECS under high wind speeds is performed with a variety of specific aims and solutions, depending on its configuration and operating limits. For example, in [40], the WECS was controlled to limit the generated electrical power to the rated power of the electrical generator. In [42], the machine-side boost converter voltage was limited to a safety value to prevent high wind speed from developing excessive torque at higher rotor speeds. In [19] and [56], for wind speeds above the rated speed, the PMSG was controlled to maximise the electrical power generated by considering the current and voltage constraints. In [44] and [70], after constant-speed stall control, a constant aerodynamic power soft stall control was performed to avoid exceeding the rated power of the turbine. In [45] and [52], after the constant-speed stall operation, the control strategy limited the generated DC power considering the electrical operating limits of the system. In [18], the rated electrical torque, which occurs when the boost converter operates at its rated current, was held until the maximum wind speed at which the generator can counteract the aerodynamic torque was reached. To the best of the author's knowledge, the VSFP WECS was operated with respect to the rated aerodynamic power of the wind turbine at high wind speeds only in [44] and [70]. In these studies, the proposed control strategies performed constant aerodynamic power soft stall control. During this operation, the shaft speed decreased while the aerodynamic torque increased to maintain constant aerodynamic power. With increasing wind speed, this operation can lead to the development of excessive aerodynamic torque. In this

situation, the major risks are the damaging of the wind turbine and the development of an aerodynamic torque that exceeds the electromagnetic torque generable by the PMSG. In this last case, the system becomes uncontrollable leading to a dangerous increase of the rotational speed. However, [44] and [70] did not consider the issue of limiting the aerodynamic torque for safety reasons.

The use of aerodynamic power or torque observers to perform constant aerodynamic power or torque operation is crucial [44], [70]. In the literature, different aerodynamic torque observers (ATOs) have been proposed. In [60]-[62], the aerodynamic torque is estimated by using a sliding-mode observer. A new high-gain robust ATO is proposed in [40]. In [18] and [44] a simple adaptive observer based on an approximated equation of rotational mass equilibrium is proposed. A Luenberger Observer (LO) was proposed in [56] and [63], but these works lack experimental validation. The advantages of using a LO are the ease in modelling operations and the easy way of achieving a fast convergence.

In this work, an original control strategy for a small VSFP ducted horizontal axis wind turbine (DHAWT) equipped with a full-embedded annular PMSG (APMSG) is proposed. The APMSG is grid-connected through a back-to-back connection of two three-phase inverters. A tripartite control scheme based on the soft stall method is proposed for the DHAWT operation under high wind speeds. This operating range is subdivided into constant shaft speed, constant aerodynamic power, and constant aerodynamic torque subregions. To perform this control strategy, a variable structure controller (VSC) combined with an aerodynamic torque LO and a shallow neural network (NN) wind speed estimator (WSE) was designed. This control scheme maximises the power extracted from the wind, which is compatible with the mechanical safety limits of the DHAWT, i.e., the rated shaft speed, rated aerodynamic power, and maximum aerodynamic torque. Therefore, the contributions of this study are as follows: the achievement of the soft stall method with a back-to-back power

converter topology, the operation of the wind turbine once the aerodynamic torque limit is reached, and the experimental validation of a LO.

Experimental tests were conducted in a laboratory setup emulating a ramp wind speed pattern to prove the effectiveness of the proposed control scheme. In the literature, there is no uniformity in the wind speed pattern used for the emulative experimental tests of WECS. The actual measured wind speed patterns were used from [19] and [64], while irregular artificial wind patterns have been adopted from [44], [47], [52] and [62]. Such wind speed patterns allow for analysis of the dynamic performances of the proposed control strategies. However, the use of wind speed patterns with multiple steps ([18], [42], [43], [45], [46], [48], [51], [57]) and single steps or constant speeds ([41], [49], [53], [68]) allows for analysis of the effectiveness of the control scheme in specific wind speed subregions. In this study, a ramp wind pattern was chosen to show the fitting of the actual aerodynamic power and torque with the ideal regulation characteristics over the entire wind speed range. The examination of the dynamic performances of the proposed control scheme was not the purpose of this work.

2.2. System Description

In this section, an overview of the proposed WECS is provided to contextualise the entire study. The system is composed of a DHAWT, an APMSG, and a back-to-back power converter topology, as shown in **Figure 1**.

2.2.1. Ducted Wind Turbine

The DHAWT is shown in **Figure 2**. In these wind turbines, a divergent duct increases the pressure drop across the disk of the rotor. This increases the power production compared to conventional wind turbines [39], [73]. The DHAWT performance improvements allow smaller rotor diameters with the same rated power, favouring rotor rigidity and reducing blade deformations. Moreover, the

adoption of a diffuser reduces the cut-in speed and wind noise compared to conventional ones [74], [75]. In **Table 1**, the most relevant parameters of the DHAWT are considered in this work, which corresponds to the one in [74].

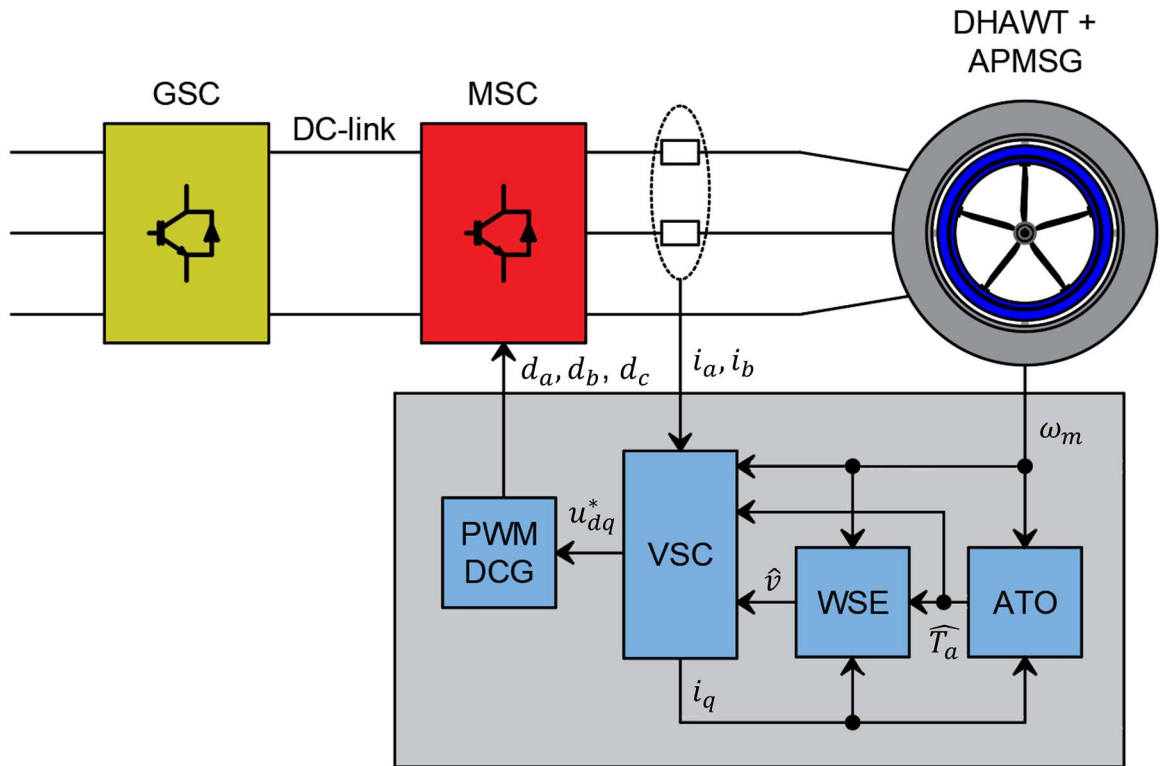


Figure 1. Wind energy conversion system schematic.

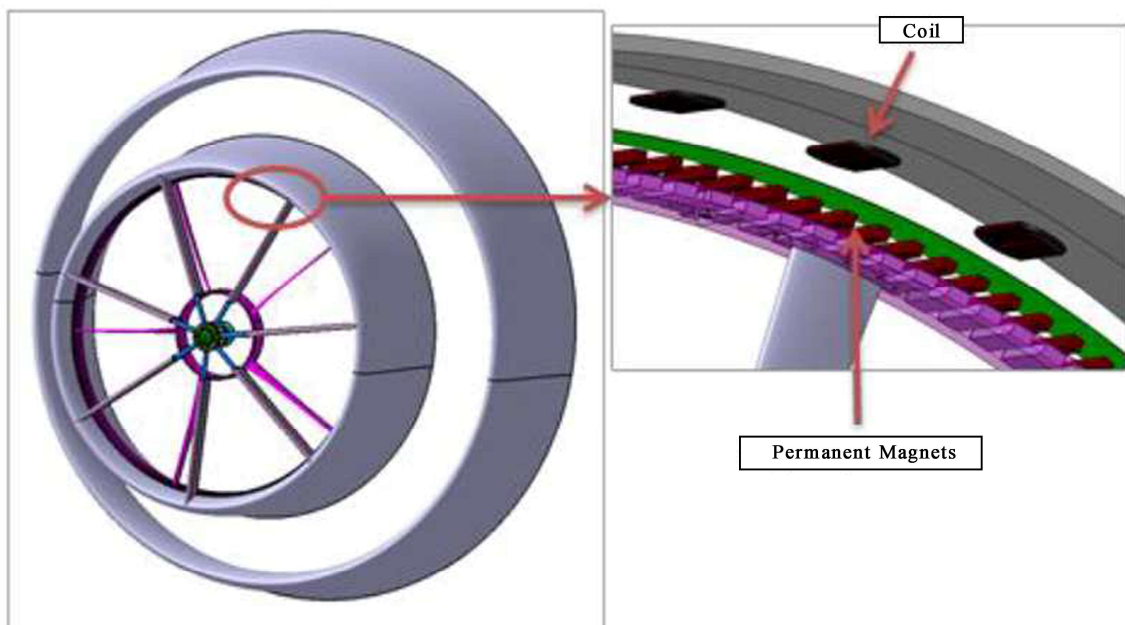


Figure 2. Rendering of the DHAWT-APMSG system.

It can be noted that the maximum value of the power coefficient (C_{pmax}), due to the presence of the diffuser, is characterised by a higher value than that of conventional wind turbines, whose theoretical maximum value, according to Betz's theory, is 16/27. For DHAWTs, this coefficient can overcome the value of 1, as proven in [74]-[76]. To obtain the DHAWT characteristic curve, which expresses the relationship between the power coefficient C_p and the tip-speed ratio (TSR) λ , in [74] a non-conventional approach was used. The flow interacting with the DHAWT was computed using computational fluid dynamics (CFD) simulations. Source terms for the momentum equations were introduced inside the domain swept by the rotor to take the turbine effect on the flow field into account. From the CFD simulation, it is possible to compute the local relative velocity, and from the polar characteristics of the aerodynamic blade profile (with an approach similar to the blade element theory), it is possible to compute the force coefficient to determine the force exchange between the flow and the rotor. Using CFD simulations has improved the computational accuracy of the entire flow field, and hence the computation of the turbine performance. The obtained DHAWT characteristic curve is shown in **Figure 3**. Note that, the value of the TSR that maximizes the power coefficient (λ_{max}) is equal to 6.

Table 1. Ducted wind turbine parameters.

Parameter	Value
P_{rated}	0,5 kW
ω_{rated}	941 rpm
T_{max}	5,9 Nm
R	0,51 m
J	1,193 Kg · m ²
λ_{max}	6
C_{pmax}	1,048

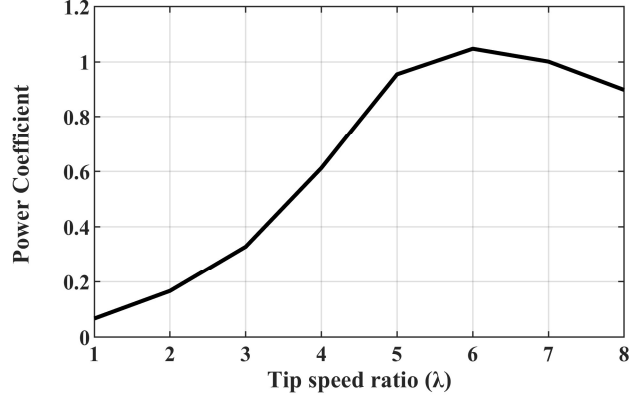


Figure 3. DHAWT characteristic curve.

Regarding the equations used in the model, the aerodynamic reference power used to evaluate the turbine performance is expressed by the following equation:

$$P_w = \frac{1}{2} \rho A_r v^3 \quad (1)$$

where ρ is the air density, A_r is the rotor swept area, and v is the unconstrained wind speed. The aerodynamic power caught by the wind turbine is:

$$P_a = C_p(\lambda) P_w \quad (2)$$

where $C_p(\lambda)$ is the power coefficient which denotes the power conversion efficiency of the wind turbine, which depends on the λ , defined by

$$\lambda = \frac{\omega_m R}{v} \quad (3)$$

where R is the blade tip radius and ω_m is the shaft speed. Replacing (1) in (2), the following expression of P_a is obtained

$$P_a = \frac{1}{2} \rho \pi R^2 C_p(\lambda) v^3 \quad (4)$$

The expression of the aerodynamic torque is obtained by the division between P_a and shaft speed ω_m :

$$T_a = \frac{1}{2} \rho \pi R^2 C_p(\lambda) \frac{v^3}{\omega_m} \quad (5)$$

By replacing ω_m in (5) through (3), a new expression for T_a is achieved:

$$T_a = \frac{1}{2} \rho \pi R^3 C_p(\lambda) \frac{v^2}{\lambda} \quad (6)$$

2.2.2. Annular Permanent Magnet Synchronous Generator

An innovative full-embedded APMSG is considered. This generator was designed in agreement with the method presented in [39]. The purpose of this method is to design a PMSG integrated with a DHAWT, to achieve a target torque with a multi-objective optimisation aimed at minimising the weight of the permanent magnets and copper. The APMSG rotor consists of a fibreglass ring with internal permanent magnets. It is directly connected to the blade tips and is concentric to a segmented iron stator, which is instead embedded on the diffuser (**Figure 2**). Concerning the stator windings, coils are realised on multilayer printed circuit boards and are wye connected. This solution makes the manufacturing and assembly process easier. In **Table 2** all parameters of the APMSG are summarised.

The mathematical model of the APMSG is the same model of a conventional SPMSM, reported in Appendix B. In fact, the ironless rotor of the APMSG can be considered isotropic, like that of a surface PMSM (SPMSM). This is also the

reason why the dq -axis inductances are the same. In this application, the equation (B.6), can be rewritten as

$$T + T_a - T_{av} = J \frac{d\omega_m}{dt} \quad (7)$$

Table 2. APMSG parameters.

Parameter	Value
Rated Power	0,8 kW
Rated Speed	941 rpm
Rated Current	1,55 A
$L_d = L_q$	$1,04 \cdot 10^{-8}$ H
R_s	34,64 Ω
ψ_{PM}	$7 \cdot 10^{-2}$ W _b
n_p	50

2.2.3. Power Conversion Stage

The power conversion stage consists of two power converters in a back-to-back configuration. The APMSG is directly coupled to a machine side converter (MSC), which is connected to a grid side converter (GSC). The MSC is a three-phase full-bridge PWM rectifier whose duty cycles are provided by the proposed control scheme to perform a field-oriented control (FOC). The GSC is a PWM inverter that maintains a constant voltage on the DC-link, and synchronises and controls the output voltages and currents to establish a correct grid connection. Thus, the GSC leads to grid frequency decoupling and transfers the generated power from the DC link to the grid.

2.3. Control Scheme Description

The WECS control scheme shown in **Figure 1** can be gathered in four macro-blocks: the VSC, the ATO, the WSE, and the PWM blocks. The sensors

present in the scheme are the phase current sensors and an optical encoder for the measurement of ω_m .

2.3.1. Variable Structure Controller

The VSC is shown in **Figure 4**. In this scheme, all the symbols under “^” represent estimated variables, while the symbols marked with “*” denote reference variables. This scheme realises a cascading speed-current FOC. A commonly adopted solution for the FOC is based on the use of proportional-integral (PI) controllers for speed and current regulation. This solution is simple and robust, and its effectiveness for the control of WECS with a PMSG and a three-phase full-bridge PWM rectifier MSC has already been demonstrated [47], [58], [61]. The speed controller is a PI regulator with feedforward for the aerodynamic torque disturbance rejection, while the current controllers are simple PI regulators. Therefore, $K_{p\omega}$, $K_{i\omega}$, K_{pd} , K_{id} , K_{pq} , and K_{iq} represent the PI gains of the speed and current control loops, respectively. The q -axis current loop performs torque regulation while the d -axis loop performs the maximum torque per ampere control. The “decoupling factors” block operates the d and q -axis decoupling as follows:

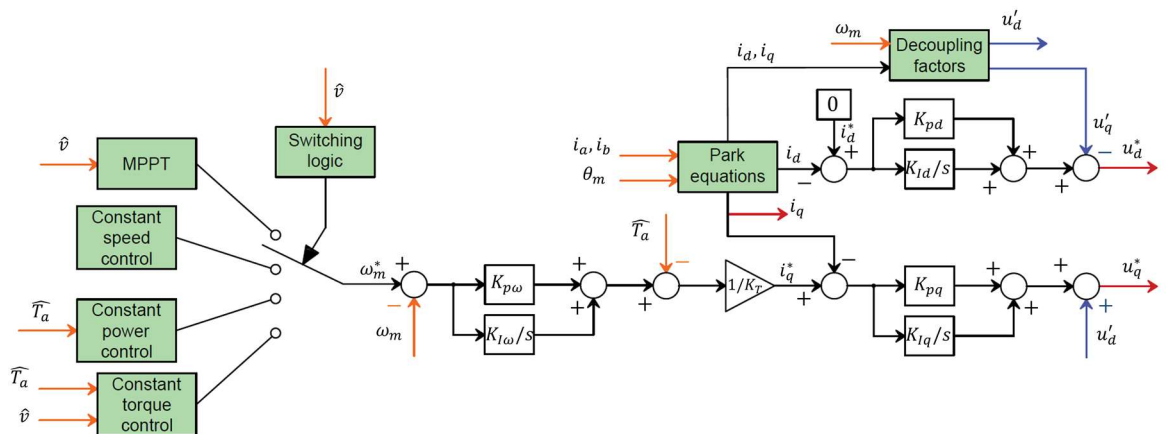


Figure 4. Variable structure controller.

The “decoupling factors” block operates the d and q -axis decoupling as follows:

$$u'_d = n_p \omega_m L_q i_q \quad (8)$$

$$u'_q = n_p \omega_m L_d i_d \quad (9)$$

The “Park equations” block operates the Park transform using the phase currents i_a and i_b and the rotor position θ_m .

The shaft speed reference ω_m^* is provided by four different laws to achieve MPPT control, constant speed control (CSC), constant power control (CPC), and constant torque control (CTC) in four different wind subregions. The shaft speed reference law is selected by the switching logic according to the estimated wind speed value. The aim of the control scheme is to achieve the ideal aerodynamic power curve over the entire wind speed range shown in **Figure 5**. This curve shows the maximum aerodynamic power that can be extracted for a given wind speed, ensuring the respect of the mechanical limits for safe operation of the DHAWT (i.e., rated speed and power and maximum aerodynamic torque). The four control laws and the corresponding wind subregions are summarised in **Table 3** while **Table 4** shows the wind speed threshold values.

Maximum Power- Point Tracking

The MPPT is performed if the wind speed is between the cut-in speed v_{ci} and the wind speed which corresponds to the rated shaft speed v_{spd} (i.e., the low wind speed region). In this work, an approach based on the model of a wind turbine combined with an ANN WSE is proposed. During the MPPT, ω_m^* is provided by a look-up table (LUT), whose input is the estimated wind speed, to maintain the TSR at its optimal value as the wind speed changes. The optimal value of the TSR is the one that maximises C_p ; therefore, it maximises the

extracted wind power, according to (2). This is the well-known optimal tip-speed ratio method. The LUT used for the MPPT control is based on the curve depicted in **Figure 6 (a)**, which is built considering the model of the DHAWT.

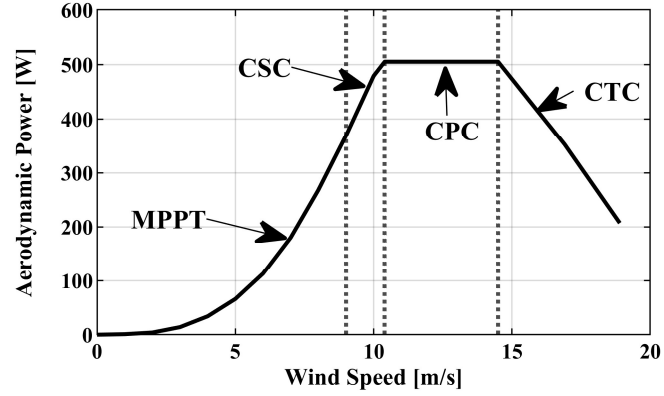


Figure 5. Subregions of the DHAWT operating range.

Table 3. Shaft speed control laws.

Wind Speed Range	Control Law
$v_{ci} < v < v_{spd}$	$\omega_m^* = \omega_{LUT}^*$
$v_{spd} < v < v_{rated}$	$\omega_m^* = \omega_{rated}$
$v_{rated} < v < v_{trq}$	$\omega_m^* = \frac{P_{rated}}{\hat{T}_a}$
$v_{trq} < v < v_{co}$	$\omega_m^* = \frac{T_{max} \omega_{CTC}}{\hat{T}_a}$

Table 4. Wind speed subregion thresholds.

Threshold	Speed [m/s]
v_{ci}	2
v_{spd}	9
v_{pwr}	10,4
v_{trq}	14,5
v_{co}	18,9

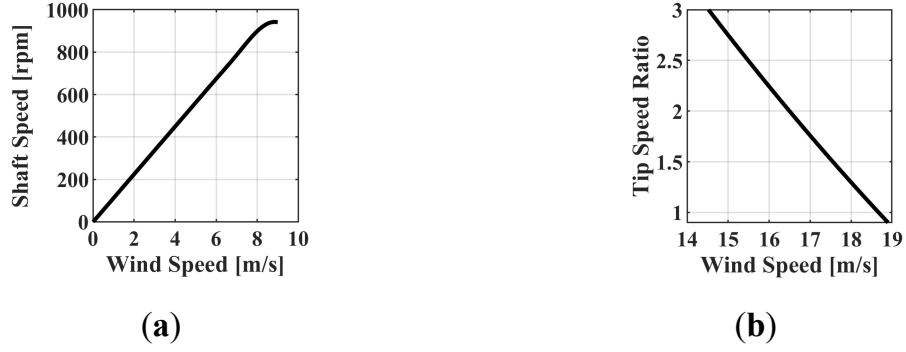


Figure 6. LUTs of the control algorithm: **(a)** Shaft speed reference during MPPT control; **(b)** TSR during CTC.

Operation in the High-Wind Speeds Regions

The CSC is performed for wind speeds above v_{spd} and below the rated speed v_{rated} . Once the rated shaft speed is reached, this should be kept constant to ensure the respect of the speed limit of the DHAWT, and to extract the maximum available power. Therefore, the control law is

$$\omega_m^* = \omega_{rated} \quad (10)$$

By maintaining the shaft speed, the increase in wind speed will increase aerodynamic power, as shown by the ideal regulation characteristic shown in **Figure 7 (a)**. Therefore, the law expressed by (10) is performed until the rated aerodynamic power (P_{rated}) is reached.

The CPC is performed for wind speeds above v_{rated} and below v_{trq} , which is the speed at which the maximum torque is reached. For these wind speeds, a soft stall is performed to limit the aerodynamic power according to the following law:

$$\omega_m^* = \frac{P_{rated}}{\hat{T}_a} \quad (11)$$

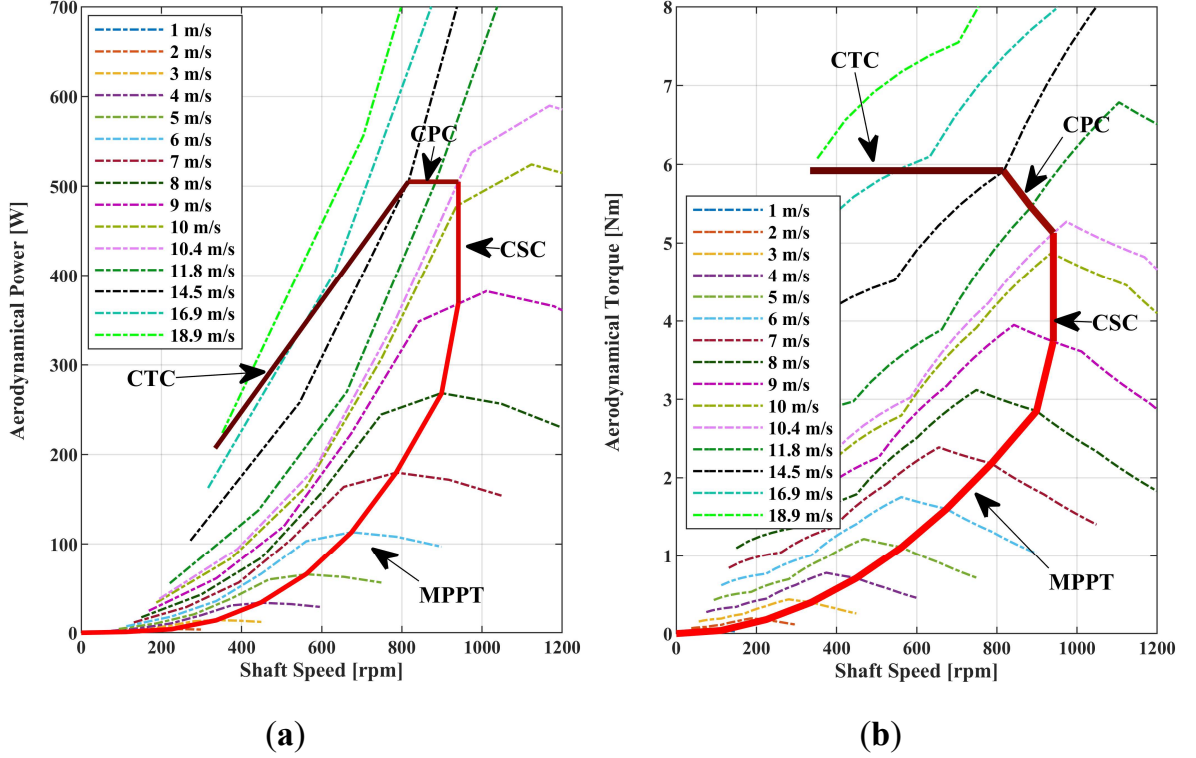


Figure 7. Regulation characteristics: (a) Regulation curve in $\omega_m - P_a$ plane; (b) Regulation curve in $\omega_m - T_a$ plane.

While this control law is applied, the shaft speed decreases while the aerodynamic torque T_a increases, keeping the power constant until the safety torque limit of the DHAWT is reached, as depicted by the ideal regulation characteristics shown in **Figure 7 (b)**.

The maximum aerodynamic torque is reached when the wind speed equals v_{trq} . CTC is performed from this wind speed until the cut-out speed. In this case, the shaft speed reference is

$$\omega_m^* = \frac{T_{max} \omega_{CTC}}{\hat{T}_a} \quad (12)$$

$$\omega_{CTC} = \frac{\lambda^*_{LUT}}{R} \quad (13)$$

where λ_{LUT}^* is computed by an LUT based on the curve depicted in **Figure 6 (b)**. This curve expresses the TSR value that ensures the operation of the DHAWT at the maximum torque as the wind speed changes in the CTC subregion. The ideal power and torque regulation characteristics corresponding to the four control laws described above are illustrated along the fluid dynamic characteristics of the DHAWT in **Figure 7**.

2.3.2. Aerodynamic Torque Observer

To estimate the aerodynamic torque, a LO was adopted. The LO is based on the following linear time-invariant continuous-time reference model:

$$\begin{cases} \dot{\mathbf{z}} = A\mathbf{z} + B\mathbf{u} \\ \mathbf{y} = C\mathbf{z} \end{cases} \quad (14)$$

where:

$$\mathbf{z} = \begin{bmatrix} \omega_m \\ T_a \end{bmatrix}, \mathbf{u} = i_q, A = \begin{bmatrix} 0 & 1 \\ 0 & 0 \end{bmatrix}, B = \begin{bmatrix} K_T \\ J \\ 0 \end{bmatrix}, C = [1 \ 0]$$

This model has been defined considering (7) and (B.5) and by introducing T_a as an exogenous variable, with the following assumptions:

- the dynamic friction losses are negligible ($T_{av} = 0$);
- the derivative of the aerodynamic torque is zero ($\dot{T}_a = 0$).

In this model, \mathbf{z} and \mathbf{y} are the state and measurable outputs of the system, respectively, while \mathbf{u} is the input of the system. The LO is described by the following equations:

$$\begin{cases} \dot{\hat{\mathbf{z}}} = \hat{A}\hat{\mathbf{z}} + \hat{B}\mathbf{u} + L\mathbf{y} \\ \hat{\mathbf{y}} = C\hat{\mathbf{z}} \end{cases} \quad (15)$$

where $\hat{\mathbf{z}}$ and $\hat{\mathbf{y}}$ are the estimations of \mathbf{z} and \mathbf{y} , respectively; \hat{A} , \hat{B} and L are designed to make the estimation error asymptotically converge to zero:

$$\mathbf{e} = \mathbf{z} - \hat{\mathbf{z}} \quad (16)$$

\hat{A} and \hat{B} are designed follows:

$$\hat{A} = A - LC \quad (17)$$

$$\hat{B} = B \quad (18)$$

and by substituting into (15):

$$\dot{\hat{\mathbf{z}}} = A\hat{\mathbf{z}} + B\mathbf{u} + L(\mathbf{y} - C\hat{\mathbf{z}}) \quad (19)$$

Considering (14) and (19), the differential error can be written as

$$\dot{\mathbf{e}} = \dot{\mathbf{z}} - \dot{\hat{\mathbf{z}}} = A\mathbf{e} - LC\mathbf{e} = (A - LC)\mathbf{e} \quad (20)$$

For the error \mathbf{e} to asymptotically converge to zero, the matrix L should be designed to obtain eigenvalues of the matrix $A - LC$ with a negative real part.

2.3.3. Pulse-Width Modulation

The dq -axis voltage references u_d^* and u_q^* provided by the PI current regulators are transformed in the three-phase voltage references u_a^*, u_b^*, u_c^* by

using the Park anti-transformation. These references are used to compute the duty cycles for each leg of the MSC:

$$\begin{aligned}
 d_a &= \frac{u_a^*}{v_{DC}} + 0.5 \\
 d_b &= \frac{u_b^*}{v_{DC}} + 0.5 \\
 d_c &= \frac{u_c^*}{v_{DC}} + 0.5
 \end{aligned} \tag{21}$$

2.3.4. Wind Speed Estimation

The proposed control scheme needs real-time wind speed for the transition between the four control laws and to calculate the shaft speed reference during the MPPT control and CTC. Determining a strategy to estimate the wind speed can be beneficial, instead of using an anemometer, to reduce costs, complexity, and the failure rate of the system [48], [64], [69], [72]. In the literature, different approaches have been proposed for wind speed estimation. In [50] and [57], the method used is based on calculating the wind speed using the inverse model of the wind turbine, and the estimation of the aerodynamic torque and shaft speed. A similar approach was used in [58], wherein the estimated aerodynamic power was used instead of the aerodynamic torque. These model-based methods can be imprecise because of estimation errors of the aerodynamic torque, aerodynamic power, and shaft speed, and because of uncertainties in the wind turbine model. In [59], a support vector machine was used to predict the wind speed. The model was trained to track the wind speed measured by an accurate radar anemometer during a short initial period of the operation of the WECS. In [47] and [56], a three-layer neural network is proposed, whose inputs are the estimated shaft speed and aerodynamic torque/power. The machine learning methods can ensure better results in comparison with those based on the inverse model of the wind turbines but require a training phase in which the wind speed should be

measured. However, as suggested in [59], once the training phase is over, the sensor used for the wind speed measurement can be used for the training with other wind turbines.

In this work, the author proposes a WSE consisting of a shallow NN whose inputs are the estimated aerodynamic torque, the measured shaft speed, and the q -axis current of the APMSG. To demonstrate the superiority of this approach over the model-based WSE, their performances will be compared with experimental tests.

Shallow NN WSE

Figure 8 shows that the WSE consists of an NN whose inputs are, \hat{T}_a , ω_m , and i_q . This is a shallow NN with one hidden layer comprising 10 neurones. The activation function of each neurone is a hyperbolic tangent sigmoid (*tansig*). Each neurone is characterised by biases and weights, which are the coefficients that should be determined with the training process. The inputs of the shallow NN have been chosen on the basis of the study presented in Appendix C. This study demonstrates that the wind speed cannot be expressed as a function only of \hat{T}_a and ω_m due to the presence of aerodynamic torque estimation errors. Instead, there exists a function f_v such as

$$v = f_v(\hat{T}_a, \omega_m, i_q) \quad (22)$$

Thus, the proposed shallow NN can be effectively used to approximate this function.

In a real WECS, this shallow NN should be trained by using the values of the input and output variables registered during a test period in which the WECS is driven by using the proposed control scheme in the whole wind speed range and an anemometer for the wind speed measurement. However, in this study,

instead of using an anemometer on a real DHAWT, the training data were generated with an experimental test on the test rig described in section 2.4.1. This test was performed by emulating the system described in sections 2.2 and 2.3 with a predefined wind speed pattern. The chosen wind speed pattern for the training data generation consists of a uniformly random noise signal that overlaps with a ramp that covers the entire wind speed range of the DHAWT. In this way, the values of the wind speed are known because the wind speed pattern is predefined while the inputs of the shallow NN are based on real measurements performed during the test.

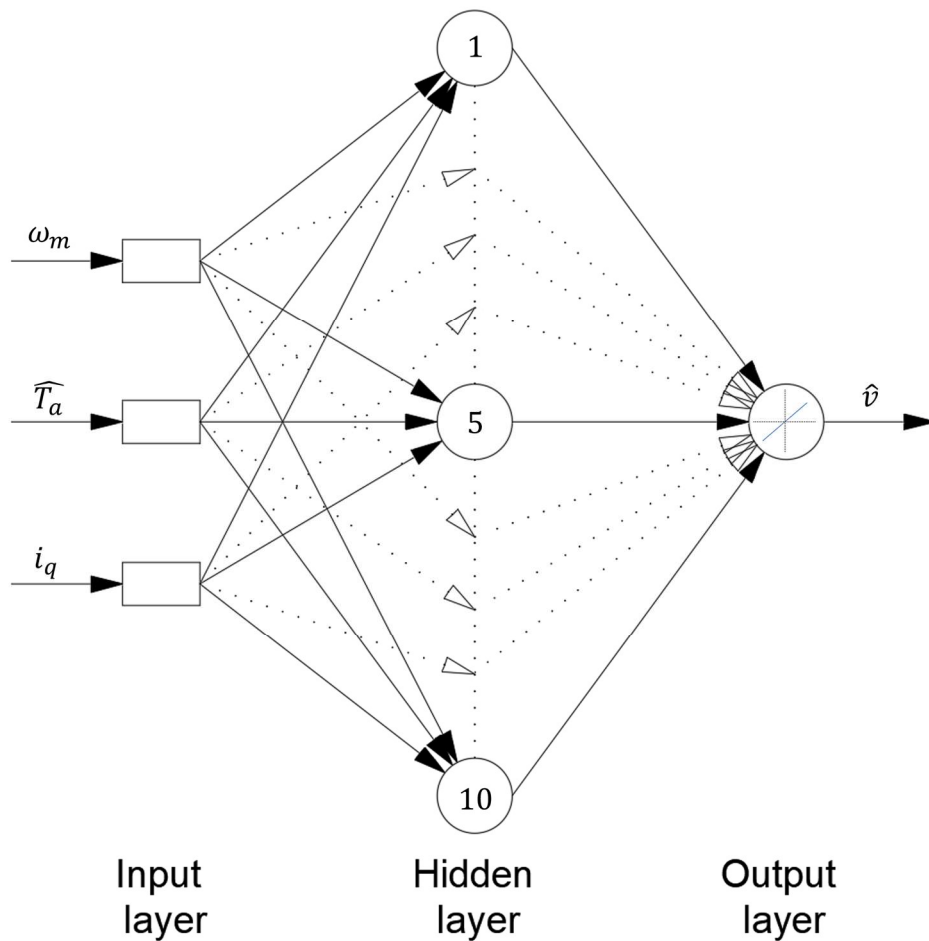


Figure 8. Shallow NN with one hidden layer.

The dataset obtained during the experimental test is approximately 2.3×10^6 samples. However, this experimental dataset was downsampled by a factor of 10 and randomly split into training data, validation data, and test data. These

datasets are made up of 70%, 15%, and 15% of the samples of the whole downsampled experimental dataset. The training dataset is used for determining the weights and biases of the shallow NN to reduce the error between the output of the NN and the wind speed values of the training dataset. To avoid overfitting of the NN, the stop criterion adopted for the training process is based on the maximum validation failures. In this way, the training process stops when the number of consecutive training epochs for which the estimation error of the validation data (*generalisation error*) increases is equal to six. The test dataset is used as an additional verification of the training performance. The Levenberg–Marquardt (LM) algorithm is used to train the NN. This algorithm is known as one of the most efficient training algorithms for small and median size patterns [77]. However, LM implementations require a large amount of available memory because the algorithm is based on the calculation of a Jacobian matrix whose size is proportional to the number of training patterns [77], [78]. In this specific application, the LM algorithm was a good choice to train the NN quickly. The mean squared errors achieved are about 0.0028 on the training, validation, and test datasets, respectively.

Model-based WSE

The model-based approach used in [50] and [57] makes use of the inverse model of the wind turbine. By using (3) and (5) is possible to highlight a relationship between, T_a , ω_m and λ :

$$T_a = \frac{1}{2} \rho \pi R^5 \frac{C_p(\lambda)}{\lambda^3} \omega_m^2 \quad (23)$$

This equation can be rearranged as follows:

$$\frac{C_p(\lambda)}{\lambda^3} = \frac{T_a}{\frac{1}{2} \rho \pi R^5 \omega_m^2} \quad (24)$$

The term $C_p(\lambda)/\lambda^3$ can be computed from (24) by using \hat{T}_a instead of, T_a and the measured shaft speed ω_m . Thus, λ can be determined by exploiting the relationship $C_p(\lambda)/\lambda^3 - \lambda$, as shown in **Figure 9**, for the current DHAWT. Finally, the estimated wind speed is calculated by reversing (3).

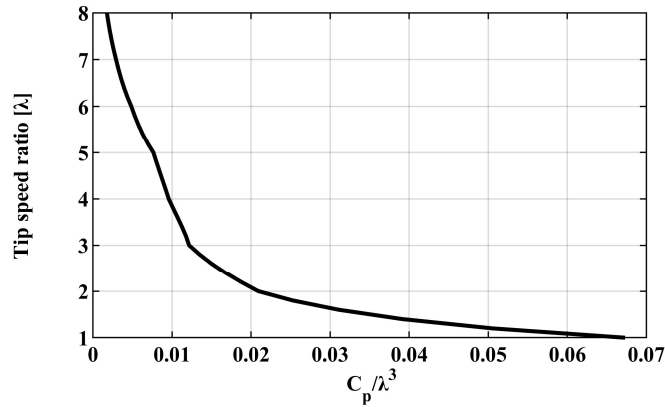


Figure 9. $\frac{C_p}{\lambda^3} - \lambda$ characteristic.

2.4. Experimental Results

2.4.1. Test Rig Overview

The test rig used for the experimental tests is shown in **Figure 10**. A dSPACE MicroLabBox d1202 microcontroller was used to execute the test. The DHAWT emulation was achieved by connecting a commercial induction motor Leporis MS 132S3-2 (which emulates the aerodynamic torque) to a customised edition of the described APMSG, reproduced on a reduced scale. The two electric machines were connected through pulleys and belts. The mechanical losses of this transmission have been considered to emulate the behaviour of a direct connection. The induction motor is driven in torque control mode by a dedicated Mitsubishi FR A800E inverter. Its torque reference is calculated in real time by

adding a mechanical loss torque term to the aerodynamic torque provided by an LUT based on the data of the DHAWT and on (5). The input of this LUT was the actual wind speed and the up-scaled measured shaft speed. Since the APSMG used during the test has rated speed and torque smaller than those of the examined DHAWT, a scaling process was performed. This process acts on the four control laws described in section 2.3.1, which are used for computing the shaft speed reference and the LUT used for the computation of the torque reference of the induction motor. The shaft speed references provided by the four control laws were multiplied by the ratio between the rated speed of the reduced-scale APSMG and of the DHAWT. Moreover, the maximum torque and rated power values used for the CPC and CTC were downscaled with the same logic.

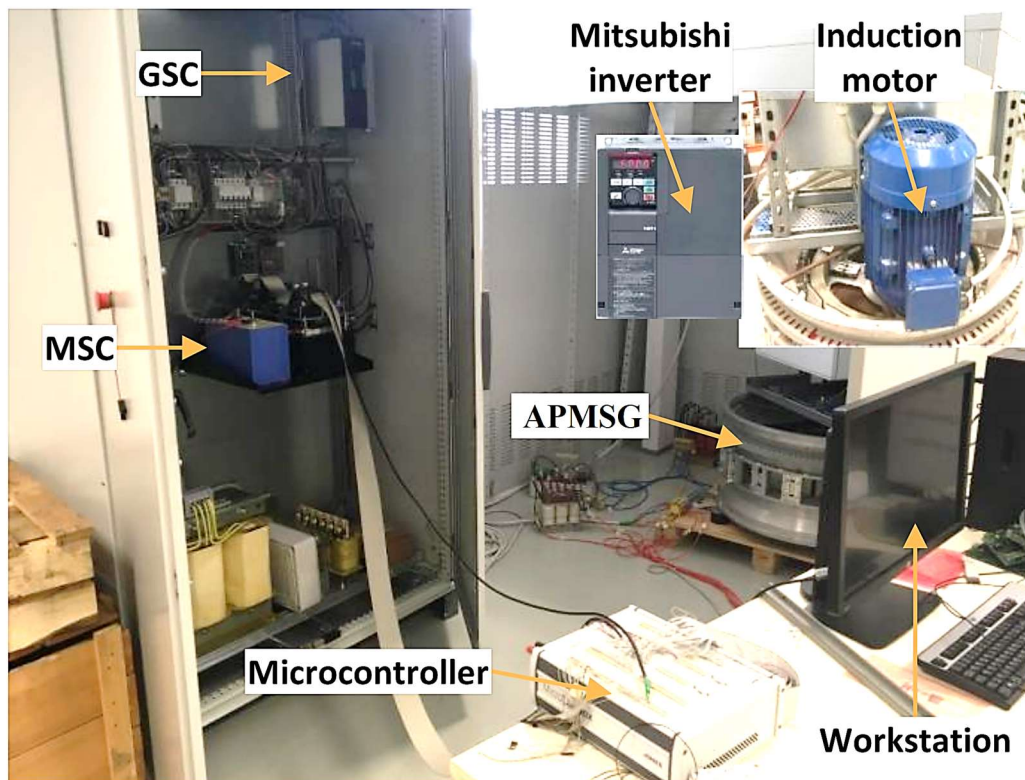


Figure 10. Experimental test rig.

Concerning the induction motor LUT, the shaft speed input is the measured speed of the APSMG multiplied by the inverse of the ratio used for downscaling. Finally, the output of this LUT (aerodynamic torque of the examined DHAWT)

was downscaled. The generator side converter is a custom converter composed of three Semikron SEMiX303GB12E4s modules, each containing two IGBT diodes. The main board of this converter also includes current sensors. The grid-side converter is instead a TDE MACNO OPDE AFE ENERGY S 15, in a custom edition for this rig, and it is set to keep 650 V on the DC-link. **Table 5** summarises the main parameters of the experimental setup, and **Figure 11** shows a scheme with the interconnections between the components of the test rig. The control scheme described in section 2.3 was carried out in a MATLAB-Simulink environment and then uploaded into the microcontroller.

Table 5. Parameters of the experimental setup.

Parameters	Value
APMSG	
Rated Torque	5.5 Nm
Rated Speed	180 rpm
Rated Current	20 A
R_s	0.33 Ω
$L_d = L_q$	0.274 mH
ψ_{PM}	0.013 W_b
n_p	15
J	0.148 $Kg \cdot m^2$
Induction motor	
Rated Speed	2930 rpm
Rated Power	9.2 kW

2.4.1. Results

In this section, the author discusses the experimental results obtained on the test rig. The shaft speed and the aerodynamic torque and power obtained during the tests were scaled up (multiplied by the ratio between the rated values of the DHAWT and APMSG) to compare the results with the ideal regulation curves illustrated in **Figure 6** and **Figure 7**.

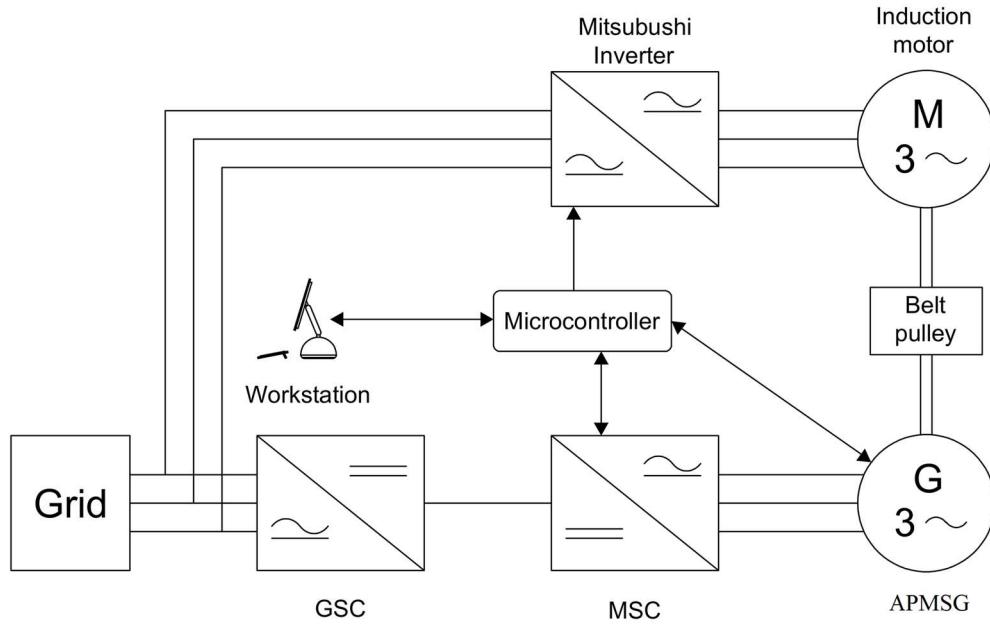


Figure 11. The test rig's architecture.

Figure 12 (a), the actual test wind speed pattern and the wind speed estimated with the model- and NN-based WSEs are shown. **Figure 12 (b)** shows the estimation errors. The actual wind speed pattern was built with a uniformly random noise signal overlapped on a 0.08 slope ramp. An extended operative range was considered, from 2.8 to 18.9 m/s even if the cut-in speed defined above was 2 m/s. The test was accomplished starting from 2.8 m/s to overcome hardware limitations. After a brief initial interval (approximately 35 s), the wind speed ramp started growing until the cut-out speed is reached. Therefore, the test lasted approximately 250 s. The comparison between the WSEs clearly prove the superiority of the proposed NN WSE.

The comparison between the actual and estimated aerodynamic torque is shown in **Figure 13 (a)**, whereas in **Figure 13 (b)**, the relative estimation errors are reported. In these figures, the proposed LO is compared with an adaptive observer proposed in [18]. The observers have very similar dynamics and performances: the maximum error is obtained when the wind speed starts increasing, but when the MPPT subregion is finished, \hat{T}_a becomes very reliable until the cut-out speed is reached. Moreover, the adaptive observer exhibits

better performance than the LO at low torque values, while at high torque values, the situation is reversed. Among the causes of the estimation error that affects both observers, there are uncertainties in the model parameters (K_T and J), inaccuracies in the estimation and compensation of the mechanical losses, and inaccuracies of the torque control of the induction motor. However, this error is acceptable in practise and affects only slightly the performance of the proposed control scheme, as will be shown in the following figures. In conclusion, these results show that the LO can be effectively employed for the estimation of the aerodynamic torque of WECSs as a valid alternative to the adaptive observer proposed in [18].

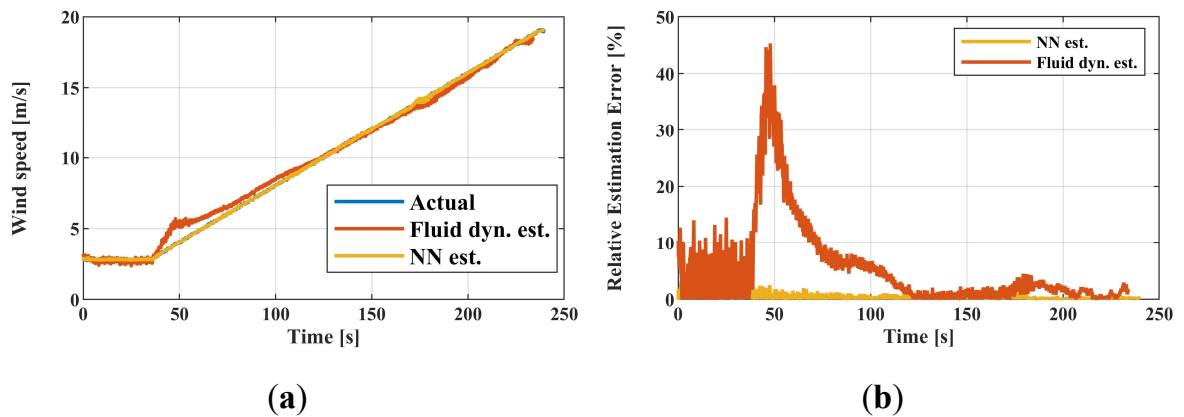


Figure 12. Wind speed: (a) Actual and estimated wind speed pattern; (b) Relative (percentage) estimation errors.

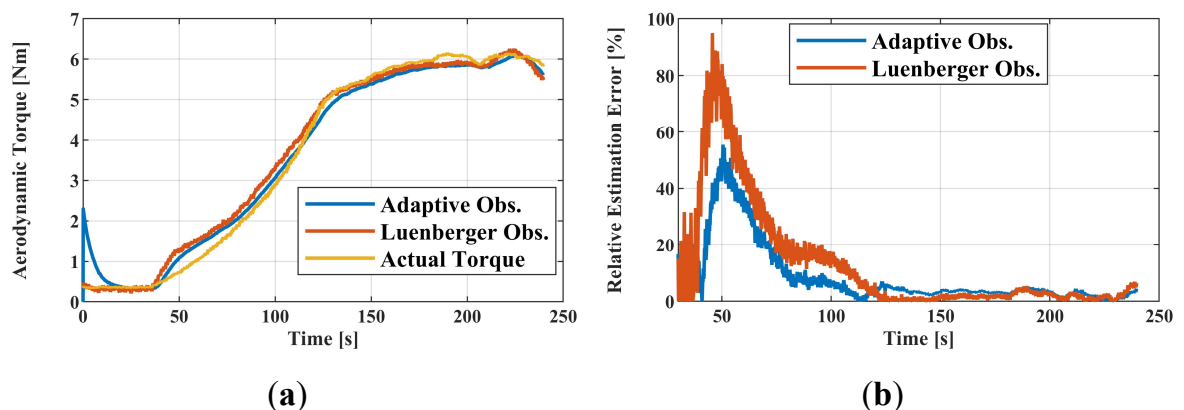


Figure 13. Aerodynamic torque: (a) Actual and estimated aerodynamic torque; (b) Relative (percentage) estimation errors.

The comparison between **Figure 12** and **Figure 13** shows that the estimation of the wind speed with the model-based approach is strongly dependent on the accuracy of the aerodynamic torque estimation. This is particularly evident in the time range between 40 and 60 s. Moreover, **Figure 13 (a)** shows how the actual aerodynamic torque is characterised by an almost constant trend between 180 s and the end of the test. In this time lapse, the wind speed has overcome 14.5 m/s and the CTC achieves a net of small fluctuations.

Figure 14 (a) shows how the measured APMSG rotor speed tracks its reference trajectory very well. The test started with a value of the shaft speed of about 300 rpm; that is the MPPT control reference speed for 2.8 m/s wind speed value. The speed tracking error has also been reported in **Figure 14 (b)**: the tracking error was restricted to a ± 3 rpm range with an average value equal to -0.03 rpm. At the time instant = 110 s, the rated rotor speed was reached, and the control provided a constant rotor speed until the time instant = 130 s, when the rated power was reached. Thus, CSC was achieved. **Figure 15** shows the references and measured d -axis and q -axis currents. The measured currents track the references with some oscillations. To better illustrate the effectiveness of the proposed method, in **Figure 16** and **Figure 17**, the ideal regulation characteristics were compared with the actual scaled ones, depending on rotor speed and wind speed. The actual curves match the ideal ones with a good fit in all wind subregions; therefore, these figures clearly show that the proposed control scheme is effective in all the DHAWT operating ranges. Note that the ideal power curve depicted in **Figure 17** (i.e., the same as in **Figure 5**) cannot be physically exceeded only in the MPPT subregion. In fact, the purpose of the MPPT is to extract the maximum wind power according to the wind turbine conversion efficiency. Thus, in this wind speed subregion, the ideal power curve represents the maximum aerodynamic power that can be physically extracted by the wind turbine. However, in this subregion, the actual aerodynamic power follows the ideal one very precisely. For wind speeds above this subregion, the

ideal power curve represents the maximum power that can be extracted without exceeding the safety mechanical limits. In this case, in the CPC and CTC subregions, the actual power slightly exceeds the ideal one because of the control scheme performance. This is mainly caused by the aerodynamic torque estimation error. In fact, as shown in **Figure 13 (b)**, when the CPC and CTC are performed (after 130 s), the aerodynamic torque estimated by the LO is lower than the actual one. Considering now (11) and (12) because the shaft speed reference is inversely proportional to \hat{T}_a , its value is higher than that achieved without estimation errors. Therefore, the increased shaft speed reference leads the DHAWT to develop an aerodynamic power higher than the ideal one. However, in practise, small deviations are acceptable.

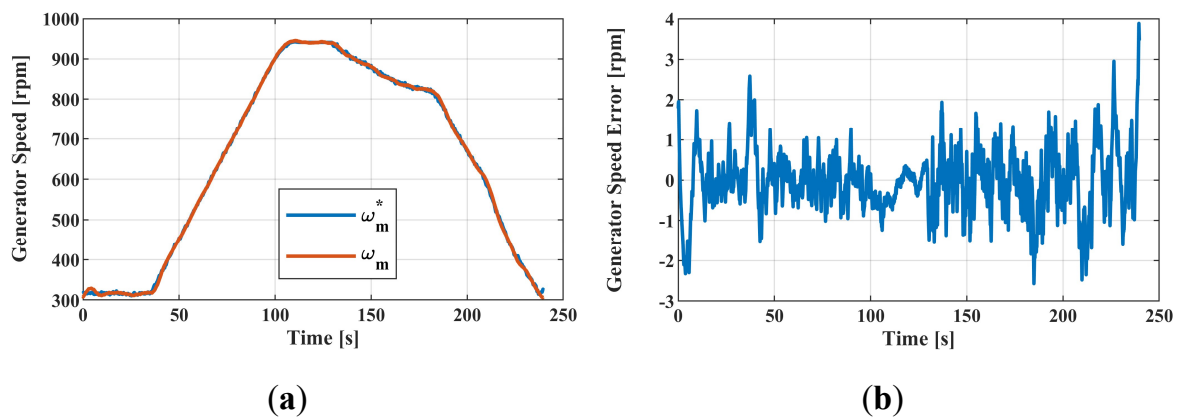


Figure 14. APMSG rotor speed: (a) Speed reference and measured rotor speed; (b) Absolute speed tracking error.

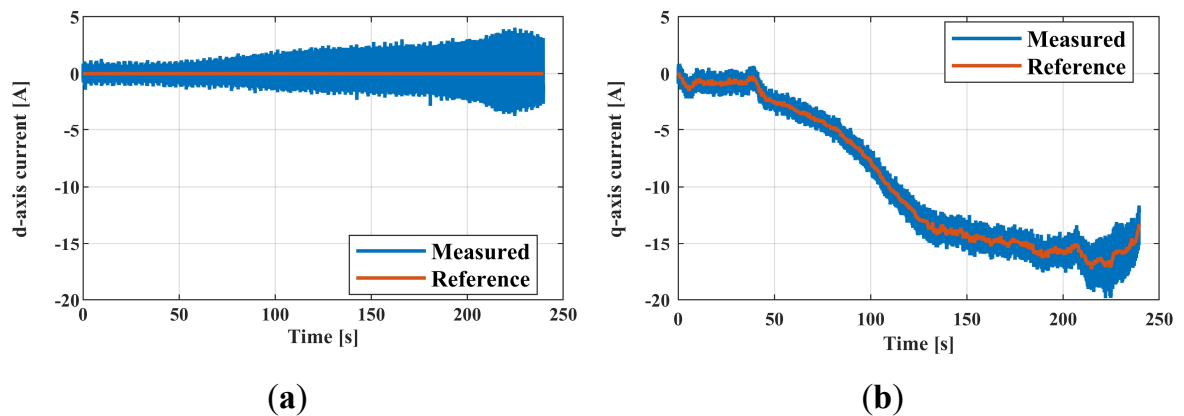


Figure 15. Comparison between reference and measured currents: (a) d -axis current; (b) q -axis current.

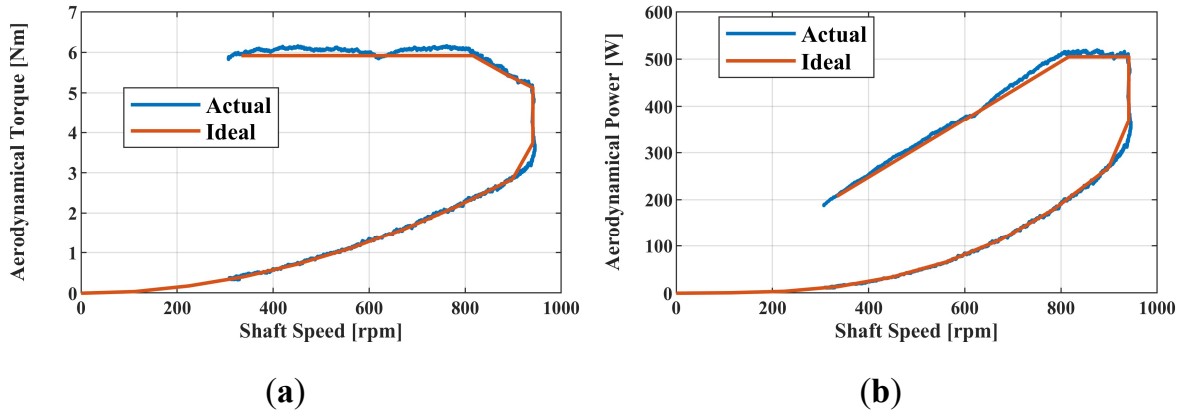


Figure 16. Regulation characteristics comparisons: (a) Ideal and actual aerodynamic torque depending on shaft speed; (b) Ideal and actual aerodynamic power depending on shaft speed.

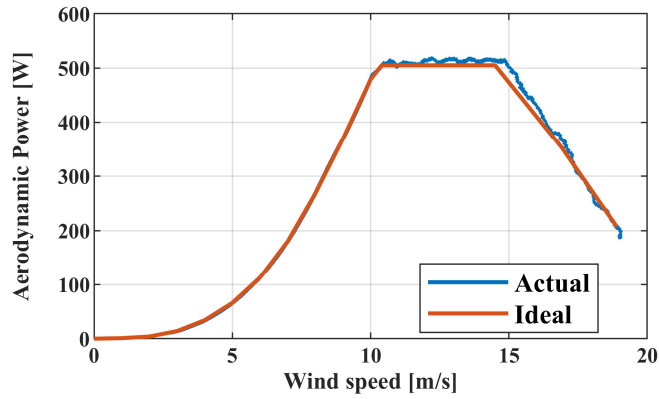


Figure 17. Actual and ideal aerodynamic power curves depending on wind speed.

To the best of the author’s knowledge, the proposed aerodynamic power regulation considering the mechanical constraints of the WECS with a back-to-back power converter topology has not been achieved before in the literature. In fact, even if the CSC and CPC have been performed in [44], [70], neither have faced the issue of limiting the aerodynamic torque. Moreover, in [44], a WECS with a passive three-phase diode rectifier and a boost converter is considered. The control scheme is largely dependent on this power converter topology and is not suitable for the application on the WECS considered in the present work. In fact, the control laws proposed in [44] explicitly refer to the generator rectification voltage (regulated by the boost converter) to achieve the ideal power characteristic, while in the present work, this voltage is held constant by the

GSC. For a thorough evaluation of the performance achieved with the proposed control scheme, it is possible and useful to compare the results achieved in [70]. In this study, the generator speed was regulated with a PID speed controller whose output was the reference current of a buck converter connected to a battery bank; therefore, the FOC was not performed. Moreover, the control scheme avoids the need for wind speed measurement or estimation and makes use of an aerodynamic power observer and shaft speed measurement. Specifically, in [70], the MPPT was performed with the power signal feedback (PSF) method, while the CPC was performed with a closed loop with another PID regulator. **Table 6** summarises the main features of the compared control schemes. **Figure 9** and **Figure 10** shown in [70] can be compared to **Figure 17** and **Figure 16 (b)**, respectively. It can be seen how the control schemes achieved **(b)**, respectively. It can be seen how the control schemes achieved

Table 6. Main features of the compared WECS control schemes.

Main Features	VSC + LO (Proposed in This Work)	Control Scheme Proposed in [70]
Wind turbine	VSFP Ducted HAWT	Conventional VSFP wind turbine
Electrical generator	APMSG	Conventional PMSG
Power converter topology	Grid connected back-to-back PWM inverters	Passive diode rectifier + buck converter connected to a battery bank
MPPT control method	Optimal TSR Model-based approach with wind speed estimation	PSF Model-based approach with aerodynamic power estimation
CSC method	FOC with a PI speed closed loop	PID speed closed loop (no FOC)
CPC method	Open loop regulation	PID aerodynamic power closed loop
CTC method	Open loop regulation	Not performed

overall similar performances until the CPC. This comparison definitively clarifies the originality and effectiveness of the proposed WECS. Finally, the author highlights that the merit of the performance achieved with the control scheme proposed in this work has to be also attributed to the accurate wind speed estimation achieved with the designed NN. In fact, an accurate wind speed estimation is crucial for optimal shaft speed reference computation in the MPPT and CTC regions. Moreover, an accurate wind speed estimation allows for a timely and proper transition between the four designed control laws.

2.5. Final considerations

An innovative control scheme for a direct-drive PMSG fully embedded in small-scale VSFP DHAWT over an extended wind speed range has been presented. This control strategy is implemented considering an AMPSG grid-connected through a back-to-back connection of two PWM three-phase inverters. An ideal power regulation characteristic depending on wind speed is considered to maximise the power extraction, ensuring the respect of the safety mechanical limits of the WECS. A VSC has been designed to achieve the ideal regulation characteristic. This controller regulates the shaft speed of the DHAWT according to four control laws performed in four wind speed subregions. In the low-speed region, MPPT is performed with the optimal TSR method. Instead, the high wind speed region is divided into three subregions in which the CSC, CPC, and CTC are performed to avoid exceeding the rated shaft speed, the rated aerodynamic power, and the maximum aerodynamic torque of the DHAWT. Moreover, a LO has been designed for the estimation of the aerodynamic torque necessary for CPC and CTC implementation. Finally, a shallow NN has been designed for the estimation of the wind speed necessary for the transition between the control laws and the MPPT control and CTC implementation. An analytical study has been performed to properly choose the inputs of the WSE.

The proposed control scheme has been validated through tests executed on a laboratory experimental setup. These tests have been performed considering a ramp wind speed pattern to explore the whole operating range of the DHAWT. The results show that the overall control strategy is successful in tracking the ideal power regulation characteristic. Moreover, the designed aerodynamic torque LO and WSE show good performances. To better evaluate the performances achieved with the proposed control scheme, comparisons with other solutions from the literature have been made. The LO achieves very similar performances to those of an adaptive ATO. Instead, the NN WSE is more accurate than a model-based WSE whose performances are influenced by the estimation errors on the aerodynamic torque. Finally, a comparison with a previously reported control scheme further demonstrates the effectiveness and originality of the proposed solution.

2.6. Publications

The contents and results presented in this chapter have been published in [79].

3. Cogging Torque Minimization of Modular PMSM

3.1. Introduction and State of the Art

In the context of the design of the PMSMs, the adoption of novel topologies based on the stator modularity and segmentation has gained increasing interest in the recent years. The stator of such machines is segmented in separated core modules which commonly assume the shape of T-cores (with one stator tooth), C-cores (with two stator teeth) or E-cores (with three stator teeth). Compared to conventional one-piece-stator PMSMs, this topology ensures many advantages from a manufacturing and assembling point of view: the reduction of material wastage [27], [80], simplicity of the stator winding process [80], [81], ease of transportation and assembling [28], and the possibility of using different materials for the stator and rotor core [27]. Such advantages are particularly noticeable for large machines, such as wind and tidal generators [20], [21]. Nevertheless, in the literature, this topology has also been studied for low power and small size PMSMs, as in [22]-[24]. Some recent research has also investigated and pointed out the advantages of the modular machines in terms of performances, such as:

- higher filling factor, that allows to increase the power density [27], [28] [80], [81];
- enhanced fault-tolerant capability caused by the separation of the modules which avoids the faults propagation [23], [28];
- enhanced demagnetization-withstand capability [29].

However, the presence of additional flux gaps between the core modules adversely affects the electromagnetic torque, causing a reduction of the average torque and increasing the cogging torque. The cogging torque is an undesired torque pulsation produced by PMSMs also at no-load condition, which causes

vibrations, acoustic noise, and speed pulsations. Conventional PMSMs with a one-piece-stator are affected only by cogging torque harmonics caused by the non-uniformity of the airgap due to the presence of the stator slots, which are called native harmonic components (NHCs). Instead, the flux gaps between the core modules can introduce additional harmonic components (AHCs) of the cogging torque which are characterized by a lower harmonic order and higher amplitude compared to the NHCs [28], [30], [82].

Despite several methods have been developed for the cogging torque minimization, these mostly deal with PMSMs affected only by NHCs. For example, methods widely investigated are the rotor or stator skewing [83], [84], the adoption of dummy slots or notches on the tooth tips [85], [86], slot openings design [87], and teeth pairing [88], [89]. Instead, the minimization of the AHCs caused by modular stators has received poor attention so far. The study presented in [90] shows that the rotor skewing has no influence on AHCs of low order. In [30], an optimal number of uniform stator modules or an optimal combination of non-uniform stator modules are suggested to minimize the cogging torque. However, this method lacks flexibility and limits the design choices. Moreover, even when the optimal design choice is adopted, a non-negligible cogging torque remains. In [20], a method to mitigate the cogging torque of a modular PMSM with E-cores has been proposed. This method uses the cogging torque produced by shifted slot openings to compensate that produced by the flux gaps between the core modules. However, this method has a limited effectiveness for some specific topologies and cannot be extended to modular machines with a different shape of the core modules.

In the present work, two novel methods have been proposed to minimize the cogging torque of modular PMSMs. The first one is based on the design of multiple and periodically reproduced shapes of the stator tooth tips by means of a topological optimization (TO). A similar approach has been proposed in [91],

in which the design of a unique shape for all the tooth tips has been performed to reduce the cogging torque of an outer rotor brushless dc motor with a one-piece-stator. However, the analysis performed in the present work shows that the AHCs cannot be minimized by means of the design of a unique shape of the tooth tips, but a defined quantity of different tooth tips should be designed. The second one is based on the injection of sinusoidal shapes in the stator tooth tips, whose frequency is directly correlated to the frequency of the AHCs to be minimized. The sinusoidal shaping is a method already employed to contour the PMs [92], [93] or to modulate the air gap length [94] to minimize the cogging torque of PMSMs. However, to the best of the author's knowledge, this method has not been applied to contour the stator tooth tips for the minimization of AHCs of the cogging torque so far. Both the proposed methods are based on the injection of novel cogging torque harmonic components to compensate the AHCs, by means of the air gap modulation. Moreover, compared to the existing methods, the proposed ones are flexible enough to handle arbitrary topologies of modular PMSMs with uniform stator segments, without limiting the designer choices as in [30].

A full analytical solution to the topological and shape optimization problems defined in this work would be suffering from two important limitations:

- difficulties in considering unconventional topologies and geometries;
- accuracy reduced by the presence of non-linear and parasitic phenomena.

In the literature, in the context of the optimization of electrical machines, to overcome the limitations of the analytical approach, a widely adopted strategy is to couple metaheuristic algorithms with the finite element analysis (FEA). Despite the non-negligible computational cost, the adoption of FEA guarantees high accuracy and the enables the possibility to analyze fully customized topologies and solutions. For example, a genetic algorithm (GA) has been used

to optimize the PM distribution [95] or to optimize the position and size of notches in the stator tooth tips [96] to minimize the cogging torque of permanent magnet machines (PMMs); in [97], a memetic algorithm has been used to optimize the shape and displacement of PMs of an interior PMSM (IPMSM) to optimize the flux weakening capability.

The computational effort required by metaheuristic algorithms coupled with FEA can be mitigated by means of computationally efficient surrogate models which can substitute the time-consuming FEA for the computation of the objective function of the optimization problem. ANN-based surrogate models constitute a promising approach recently investigated for the reduction of computational requirements in electrical machines' optimizations. For example, in [98], a topological binary particle swarm optimization (BPSO) coupled to a surrogate model based on a convolutional neural network (CNN) together with full and reduced order FEA maximized the torque of a synchronous reluctance motor (SynRM). By performing 80% of the BPSO iterations using the CNN, results comparable to a full order FEA optimization are achieved. The computational times are reduced of almost 20 times, providing a solution in 24 h. Moreover, in [99], a multi-objective GA has been successfully used with two Bayesian regularization backpropagation neural networks which approximate the relationship between three design variables and the average torque and the torque ripple of a SynRM. In this work, the author investigates the use of multilayer ANNs to approximate the relationship between the design variables and the cogging torque waveform. A comparison with the results achieved with the conventional approach based on the use of a genetic algorithm directly coupled to the FEA will show the superiority of the investigated method in terms of computational efficiency.

3.2. Cogging Torque of Modular PMSMs

The cogging torque of PMSMs is caused by the interaction between isofrequential harmonics of the rotor magneto-motive force (MMF) and of the flux-path permeance function (FPPF) [100]-[102]. The harmonics of the magneto-motive force are caused by the shape and placement of the rotor PMs. Instead, the harmonics of the FPPF are caused by the variations of the airgap length due to the stator slots and by the presence of additional airgaps in the flux-path of modular stators. The cogging torque of modular PMSMs can be expressed as:

$$T_{cog}(\theta) = T_{NHC}(\theta) + T_{AHC}(\theta) \quad (25)$$

where θ is the electrical rotor position, T_{NHC} represents the NHCs caused by the presence of the stator slots and T_{AHC} represents the AHCs caused by the segmented stator. The frequency of the NHCs is an integer multiple of the least common multiple (LCM) between the number of poles and the number of stator slots. Instead, the AHCs frequency is an integer multiple of the LCM between $2n_p$ and the number of stator core segments N_s :

$$T_{NHC} = \sum_i^{\infty} T_{NHCi} \sin(LCM(2n_p, N_s)i\theta + \varphi_{NHCi}), \quad i \in \mathbb{N} \quad (26)$$

$$T_{AHC} = \sum_i^{\infty} T_{AHCi} \sin(LCM(2n_p, m)i\theta + \varphi_{AHCi}), \quad i \in \mathbb{N} \quad (27)$$

where T_{NHCi} , T_{AHCi} , and φ_{NHCi} , φ_{AHCi} are the amplitudes and the phase shift of the i -th harmonic component, respectively.

Since the number of stator segments is equal or smaller than the number of stator slots, the period of the AHCs can be higher than the period of the NHCs. Moreover, since the low order harmonics of the MMF and FPPF are generally greater than the high order ones, it is expected that the AHCs of the cogging torque are greater than the NHCs.

3.3. The Case Study

To investigate and validate the methods proposed for the cogging torque minimization, the same annular PMSM (APMSM) described in subsection 2.2.2 has been chosen as a case study. **Figure 18** depicts one of the ten modules of the considered APMSM with 20, 30 and 60 uniform stator core segments. Machine geometrical parameters and materials are summarized in **Table 7**.

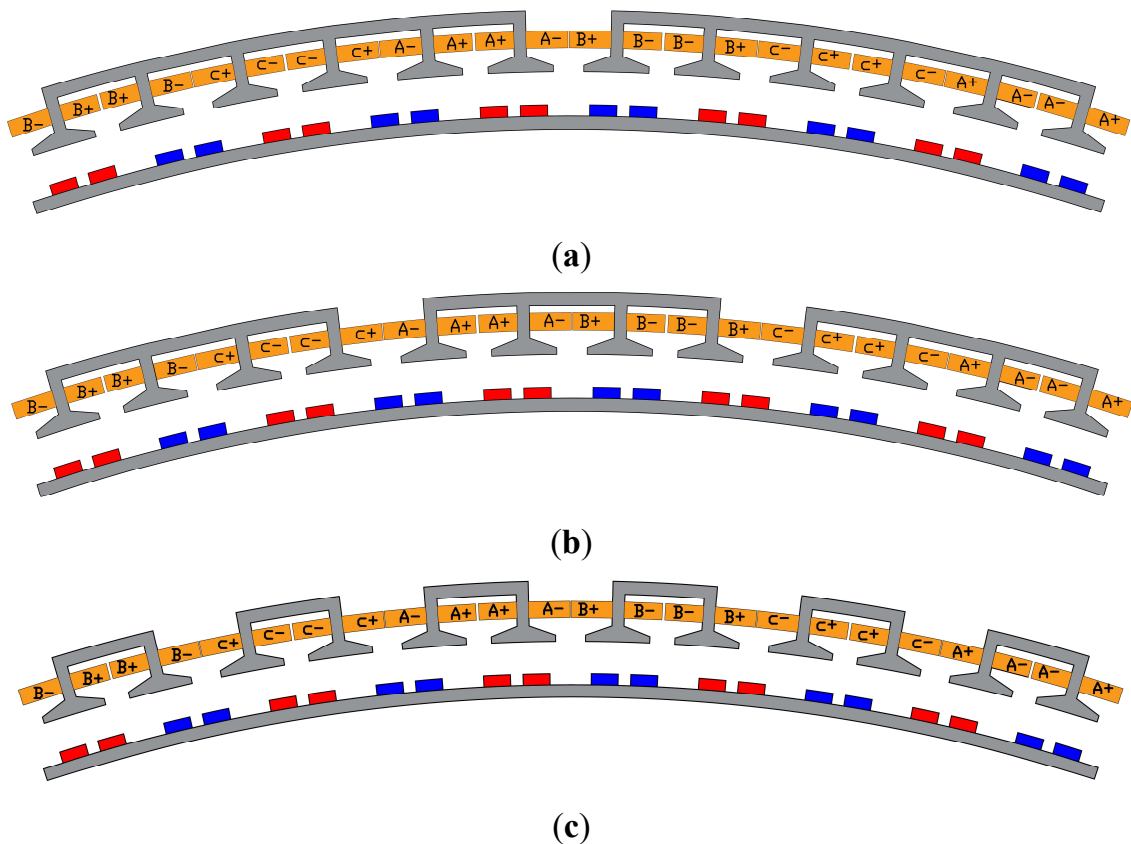


Figure 18. Modules of the APMSM: (a) Two stator segments per module; (b) Three stator segments per module; (c) Six stator segments per module.

Considering (27), the following harmonic orders of the AHCs are expected in an electrical period for the APMSMs with 20, 30 and 60 stator segments, respectively:

$$\frac{LCM(2n_p, m)}{n_p} = \frac{LCM(100, 20)}{50} i = 2i, \quad i \in \mathbb{N} \quad (28)$$

$$\frac{LCM(2n_p, m)}{n_p} = \frac{LCM(100, 30)}{50} i = 6i, \quad i \in \mathbb{N} \quad (29)$$

$$\frac{LCM(2n_p, m)}{n_p} = \frac{LCM(100, 60)}{50} i = 6i, \quad i \in \mathbb{N} \quad (30)$$

For the APMSM with 20 stator segments, a higher amplitude of the first AHC is expected with respect to the others APMSMs. In fact, in (28), since $LCM(100, 20) = 100$, the first AHC is produced by the fundamental component of the rotor MMF. In (29) and (30), the first AHC is produced by the third harmonic component of the MMF which has a smaller amplitude if compared with the fundamental component. Moreover, the APMSM with 60 stator segments is expected to have larger AHCs than the one with 30 stator segments. In fact, when additional airgaps are introduced, the reluctance of the back-iron increases. This introduces more flux linkage across slot openings and tooth tips, increasing the tangential flux density, which adversely affects the cogging torque [30]. Considering (26), instead, the following harmonic orders of the NHCs are expected for the three APMSMs:

$$\frac{LCM(2n_p, N_s)}{n_p} = \frac{LCM(100, 120)}{50} i = 12i, \quad i \in \mathbb{N} \quad (31)$$

In (31), since $LCM(100, 120) = 600$, the first NHC is produced by the 6th component of the rotor MMF. Hence, the amplitudes of the NHCs are negligible if compared to the amplitudes of the AHCs.

To analyze the cogging torque of the APMSMs, transient-with-motion (TWM) 2D FEA have been performed using the MagNet software. The TWM solver provides accurate solutions by considering the motion effect as well as the induced eddy currents. A 450 steps TWM FEA has been performed to analyze the cogging torque over an electric period. In **Figure 19** the cogging torque waveforms and harmonic spectra of the APMSMs with 20, 30 and 60 stator core segments are reported. analyze the cogging torque over an electric

Table 7. Main parameters and materials of the APMSM.

Parameter	Value
No. of modules	10
N_s	120
Stator back-iron thickness	4 mm
Rotor back-iron thickness	4 mm
PM thickness	3.5 mm
L_{stk}	10 mm
g	10 mm
Stator external radius	583 mm
Rotor external radius	545 mm
Tooth tips width	20.3 mm
Tooth tips height	2 mm
Copper fill factor	0.08
Element	Material
Magnets	NdFeB 40/23
Stator core	10JNEX900
Rotor back-iron	10JNEX900
Windings	Copper 100% IACS

period. In **Figure 19** the cogging torque waveforms and harmonic spectra of the APMSMs with 20, 30 and 60 stator core segments are reported. The harmonic spectrum of the APMSM with 20 stator core segments has a wide 2nd harmonic and a 4th and 6th harmonics with amplitudes of 0.165 and 0.069 Nm, respectively. The APMSMs with 30 and 60 stator core segments have similar

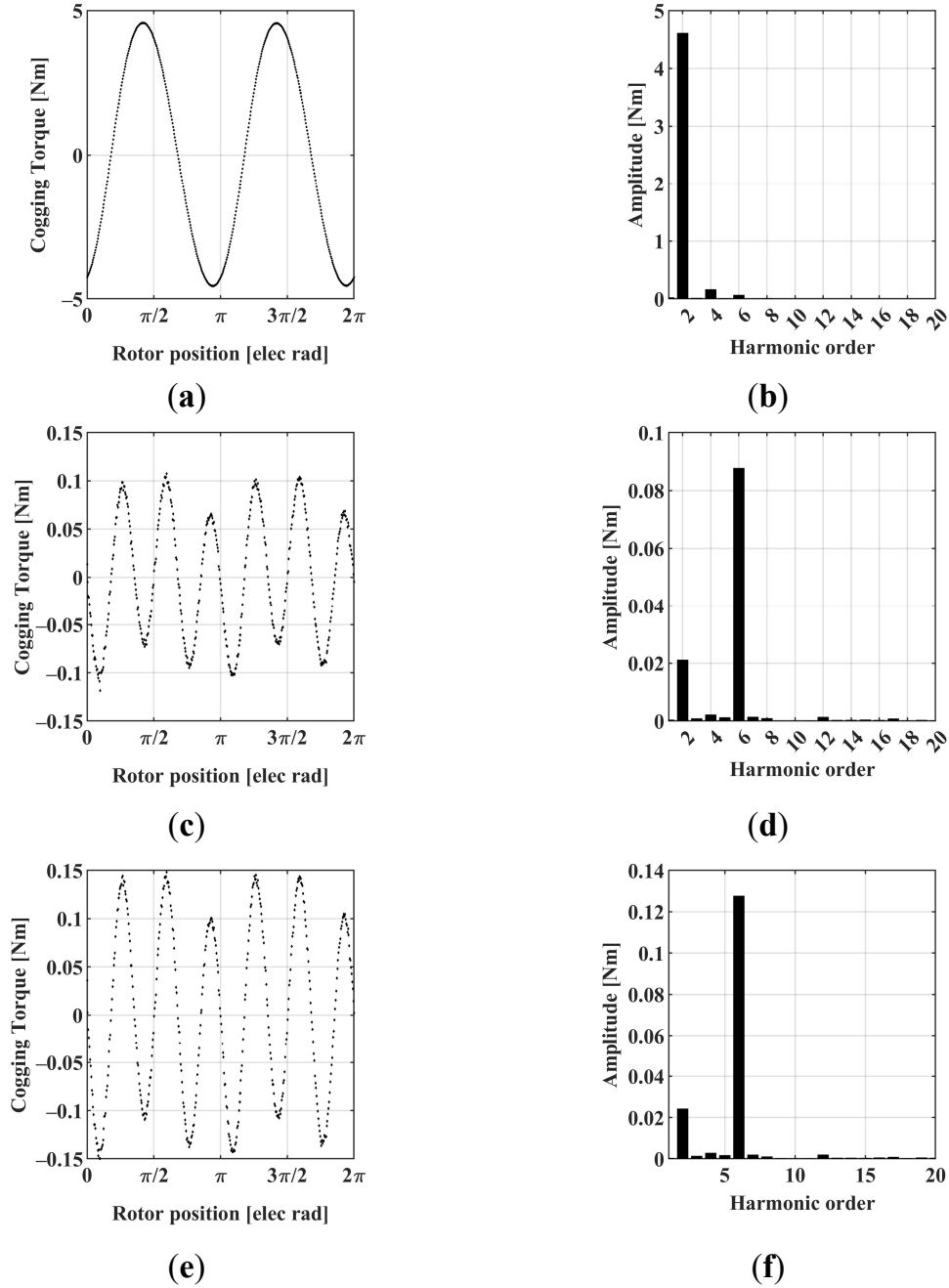


Figure 19. Cogging torque waveforms and harmonic spectra of the APMSMs: **(a,b)** APMSM with 20 stator segments; **(c,d)** APMSM with 30 stator segments; **(e,f)** APMSM with 60 stator segments.

spectra in which the dominant cogging torque harmonic is the 6th. The peak-to-peak values of the cogging torque are 9.125, 0.226 and 0.298 Nm, i.e., 76,0%, 1,9% and 2,5% of the rated torque, respectively. In all the cases, the NHCs are negligible if compared to the AHCs. Finally, note that in the last two harmonic spectra, unexpected weak harmonic components occur. These harmonics can be caused by slightly asymmetries in the model [103]. Nevertheless, the obtained results are overall in good agreement with the expectations.

3.4. Cogging Torque Minimization Based on the Stator Tooth Tips Topological Optimization

3.4.1. Theoretical Study and Design Formula

The first method proposed for the minimization of the AHCs is based on the design of multiple, periodically reproduced, independent shapes of the tooth tips of the machine, called *independent tooth tips*. By means of the shaping of the stator tooth tips, additional harmonic components of the FPPF and consequently of the cogging torque can be injected. Considering the modified shapes of the tooth tips, the cogging torque of a modular PMSM can be expressed as:

$$T_{cog} = T_{NHC} + T_{AHC} + T_{IHC} \quad (32)$$

where T_{IHC} describes the components of the cogging torque caused by the shape of the tooth tips, called *introduced harmonic components* (IHCs). The proposed strategy aims at directly suppress the AHCs by means of the IHCs. For this purpose, the IHCs should have the same frequency of the AHCs.

To find a relationship between the frequency of the IHCs and the number of the independent tooth tips, the author conducts a theoretical study. In [21], the superposition principle is employed to study the cogging torque of PMMs with

a segmented stator core (SSC). According to this principle, the contributions of the slotted stator structure and of the stator segmentations are independent and can be added together. In particular, the cogging torque contribution due to the slotted stator structure can be studied by considering a non-segmented slotted machine. Commonly made assumptions to study the cogging torque of these machines are as follows [21], [88], [101], [104]:

- the magnetic energy is stored only in the airgap and PMs volume;
- the PMs and air permeability are equal to the vacuum permeability;
- the permeability of the iron is assumed to be infinite;
- the airgap flux density is constant along the radial direction.

The cogging torque of a rotating PMM can be studied with the well-known energy method, which defines the cogging torque as:

$$T_{cog} = -\frac{\partial W}{\partial \theta} \quad (33)$$

where W is the stored magnetic energy. According to the above assumptions, W can be expressed as in [88]:

$$W = \frac{1}{2\mu_0} \int_{V_g} B^2 dV \quad (34)$$

where V_g is the volume of airgap and PMs, μ_0 is the vacuum permeability, and B is the no-load airgap flux density expressed as:

$$B(\alpha, \theta) = \Lambda(\alpha) F_m(\alpha, \theta) \quad (35)$$

where Λ is the airgap permeance function, F_m is the rotor MMF, and α is the angular displacement along stator circumference. Considering (35), (34) can be rewritten as:

$$\begin{aligned}
W &= \frac{1}{2\mu_0} \int_{V_g} \Lambda^2(\alpha) F_m^2(\alpha, \theta) dV \\
&= \frac{1}{2\mu_0} \int_0^{L_{stk}} \int_{R_1}^{R_2} \int_0^{2\pi} \Lambda^2(\alpha) F_m^2(\alpha, \theta) d\alpha dr dz \\
&= \frac{L_{stk}}{2\mu_0} \frac{(R_2^2 - R_1^2)}{2} \int_0^{2\pi} \Lambda^2(\alpha) F_m^2(\alpha, \theta) d\alpha \quad (36)
\end{aligned}$$

where L_{stk} , R_1 and R_2 are the stack length, the outer radius of rotor, and the radius to the tooth tips, respectively. Following the approach adopted in [105] and [106], Λ can be expressed as:

$$\Lambda = \frac{\mu_0}{g'} \quad (37)$$

with:

$$g'(\alpha) = g + l_{ss}(\alpha) + l_{tts}(\alpha) \quad (38)$$

where g is the difference between R_2 and R_1 , l_{ss} is the additional length of the airgap flux-path due to the presence of the stator slots and l_{tts} is the additional length of the airgap flux-path due to the modified shape of the tooth tips. Assuming $l_{ss}, l_{tts} \ll g$, (37) can be approximated by the first-order Taylor's expansion:

$$\begin{aligned}\Lambda &\approx \frac{\mu_0}{g} - \frac{\mu_0}{g^2}(g' - g) = \frac{\mu_0}{g} - \frac{\mu_0}{g^2}(l_{ss} + l_{tts}) \\ &= \frac{\mu_0}{g} + \Lambda_{ss} + \Lambda_{tts}\end{aligned}\quad (39)$$

where Λ_{ss} and Λ_{tts} are the permeance functions associated to the stator slotting effect and to the modified shape of the tooth tips, respectively. Considering (39), (36) can be expressed as:

$$\begin{aligned}W &= \frac{L_{stk}}{2\mu_0} \frac{(R_2^2 - R_1^2)}{2} \int_0^{2\pi} \left(\frac{\mu_0}{g} + \Lambda_{ss}(\alpha) + \Lambda_{tts}(\alpha) \right)^2 F_m^2(\alpha, \theta) d\alpha \\ &= \frac{L_{stk}}{2\mu_0} \frac{(R_2^2 - R_1^2)}{2} \int_0^{2\pi} \left(\frac{\mu_0^2}{g^2} + \Lambda'_{ss}(\alpha) + \Lambda'_{tts}(\alpha) \right) F_m^2(\alpha, \theta) d\alpha\end{aligned}\quad (40)$$

where $\Lambda'_{ss} = 2\Lambda_{ss}\mu_0/g + \Lambda_{ss}^2$, $\Lambda'_{tts} = 2\Lambda_{tts}\mu_0/g + \Lambda_{tts}^2 + 2\Lambda_{ss}\Lambda_{tts}$.

$$\Lambda'_{ss} = 2\Lambda_{ss}\mu_0/g + \Lambda_{ss}^2 \quad (41)$$

$$\Lambda'_{tts} = 2\Lambda_{tts}\mu_0/g + \Lambda_{tts}^2 + 2\Lambda_{ss}\Lambda_{tts} \quad (42)$$

Compared to the basic machine, the one with the modified shape of the tooth tips has an additional component of the squared permeance function, i.e., Λ'_{tts} . Therefore, the IHCs are caused by the interaction between this component and the rotor MMF:

$$T_{IHC} = -\frac{L_{stk}}{2\mu_0} \frac{(R_2^2 - R_1^2)}{2} \frac{\partial}{\partial \theta} \int_0^{2\pi} \Lambda'_{tts}(\alpha) F_m^2(\alpha, \theta) d\alpha \quad (43)$$

If N_i independent shapes of the tooth tips are periodically reproduced for all the tooth tips of the machine, the frequency f_{tts} of the function l_{tts} is:

$$f_{tts} = \frac{N_s}{2\pi N_i} \quad (44)$$

This frequency coincides with the frequency of Λ'_{tts} . This can be easily verified by means of the Werner formula, considering (39), the definition of Λ'_{tts} , and that the frequency of Λ_{SS} is equal to $N_s/2\pi$, i.e., an integer multiple of f_{tts} . Considering the orthogonality property of trigonometric functions, in (43) only the harmonic components of Λ'_{tts} and F_m^2 with the same frequency contribute to the energy, and, thus, to the cogging torque. Since the frequencies of the harmonic components of F_m^2 are multiple of $2n_p$ ([100], [101]), the frequency of T_{IHC} is expressed by:

$$f_{IHCi} = \frac{LCM\left(2n_p, \frac{N_s}{N_i}\right) i}{2\pi}, \quad i \in \mathbb{N} \quad (45)$$

Finally, the following expression for the T_{IHC} holds true:

$$T_{IHC} = \sum_i^{\infty} T_{IHCi} \sin\left(LCM\left(2n_p, \frac{N_s}{N_i}\right) i\theta + \varphi_{IHCi}\right) \quad (46)$$

where T_{IHCi} and φ_{IHCi} are the amplitude and the phase shift of the i -th harmonic component, respectively.

Equations (45) and (46) are a key result of the presented analytical study. These formulas state that the frequencies of the IHCs of a PMSM designed with N_i independent tooth tips are multiple of the LCM between the number of poles and the ratio of the number of slots and the number of independent tooth tips. Considering (27) and (46), to obtain IHCs with the same frequency of the AHCs, the following equation should be satisfied:

$$LCM\left(2n_p, \frac{N_s}{N_i}\right) = LCM(2n_p, m) \quad (47)$$

Therefore, the minimum number of independent tooth tips to suppress the AHCs is the following:

$$N_i = \min \left\{ n \in \mathbb{N} \mid LCM\left(2n_p, \frac{N_s}{n}\right) = LCM(2n_p, m) \right\} \quad (48)$$

Equation (48) is the *design formula* that allows the designer to choose the number of independent tooth tips to be designed to minimize the AHCs.

3.4.2. Topological Optimization of the Tooth Tips Shape

Equation (48) ensures that the IHCs include components with the same frequency of the AHCs. However, to suppress the AHCs, it is still necessary to properly set the amplitude and the phase shift of the IHCs through the design of the shape of the independent tooth tips. To face this issue, an approach based on the definition of a TO problem is proposed. Each independent tooth tip is discretized with a variable depth layer of N_{sub} sub-regions, called *sub-teeth*. To define the sub-region materials, a binary variable (S_{ij}) is assigned to each i -th sub-tooth of the j -th independent tooth tip. $S_{ij} = 0$ denotes air while $S_{ij} = 1$ denotes iron. Moreover, considering the depth of the sub-teeth layer as an

additional variable, the design variables of the TO problem can be expressed as follows:

$$\mathbf{x} = [S_{1,1} \dots S_{N_{sub},1} \dots S_{N_{sub},N_i} \text{ Depth}] \quad (49)$$

where $S_{i,j} \in \{0,1\}$, with $i = 1, \dots, N_{sub}, j = 1, \dots, N_i$, and $\text{Depth} \in [0 d_{MAX}]$, with d_{MAX} as the depth limit for the sub-teeth layers. Therefore, $N_{sub} \cdot N_i$ binary design variables and a real bounded design variable are defined. Two independent tooth tips discretized with layers of 5 sub-teeth are shown in **Figure 20**, while an APMSM module designed with the above independent tooth tips is depicted in **Figure 21**. As shown in the figure, the shapes of the independent tooth tips are periodically reproduced for all the tooth tips of the APMSM. The objective function, $f(\mathbf{x})$, of the TO is defined as the peak-to-peak value of the cogging torque:

$$f(\mathbf{x}) = \max(T_{cog}(\mathbf{x}, \theta)) - \min(T_{cog}(\mathbf{x}, \theta)) \quad (50)$$

where $T_{cog}(\mathbf{x}, \theta)$ is the cogging torque waveform of the APMSM designed in agreement with the current values of the design variables \mathbf{x} . The maximum value of N_{sub} is limited by the tooth tips width and the manufacturing tolerances, while the maximum value for d_{MAX} is limited by the tooth tip height. The choice of N_{sub} should be a trade-off between the achievable performances and the computational effort. In fact, the number of the sub-teeth is related to the quantity of the design variables affecting the complexity of the optimization problem and consequently the computational effort required by the heuristic solution. Similar considerations are done about the choice of d_{MAX} .

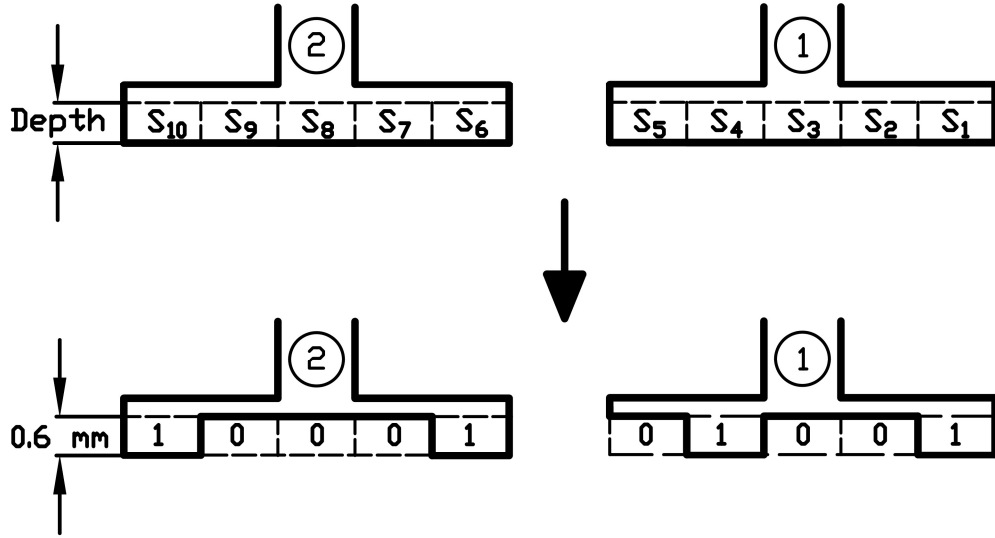


Figure 20. Example of two independent tooth tips discretized with a layer of 5 sub-teeth: $N_i = 2$, $N_{sub} = 5$, $\mathbf{x} = [1\ 0\ 0\ 1\ 0\ 1\ 0\ 0\ 0\ 1\ 0.6]$.

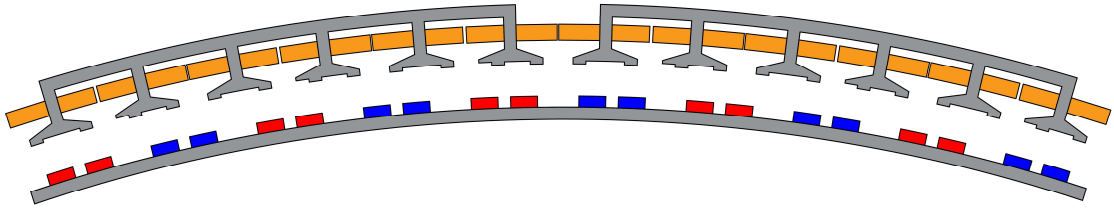


Figure 21. Module of the APMSM designed with: $N_i = 2$, $N_{sub} = 5$, $\mathbf{x} = [1\ 0\ 0\ 1\ 0\ 1\ 0\ 0\ 0\ 1\ 0.6]$.

3.4.3. Heuristic Solution Based on Genetic Algorithm and Artificial Neural Networks Surrogate Models

To solve the TO defined by (49) and (50), an original multi-training heuristic procedure that employs the GA and ANN-based surrogate models has been proposed, which can be described by the flow chart shown in **Figure 22**. It begins with the choice of the main design parameters: N_i , N_{sub} and d_{MAX} . Then, N_{start} sample data are generated through the TWM FEA of the APMSM considering random samples of the design variables in the design space. The sample data consists of a set of inputs X constituting the actual values of the design variables \mathbf{x} and a set of outputs Y constituting the values of $T_{cog_FEA}(\mathbf{x}, \theta)$

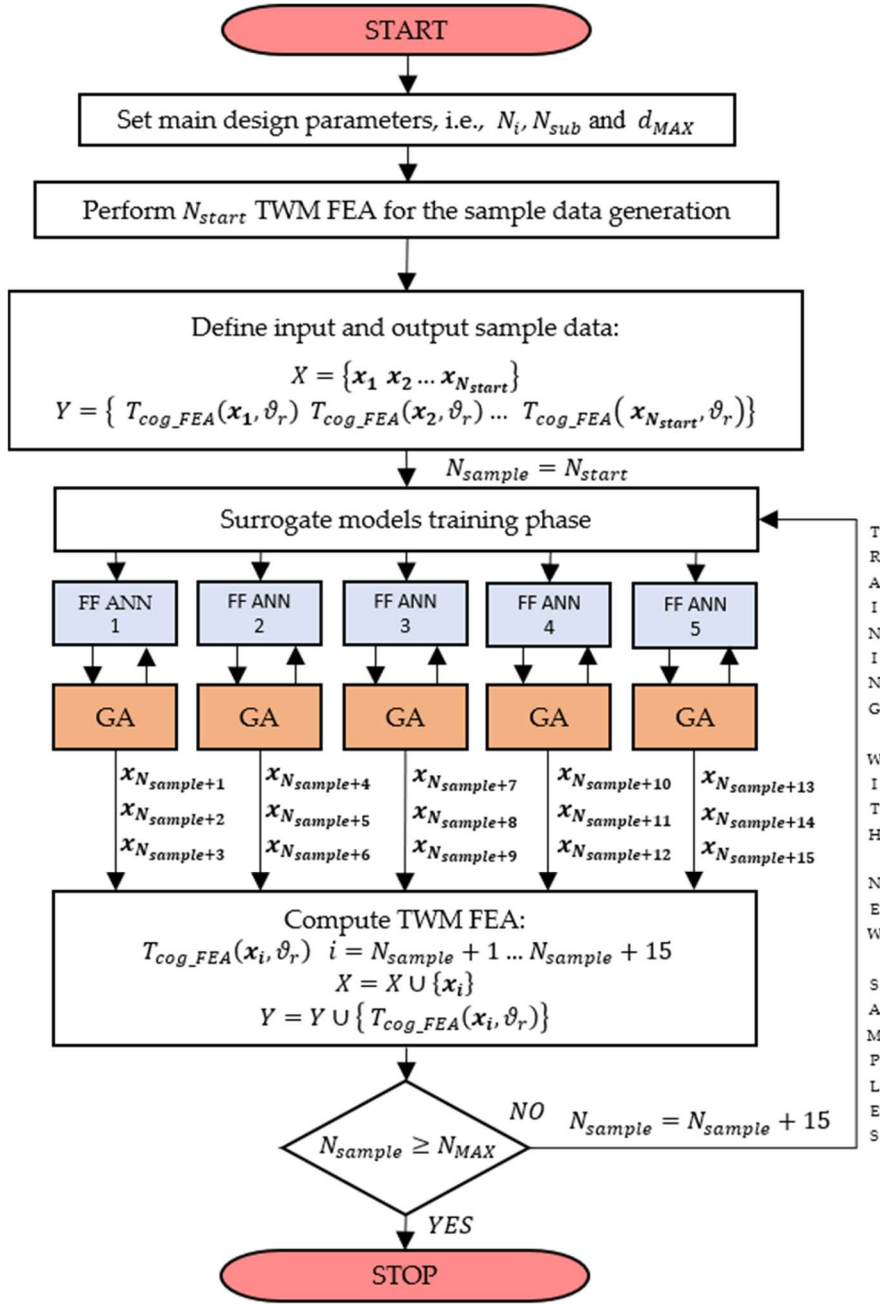


Figure 22. Flow chart of the proposed multi-training heuristic procedure.

computed by the TWM FEA. Specifically, $T_{cog_FEA}(\mathbf{x}, \theta)$ is a vector of $N_{step} + 1$ values of the torque in an electrical period, where N_{step} is the number of steps computed by the TWM FEA. Then, by making use of the sample data, a multi-training phase is performed. Five feed forward (FF) multilayer ANNs are chosen as surrogate models. Details about the choice of the FF ANNs will be presented subsequently.

These FF ANNs are employed by the GA for the objective function evaluation:

$$f(\mathbf{x}) = \max\left(T_{cog_ANN}(\mathbf{x}, \theta)\right) - \min\left(T_{cog_ANN}(\mathbf{x}, \theta)\right) \quad (51)$$

where $T_{cog_ANN}(\mathbf{x}, \theta)$ is a vector of $N_{step} + 1$ values of the torque in an electrical period, computed by the FF ANN. The best three solutions of each trial of the GA are used to perform a TWM FEA and compute $T_{cog_FEA}(\mathbf{x}, \theta)$. Thus, the new couples $(\mathbf{x}, T_{cog_FEA}(\mathbf{x}, \theta))$ are introduced as additional data for the next heuristic iteration. The process stops when N_{MAX} sample data are obtained. The achieved solution (\mathbf{x}_{opt}) is selected as the best sample among the input data set, i.e., the minimizer of the following function:

$$f_{FEA}(\mathbf{x}) = \max\left(T_{cog_FEA}(\mathbf{x}, \theta)\right) - \min\left(T_{cog_FEA}(\mathbf{x}, \theta)\right), \quad \mathbf{x} \in X \quad (52)$$

The main idea is to implement a step-by-step incremental accuracy of the surrogate models in the proximity of the minimum of $f(\mathbf{x})$. The author suggests employing five FF ANNs to mitigate the randomness of the data sample splitting in training and validation data, which affects the surrogate models' accuracy near the solution of the TO. The best three solutions of each GA are chosen for the next step to cope with the estimation errors of the surrogate models. Details about the TWM FEA, the surrogate models and the GA are provided below.

Computationally-Efficient TWM FEA

Each one of the 450 steps TWM FEA performed to obtain the cogging torque waveform requires about 55 min on a HP Z440 workstation equipped with an Intel Xeon CPU E5-1620 v3 @ 3.50GHz. Since the proposed procedure requires hundreds of TWM FEA, the author suggests moderating the number of steps of

the TWM FEA according to process time. To ensure that the TWM FEA catches the dominant cogging torque harmonics to minimize, the number of steps should be greater than the double of the maximum harmonic order of the cogging torque harmonics to be minimized, according to the Nyquist criterion. Considering that the maximum order of the cogging torque harmonics of the analyzed APMSMs is 6, 36 steps has been chosen for the TWM FEA performed during the proposed heuristic procedure. Therefore, $T_{cog_FEA}(\mathbf{x}, \theta)$ consists of 37 values of the torque in an electrical period. Note that 36 steps ensure an acceptable accuracy as will be shown later.

FF ANNs Surrogate Models Design

The designed FF multilayer ANN is depicted in **Figure 23**. The inputs and outputs are the design variables \mathbf{x} and the $T_{cog_ANN}(\mathbf{x}, \theta)$ waveform, respectively. The architecture consists of an input layer of $N_{sub}N_i + 1$ neurons, of N_{HL} hidden layers, each one with N_{HN} neurons, and an output layer of 37 linear neurons. The hidden neurons' activating function is the hyperbolic tangent sigmoid (tansig).

To obtain the five FF ANNs employed by the GA for the objective function evaluation, the following training procedure is proposed. First, the N_{sample} sample data are randomly split in training (80%) and validation (20%) data. Then, the number of hidden layers and the number of neurons for each hidden layer are chosen among the following sets of values:

$$\begin{aligned} N_{HL} &\in [1, 2] \\ N_{HN} &\in [2, 4, 6, 8] \end{aligned} \tag{53}$$

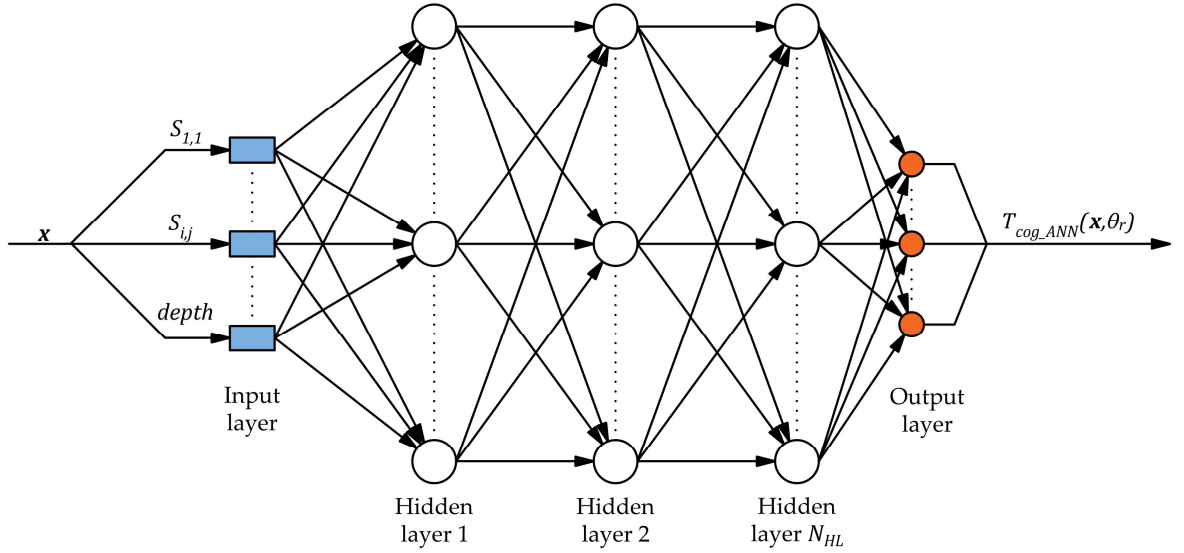


Figure 23. Architecture of the FF multilayer ANN used as surrogate model.

The Levenberg-Marquardt algorithm, i.e., one of the fastest among ANNs training methods [77], is applied to the training data set to determine the weights and biases of the FF ANN. Moreover, to avoid the ANN over fitting on the training data, a stop criterion based on the maximum validation failures is adopted. This criterion stops the Levenberg-Marquardt training algorithm if the estimation error on the validation data (*generalization error*) fails to improve for ten epochs in a row. This step is repeated for all the possible combinations of N_{HL} and N_{HN} , hence, 8 FF ANNs are trained according to (53). Finally, the trained FF ANN with the lowest validation error is chosen as surrogate model. A preliminary analysis has shown that, compared to (53), higher numbers of neurons and hidden layers don't ensure better validation errors considering a number of data samples lower than 300. As shown in **Figure 22**, this training procedure is repeated five times to obtain five ANN-based surrogate models. Note that the five FF ANNs could have different structures, i.e., different values of N_{HL} and N_{HN} . Moreover, these structures could vary with each iteration of the heuristic procedure. In fact, it is expected that the optimal number of hidden layers and neurons increases when the number of sample data increases.

GA Design

The main parameters and settings of the designed GA are summarized in **Table 8**. As the computation of the objective function using the surrogate models is very fast, the GA can operate with large individuals and generations to increase its performances. In this work, the initial population is made by the best 50 samples of the input data set X , and 350 samples obtained through a uniform sampling in the design space.

Table 8. GA parameters and settings

Parameter	Value
Population Size	400
Maximum Generations Number	100
Crossover rate	80%
Mutation rate	20%
Number of Elite Individuals	$0.05 \cdot \text{Population Size}$

3.4.4. Results

Results of the Proposed Heuristic Procedure

The design parameters used to perform the proposed heuristic procedure are reported in **Table 9**. According to (48), N_i is 6, 2 and 2, respectively. Moreover, the author set $N_{MAX} = 265$ to perform the proposed optimization in about 24 h, as can be deduced by **Table 10**, where the computational times of the main steps of the proposed heuristic procedure are reported. The training phase is related to the five FF ANNs surrogate models.

Table 11-Table 13 show the results of the proposed heuristic procedure obtained on the APMSMs with 20, 30 and 60 stator segments. Since the proposed method includes stochastic processes, i.e., the surrogate models training phase and the GA heuristics, it has been applied five times to properly evaluate its performances. As it can be seen, the method ensures outstanding performances:

in all the cases a reduction of the cogging torque higher than 85% is achieved. Particularly noteworthy are the results achieved on the APMSM with 20 stator segments. In fact, in this case, a cogging torque lower than that of the basic APMSMs with 30 and 60 stator segments has been achieved.

Figure 24 shows the cogging torque peak-to-peak values computed using the TWM FEA during the best optimizations, i.e., optimization no. 1, 2 and 2 for the APMSMs with 20, 30 and 60 stator segments, respectively. As it can be seen, a reduction of the cogging torque is already achieved with the first GA solutions, then, as the number of data samples increases, the accuracy of the surrogate models improves, and better solutions are achieved by the GA heuristics. Moreover, in the case of APMSMs with 30 and 60 stator segments, the best solutions are achieved from the early iterations. In fact, in these two cases, fewer design variables are used. Consequently, the FF ANNs surrogate models ensure good approximation performances of the objective function even with few data samples. This stresses the importance of reducing the design variables through a proper choice of the number of independent tooth tips to save computational time.

Table 9. Actual values of the main design parameters.

Parameter	Value
N_i	6, 2, 2
N_{sub}	9
d_{MAX}	0.8 mm
N_{start}	100
N_{MAX}	265

Table 10. Computational times of the heuristic procedure on a Workstation Hp Z440.

Operation	Computational Time
TWM FEA (36 steps)	5 min
Training phase (x5)	3 min
GA heuristic (x5)	6 min

Table 11. Results of the optimizations with the proposed heuristic procedure on the APMSM with 20 stator segments.

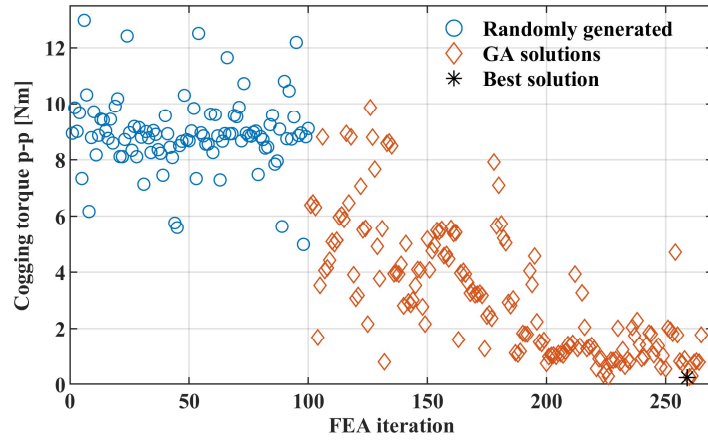
	$f_{FEA}(x_{opt})$ [Nm]	Cogging Torque Reduction [%]	Average Cogging Torque Reduction [%]
1	0.216	97.6	
2	1.210	86.7	
3	0.282	96.9	94.4
4	0.241	97.4	
5	0.592	93.5	

Table 12. Results of the optimizations with the proposed heuristic procedure on the APMSM with 30 stator segments.

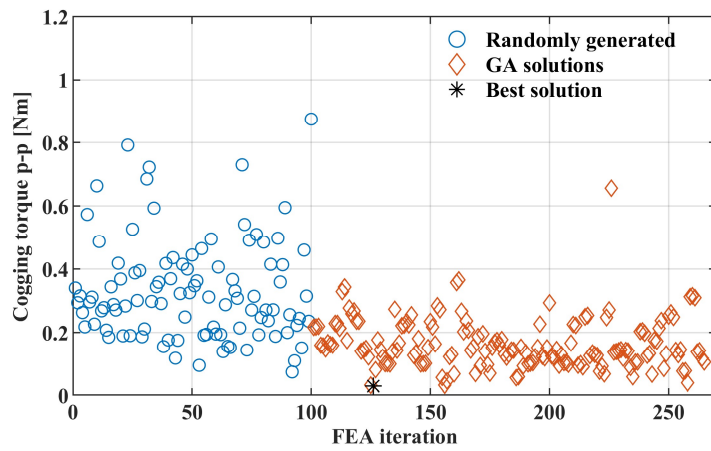
	$f_{FEA}(x_{opt})$ [Nm]	Cogging Torque Reduction [%]	Average Cogging Torque Reduction [%]
1	0.031	86.3	
2	0.030	86.7	
3	0.038	83.2	84.9
4	0.040	82.3	
5	0.032	85.8	

Table 13. Results of the optimizations with the proposed heuristic procedure on the APMSM with 60 stator segments.

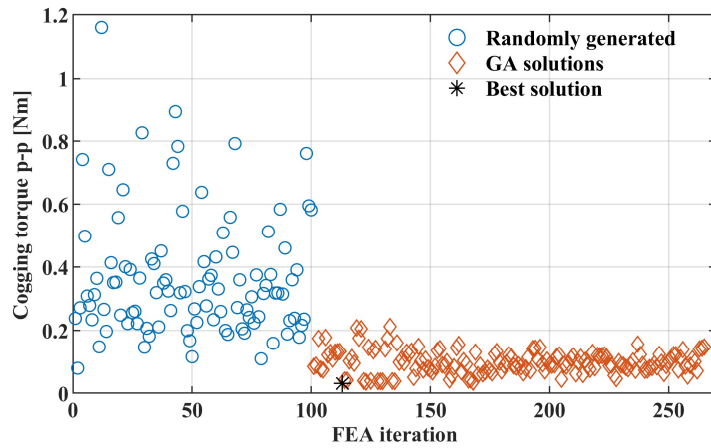
	$f_{FEA}(x_{opt})$ [Nm]	Cogging Torque Reduction [%]	Average Cogging Torque Reduction [%]
1	0.034	88.6	
2	0.032	89.3	
3	0.037	87.6	87.7
4	0.040	86.6	
5	0.040	86.6	



(a)



(b)



(c)

Figure 24. Objective function values computed using the TWM FEA performed during the heuristic procedure: (a) APMSM with 20 stator segments; (b) APMSM with 30 stator segments; (c) APMSM with 60 stator segments.

Figure 25 shows the cogging torque waveforms and harmonic spectra obtained with 36 and 450 steps TWM FEA of the best designs of the APMSMs achieved by the optimizations. The peak-to-peak values of cogging torque computed with the 450 steps TWM FEA are 0.224, 0.042 and 0.0362 Nm for the optimized APMSMs with 20, 30 and 60 stator segments, respectively.

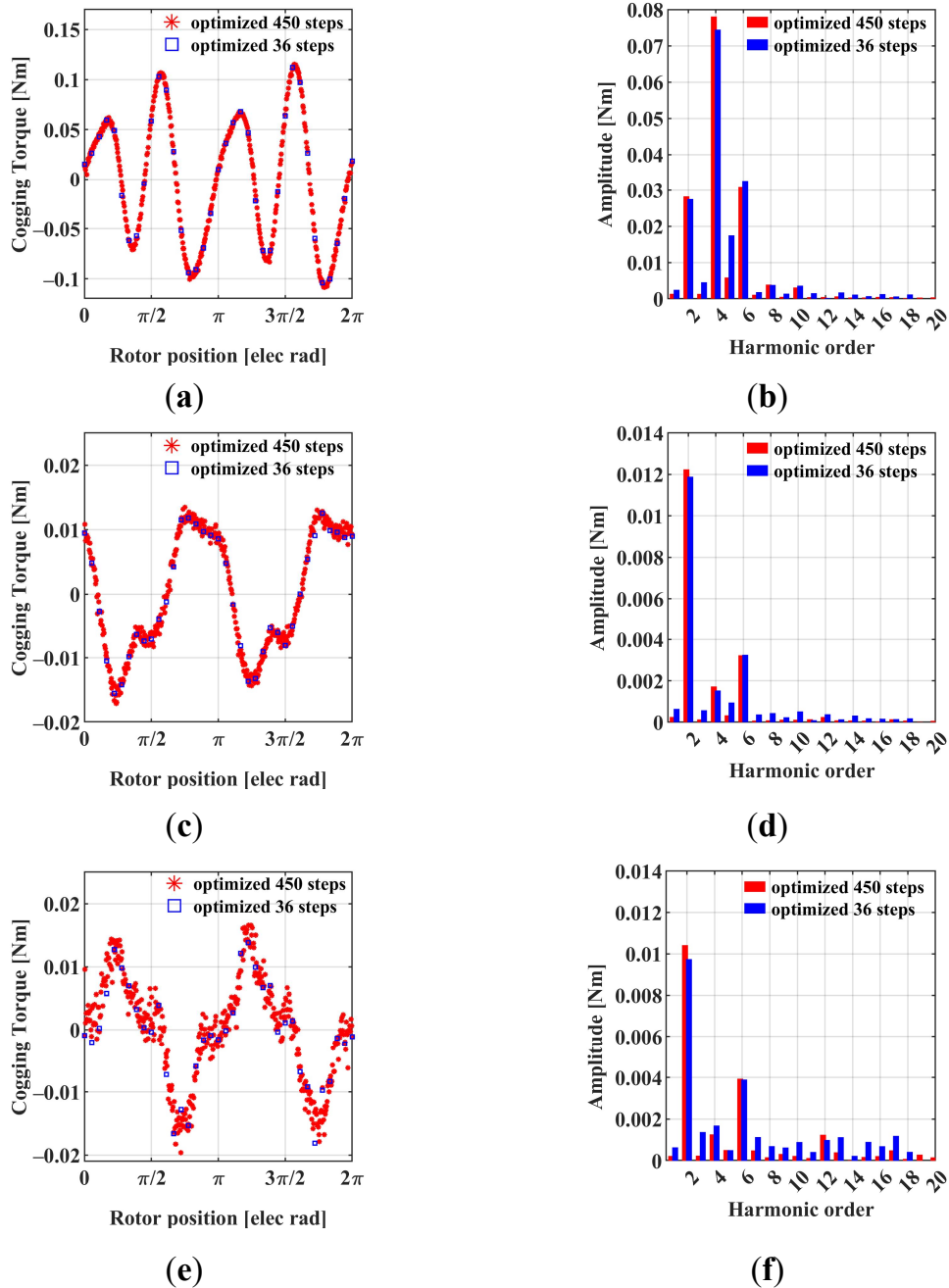


Figure 25. Cogging torque waveforms and harmonic spectra of the optimized APMSMs: (a,b) APMSM with 20 stator segments; (c,d) APMSM with 30 stator segments; (e,f) APMSM with 60 stator segments.

Therefore, a good agreement between the 36 and 450 steps TWM FEA is verified. Note that in all the cases a remarkable reduction of the dominant AHC is achieved. Moreover, the optimized APMSM with 20 stator segments also shows an improvement of the 4th and 6th harmonics over 50%. These results demonstrate the effectiveness of the proposed method in the minimization of the AHCs of the cogging torque. The no-load flux density distribution of the best designs of the APMSMs achieved by the optimizations are shown in **Figure 26**. This figure also shows the optimized shapes of the tooth tips, while the solutions achieved (\mathbf{x}_{opt}) have been reported in the figure caption. A low value of the flux density can be noted. This corresponds to a design choice of the APMSM selected as a case study. In fact, this choice allows to reduce the iron losses while

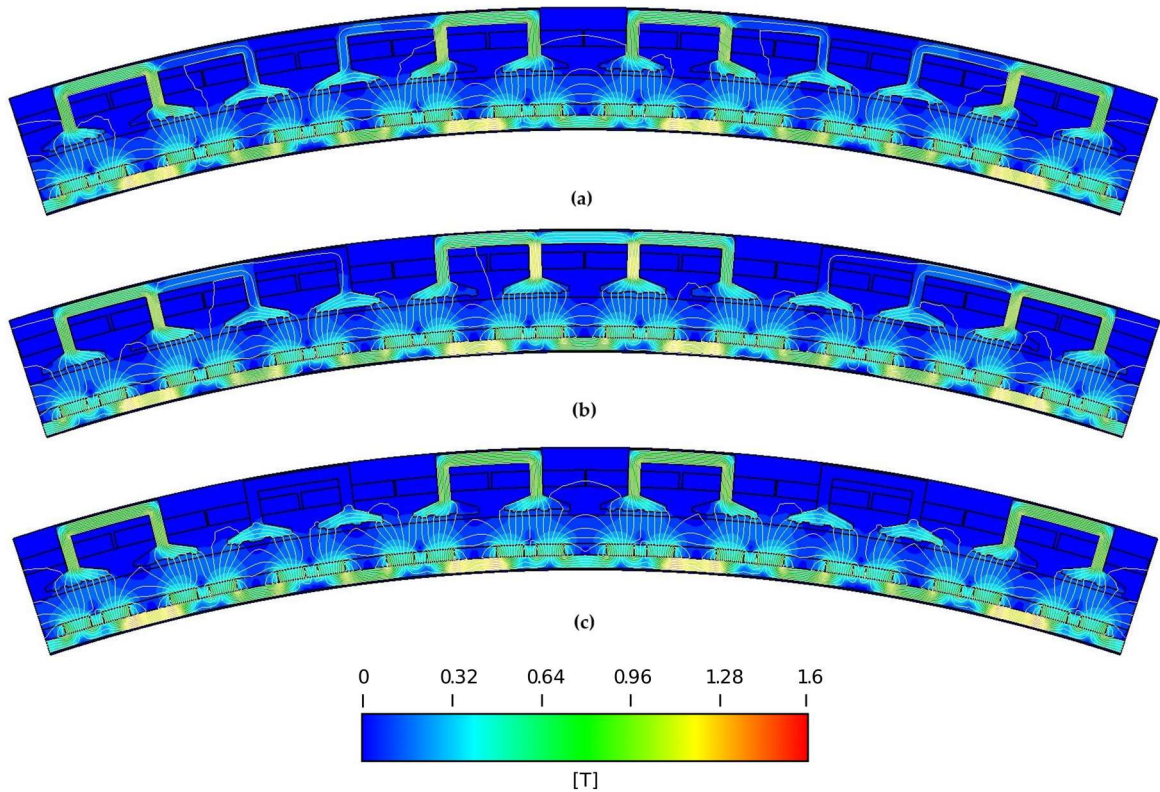


Figure 26. No-load flux density distribution of the optimized machines: (a) APMSM with 20 stator segments, $\mathbf{x}_{opt} = [001110011000010111010000011101000011111010000010111010\ 0.8mm]$; (b) APMSM with 30 stator segments, $\mathbf{x}_{opt} = [0\ 1\ 1\ 1\ 1\ 1\ 1\ 1\ 1\ 1\ 0\ 0\ 1\ 0\ 0\ 1\ 1\ 0\ 0.48mm]$; (c) APMSM with 60 stator segments, $\mathbf{x}_{opt} = [1\ 0\ 0\ 1\ 0\ 0\ 1\ 1\ 0\ 1\ 1\ 0\ 1\ 1\ 0\ 1\ 0\ 0.62mm]$.

meeting the torque requirements without increasing the copper losses, i.e., the main source of the losses of the considered machine.

To fully demonstrate the validity of the design formula (48), an analysis of the results achieved with values of N_i in disagreement with the design formula is required. **Figure 27** shows the results achieved through the optimizations on the APMSM with 20 stator segments with $N_i = 3, 4$, in disagreement with (48). As expected, a weak reduction of the cogging torque is achieved.

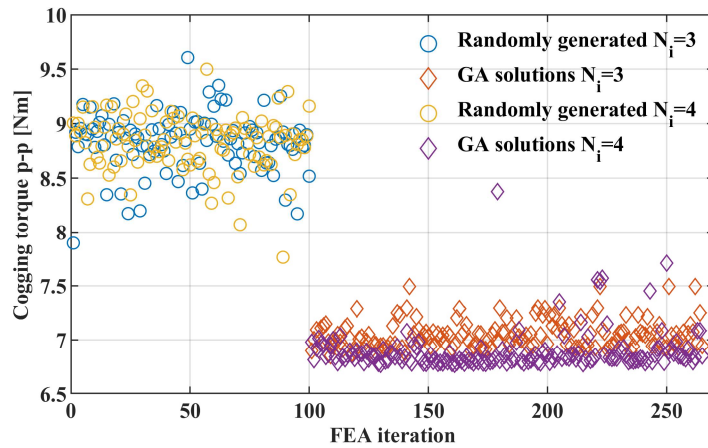


Figure 27. Objective function values computed using the TWM FEA performed during the heuristic procedure on the APMSM with 20 stator segments and $N_i = 3, 4$.

Figure 28 shows the cogging torque waveforms and harmonic spectra of the best achieved solutions, obtained with a 450 steps TWM FEA. The cogging torque peak-to-peak values of the optimized machines are 6.927 and 6.805 Nm respectively. Note that the APMSMs with $N_i = 3$ has a higher 4th harmonic compared to the basic one (greater by 42.8%) while there is a weak influence on the 2nd (lower by 24.7%) and 6th (lower by 17.7%) harmonic. Moreover, the APMSM with $N_i = 4$ has a higher $N_i=6$ th harmonic compared to the basic one (greater by 55.9%) while there is a weak influence on the 2nd (lower by 18.8%) and 4th harmonic (lower by 3.7%). These results agree with the theoretical study since in an electrical period, from (46), the harmonic orders of the IHCs expected for $N_i = 3, 4$ are $6i$ and $4i$, respectively, with $i \in \mathbb{N}$. These results demonstrate

the validity of the developed design formula (48). Note that the solution \mathbf{x} of the TO might be also constituted by the same shape for all the stator tooth tips. This implies that the design of a single tooth tip shape does not affect the AHCs of the cogging torque. Consequently, traditional methods based on dummy slots or notches equally placed in all the tooth tips cannot be adopted for the minimization of the AHCs.

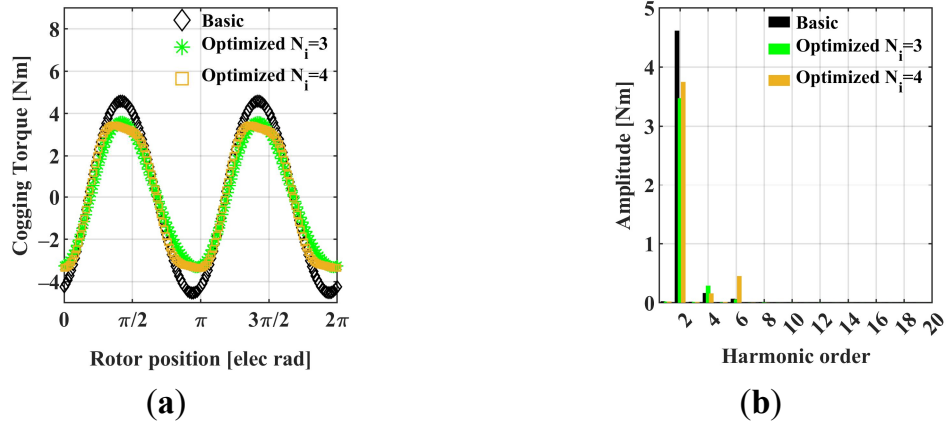


Figure 28. Comparison between the basic and optimized APMSMs with 20 stator segments and $N_i = 3, 4$: (a) Cogging torque waveforms; (b) Cogging torque harmonic spectra.

Results of the Direct Approach

To demonstrate the computational efficiency of the proposed multi-training heuristic procedure, the results are compared with those achieved with the conventional direct approach on the APMSM with 20 stator segments. In this case, a unique GA heuristic is performed, and the objective function has been directly computed by a 36 steps TWM FEA:

$$f(\mathbf{x}) = \max\left(T_{cog_FEA}(\mathbf{x}, \vartheta_r)\right) - \min\left(T_{cog_FEA}(\mathbf{x}, \vartheta_r)\right) \quad (54)$$

Same design parameters (i.e., N_i, N_{sub} and d_{MAX}) are employed. The GA population size (PS) and maximum generations number (MGN) are chosen so that the two methods have same execution times. Since the best combination of

the PS and MGN is not known a priori, the author chooses three different combinations for these two parameters. These combinations are reported in **Table 14** together with the number of TWM FEA iterated by the GA, i.e., PS · MGN + PS since the GA initial population is considered as well. The other settings of the GA used for the direct approach are equal to those listed in **Table 8**. The initial population is obtained through a uniform sampling in the design space. To properly compare the two approaches, five optimizations for each GA combination have been performed. Each TWM FEA requires 5 min to be performed, thus, each GA heuristic requires more than 25 h. Therefore, a slightly advantage of time has been granted to the direct approach. Nevertheless, as shown in **Table 15-Table 17**, none of the three GA combinations ensure the same performances obtained by using surrogate models. In fact, the average and maximum cogging torque reduction are lower than those reported in **Table 11**.

Finally, **Figure 29** shows the evolution of the best individuals among the GA generations obtained during the best optimizations performed: optimization no. 1, 3, and 5 for the 17×17 , 24×12 , and 30×9 GA combinations, respectively. This figure clearly shows the limit of the direct approach compared to the proposed one: to achieve good results through the GA, high values of the PS and of MGN are needed. This condition is satisfied by the proposed method by using computationally-efficient surrogate models.

Table 14. GA population size and maximum generations number set for the direct approach.

GA 1st Combination		GA 2nd Combination		GA 3rd Combination	
PSxMGN	No. of TWM FEA	PSxMGN	No. of TWM FEA	PSxMGN	No. of TWM FEA
17x17	306	24x12	312	30x9	300

Table 15. Results obtained with the direct approach on the APMSM with 20 stator segments using a 17x17 GA

	$f_{FEA}(x_{opt})$ [Nm]	Cogging Torque Reduction [%]	Average Cogging Torque Reduction [%]
1	1.850	79.7	
2	2.302	74.8	
3	2.289	74.9	73.9
4	1.864	79.6	
5	3.601	60.5	

Table 16. Results obtained with the direct approach on the APMSM with 20 stator segments using a 24x12 GA

	$f_{FEA}(x_{opt})$ [Nm]	Cogging Torque Reduction [%]	Average Cogging Torque Reduction [%]
1	1.997	78.1	
2	1.086	88.1	
3	1.080	88.2	82.4
4	1.184	87.0	
5	2.699	70.4	

Table 17. Results obtained with the direct approach on the APMSM with 20 stator segments using a 30x9 GA

	$f_{FEA}(x_{opt})$ [Nm]	Cogging Torque Reduction [%]	Average Cogging Torque Reduction [%]
1	3.003	67.1	
2	1.904	79.1	
3	2.477	72.6	77.3
4	1.496	83.6	
5	1.445	84.2	

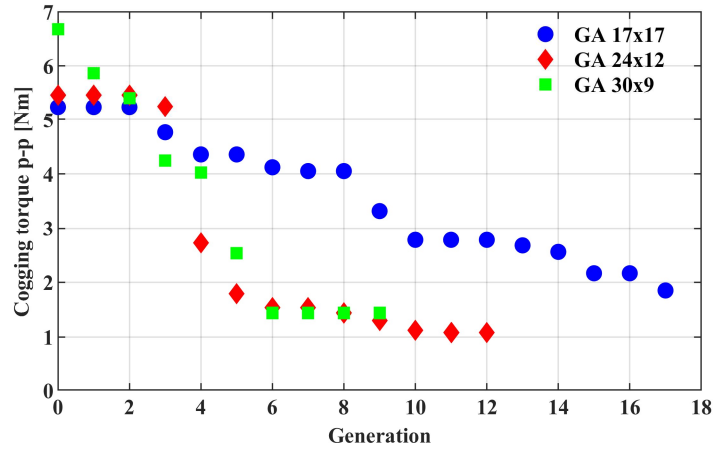


Figure 29. Evolution of the best individuals among GA generations obtained with the direct approach.

Comparison with the Basic Machine

In this subsection, a comparison between the basic and optimized design of the APMSM with 20 stator segments is reported. The optimized design is the one shown in **Figure 26 (a)**.

Figure 30 shows the torque waveforms and harmonic spectra at rated current of the basic and optimized designs obtained with a 450 steps TWM FEA. Note that the cogging torque of the basic machine largely affects the torque ripple under load operations. In fact, the 2nd harmonic of the cogging torque appears unaltered in the torque waveform. Instead, the torque of the optimized machine benefits from the proposed method and the torque ripple is significantly reduced.

In **Figure 31**, the permanent magnet flux-linkage with the three phases of the basic and optimized designs is shown. The basic design has an asymmetry of the flux-linkage with a phase B amplitude slightly larger than phases A and C. Instead, analysis performed on the basic design with 30 and 60 stator segments, not reported here, show a flux-linkage symmetric for the three phases. The optimized design keeps the asymmetry of the basic machine but the amplitudes of the fundamental components and of the other harmonic components are slightly reduced.

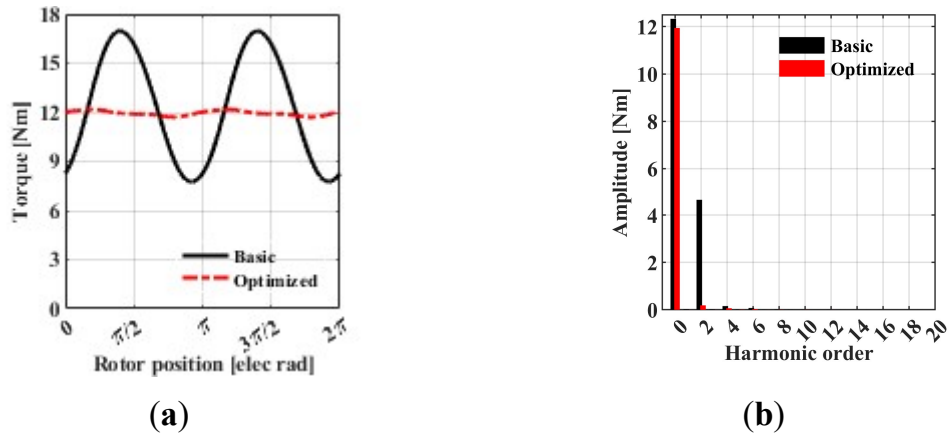


Figure 30. Comparison between the basic and optimized APMSMs with 20 stator segments at rated current: (a) Torque waveforms; (b) Torque harmonic spectra.

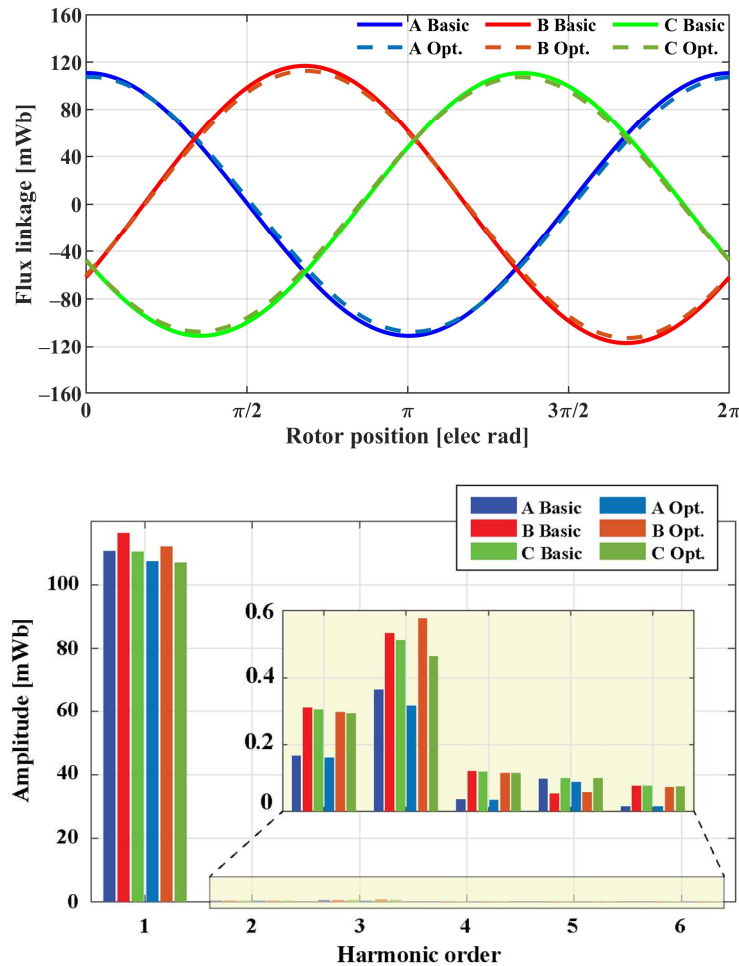


Figure 31. Waveforms and harmonic spectra of the permanent magnet flux-linkage for the three phases of the basic and optimized APMSM.

Details about the THD of the permanent magnet flux-linkage, torque ripple, average torque, and losses at rated speed and current of the basic and optimized designs are provided in **Table 18**. The average torque of the optimized machine

has been reduced by 3.1%, the torque ripple has been reduced by 66.7% while there are no appreciable alterations of the losses and permanent magnet flux-linkage THD. Due to the high value of the copper losses, the efficiency of the optimized and basic design is about 90%. However, since the considered fill factor is very low (see **Table 7**) the efficiency of the machine can be improved by increasing the copper volume.

Table 18. Comparison between the basic and optimized APMSM with 20 stator segments.

Parameter	Basic APMSM	Opt. APMSM
Average torque	13.05 Nm	12.64 Nm
Torque ripple (peak-to-peak to average torque ratio)	70,6%	3,9%
Phase A permanent magnet flux-linkage THD	0,37%	0,34%
Phase B permanent magnet flux-linkage THD	0,57%	0,61%
Phase C permanent magnet flux-linkage THD	0,58%	0,56%
Copper losses	91.8 W	91.8 W
Magnet losses	23.6 W	23.3 W
Iron losses	16.4 W	15.7 W

Sensitivity Analysis Considering Manufacturing and Assembling Tolerances

To evaluate the robustness of the proposed method, a sensitivity analysis has been performed considering manufacturing and assembling tolerances on the optimized design of the APMSM with 20 stator core segments, i.e., the machine shown in **Figure 26 (a)**. The considered manufacturing and assembling uncertainties are shown in **Figure 32** and are as follows:

- tolerance of stator tooth width, Δw_t ;
- tolerance of stator segments position, $\Delta \theta_t$;
- tolerance of sub-teeth width, Δw_{st} ;
- tolerance of magnets position, $\Delta \theta_{PM}$.

Note that all the considered uncertainties affect the cogging torque of the APMSM. Typical values of tolerance are considered, as reported in **Table 19** [101]. As in [107], a normal distribution is assumed for the manufacturing and assembling uncertainties with a standard deviation $\sigma = (UL - LL)/6$, where UL and LL are the upper and lower limits of the tolerance ranges, respectively.

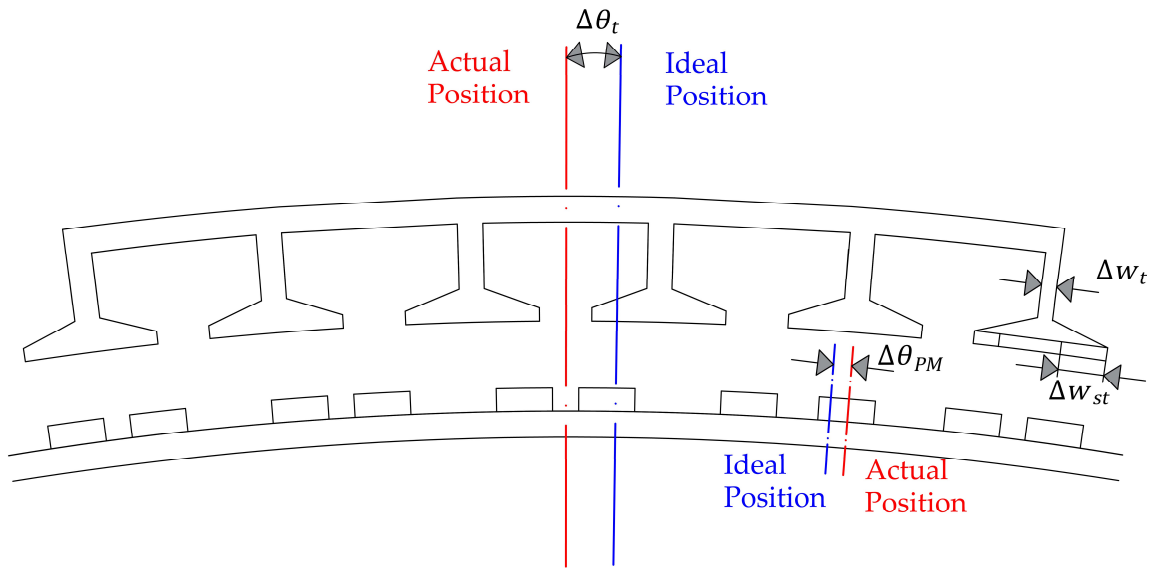


Figure 32. Manufacturing and assembling tolerances considered in the sensitivity analysis.

Table 19. Manufacturing and assembling tolerances.

Δw_t	$\Delta \theta_t$	Δw_{st}	$\Delta \theta_{PM}$
± 0.05 mm	$\pm 0.05^\circ$	± 0.05 mm	$\pm 0.05^\circ$

Two methods can be adopted to handle such tolerances. The first method is the uniform uncertainties method (UUM), which assumes that the uncertainty on each component is the same, e.g., all the teeth have the same width. Although its ease of implementation, the effects of the manufacturing tolerances may be underestimated with this method. The second approach is the non-uniform uncertainties method (non-UUM), which assumes that each component has its own uncertainty. This method ensures more realistic analysis but requires a higher computational effort since the motor periodicity is lost [101].

In this work, the author employed the non-UUM while considering equal APMSM modules. That is, each PM, tooth and stator segment of a module has its own uncertainty. This choice represents a fair trade-off between accuracy and computational effort. Thus, to evaluate the cogging torque under this assumption, a TWM FEA in a mechanical period of 36° should be performed, which is the angular span of a single APMSM module. In fact, due to the loss of the rotor periodicity caused by the tolerance of magnets' position, the TWM FEA cannot be performed in an electrical period. The number of steps of the TWM FEA has been fixed to 180, which is the product between 36 (i.e., the number of steps used to perform the optimization) and the number of pole pairs of a module of the APMSM. A 180 steps TWM FEA requires about 23 min. If the non-UUM were applied to each module of the APMSM, a TWM FEA in a mechanical period of 360° would have been necessary. Therefore, an 1800 steps TWM FEA requiring about 230 min would have been performed. Note that such a high computational time limits the number of TWM FEA iterations, reducing the analysis accuracy.

Figure 33 shows the peak-to-peak cogging torque values obtained by means of TWM FEA performed on several designs of the optimized APMSM subject to the considered tolerances. The average value of the peak-to-peak cogging torque of the optimized designs under manufacturing and assembling tolerances is shown in the figure. This value is equal to 0,69 Nm, which corresponds to a reduction of 92.4% if compared to the basic machine. Moreover, the minimum and maximum values of the peak-to-peak cogging torque among the analyzed machines are equal to 0,39 and 1.17 Nm, respectively. These results clearly show how a significantly reduction of the cogging torque is achieved even under manufacturing and assembling tolerances, proving the robustness of the proposed method.

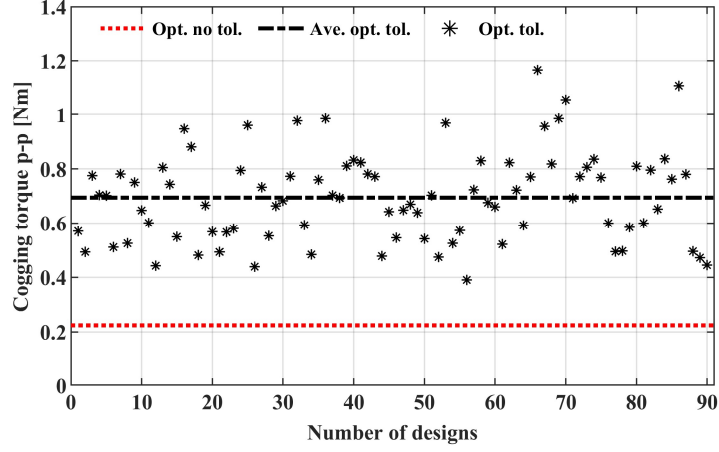


Figure 33. Peak-to-peak cogging torque of the optimized design of the APMSM with 20 stator segments under manufacturing and assembling uncertainties.

3.5. Cogging Torque Minimization Based on the Stator Tooth Tips Sinusoidal Shaping

3.5.1. Theoretical Study and Design Formula

The second method proposed for the minimization of the AHCs is based on the shaping of the tooth tips with sinusoidal profiles. To derive the relationship between the frequencies of the introduced sinusoidal profiles and the IHCs, the author followed the study reported in subsection 3.4.1. As a result of this study, the IHCs can be expressed as follows:

$$T_{IHC}(\theta) = \sum_{k=1}^{N_{sp}} T_{IHC_k} \sin \left(2\pi f_{sp_k} \theta + \varphi_{IHC_k} \right) \quad (55)$$

where N_{sp} is the number of the sinusoidal profiles introduced to shape the tooth tips, f_{sp_k} is the spatial frequency of the k -th sinusoidal profile, and T_{IHC_k} and φ_{IHC_k} are the amplitude and the phase of the k -th IHC. The key results expressed by (55) can be summarized as follows:

- each sinusoidal profiles introduces only an IHC;

- the frequency of the IHCs coincides with the spatial frequency of the sinusoidal profiles.

As stated in subsection 3.4.1, to suppress the AHCs by means of the IHCs, these should have the same frequencies. Therefore, if $N_{AHC} \subset \mathbb{N}$ is the arbitrarily chosen set of the harmonic order of the AHCs to be minimized, considering (27) and (55), the following condition should be satisfied:

$$f_{sp_k} = LCM(2n_p, m)i$$

$$f_{sp_k} = \frac{LCM(2n_p, m)i}{2\pi}, \quad i \in N_{AHC} \quad (56)$$

Equation (56) represents the design formula which allows to choose the frequency of the sinusoidal profiles. Note that a sinusoidal profile is introduced for each AHC to minimize.

The same methodology can also be applied for the minimization of the NHCs. Let be $N_{NHC} \subset \mathbb{N}$ the arbitrarily chosen set of the NHCs to minimize. According to (26) and (55), the IHCs to introduce to suppress the NHCs should have the following frequencies:

$$f_{sp_k} = \frac{LCM(2n_p, N_s)j}{2\pi}, \quad j \in N_{NHC} \quad (57)$$

Equation (57) can also be employed for the suppression of the cogging torque of conventional PMSMs with a one-piece stator core.

3.5.2. Formulation of the Optimization Problem

Equations (56) and (57) allow the designer to choose the number and frequency of the sinusoidal profiles which ensure to introduce cogging torque

harmonic components isofrequential with the AHCs and to the NHCs to be minimized. However, to suppress the AHCs and NHCs, it is also necessary to properly set the amplitude and position of the sinusoidal profiles.

Figure 34 shows two tooth tips shaped by means of the composition of two sinusoidal profiles. The shape of the tooth tips can be described by the distance from the centre of the PMSM to the tooth tips inner surface:

$$r(\alpha) = R_2 + S(\alpha, \mathbf{A}, \boldsymbol{\varphi}) + |\min(S(\alpha, \mathbf{A}, \boldsymbol{\varphi}))| \quad (58)$$

where

$$S(\alpha, \mathbf{A}, \boldsymbol{\varphi}) = \sum_{k=1}^{N_{sp}} A_k \cos(2\pi f_{sp_k} \alpha + \varphi_k) \quad (59)$$

$$\mathbf{A} = [A_1 \ A_2 \ \dots \ A_{N_{sp}}], \quad \boldsymbol{\varphi} = [\varphi_1 \ \varphi_2 \ \dots \ \varphi_{N_{sp}}] \quad (60)$$

in which, A_k , φ_k are the amplitude and phase shift of the introduced sinusoidal profiles. Equation (58) ensures that $r(\alpha) \geq R_2$, $\forall \alpha \in [0 \ 2\pi]$, i.e., that airgap length cannot be reduced with respect to the original shape of the tooth tips, as shown in **Figure 34**.

To determine the optimal amplitudes and phase shifts of the introduced sinusoidal profiles, the author defines an optimization problem in which the objective function coincides with (50), in which the vector of the design variables \mathbf{x} is:

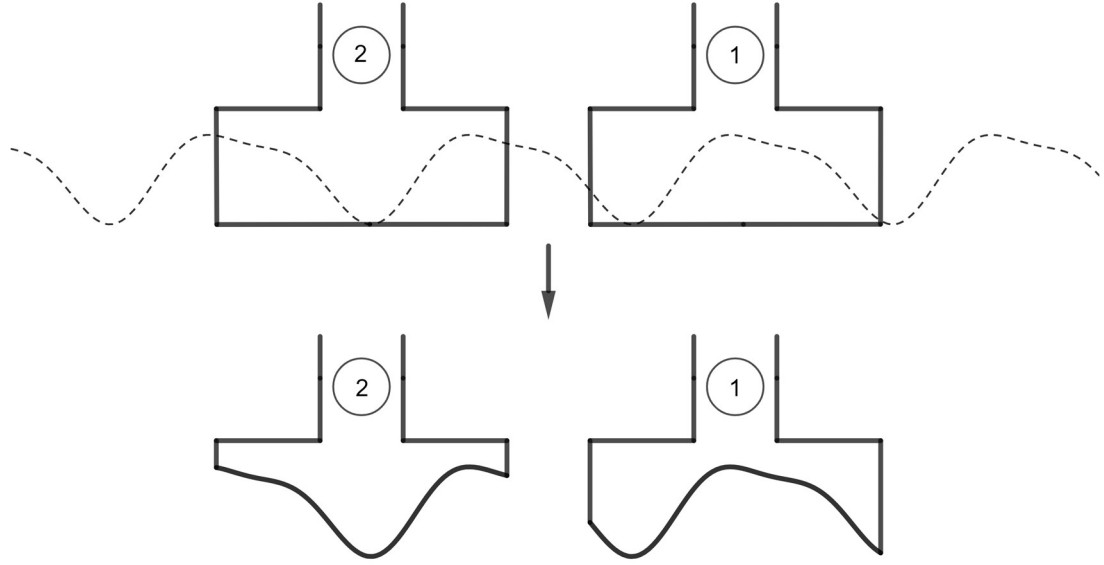


Figure 34. Example of two tooth tips shaped with two combined sinusoidal profiles.

$$\mathbf{x} = [\mathbf{A} \boldsymbol{\varphi}], \quad \mathbf{x} \in [0 A_{lim}]^{N_{sp}} \times [0 2\pi]^{N_{sp}} \quad (61)$$

where A_{lim} is the sinusoidal profiles amplitude upper bound, Moreover, the following constraint is introduced:

$$S(\alpha, \mathbf{A}, \boldsymbol{\varphi}) \leq A_{lim} \quad (62)$$

To ensure the manufacturing feasibility of the tooth tips shape, A_{lim} should be chosen minor or equal to half of the tooth tips height.

3.5.3. Heuristic Solution

Also in this case, to solve the optimization problem defined by (50), (61) and (62), a heuristic solution based on the use of ANN-based surrogate models and GA is adopted. However, in this case, a conventional single-training procedure is used, based on the following steps:

- sample data generation with TWM FEA;
- surrogate models training;

- choice of the best surrogate model;
- GA implementation on the chosen surrogate model;
- validation of the GA result by means of FEA.

The sample data generation is performed considering random samples of the design variables in the design space. The training of the surrogate models and the choice of the best surrogate model is based on the same logic adopted in the case of the TO. However, in this case, the choice of the best surrogate models is performed by means of a GA in which the design variables are N_{HL} and N_{HN} and the objective function is the mean squared estimation error on the validation data. Finally, the parameters of the GA implemented on the chosen surrogate model to minimize the cogging torque are the same reported in **Table 8**. In this case, the design variables are expressed by (61), the additional constraint is expressed by (62) and the objective function is expressed by (50).

3.5.4. Results

In **Table 20-Table 22** are reported the results obtained with 10 surrogate models trained with 100, 250, and 400 random samples, respectively. The APMSM with 20 stator segments has been considered and three sinusoidal profiles have been introduced to minimize the 2nd, 4th and 6th harmonics shown in **Figure 19 (b)**. The frequencies of the introduced sinusoidal profiles have been chosen in agreement with the design formula (56), i.e., 15.92 Hz, 31.83 Hz, and 47.75 Hz, respectively. For each surrogate model are reported information about the structure of the NN, (i.e., N_{HL} and N_{HN}), the validation error, the result of the GA implemented on the surrogate model (\mathbf{x}_{opt} , $f(\mathbf{x}_{opt})$), and the result of the FEA validation $f_{FEA}(\mathbf{x}_{opt})$. Note that the performances of the cogging torque optimization increase with the number of samples employed to train the surrogate models and outstanding results are achieved when 400 samples are employed.

In **Table 23-Table 25** are reported the results obtained with the same single-training procedure above described, using the method based on the TO. The comparison of the results achieved with the results reported in **Table 20-Table 22** shows that when a low number of samples are employed, the performances of the optimization are unsatisfactory in both cases. Instead, with the increase of the number of samples, the optimization based on the tooth tips sinusoidal shaping outperforms the TO. The main advantage of the optimization based on the tooth tips sinusoidal shaping is that the number of design variables depends only on the number of AHCs to be minimized while in the TO it increases with the period of the AHCs. A reduced number of design variables favors the integration of the second method proposed in this work with an optimization approach based on the use of surrogate models. Moreover, note that the comparison of the results reported in **Table 25** and in **Table 11** further demonstrates the effectiveness of the multi-training heuristic procedure described in **Figure 22**. In fact, this procedure ensures an average cogging torque reduction higher than 24.3% compared with the conventional single-training approach described in section 3.5.3, and with a computational time reduced by about 28%.

Finally, in **Table 26** are reported the results of the optimization performed by introducing two sinusoidal profiles in disagreement with the design formula (56). The frequencies chosen are 23.87 Hz and 39.79 Hz, which correspond to the frequencies of the 3rd and 5th harmonics in the harmonic spectrum shown in **Figure 19**. Note that in this case, a very high accuracy of the surrogate model is achieved. In particular, the error between the $f(\mathbf{x}_{opt})$ and $f_{FEA}(\mathbf{x}_{opt})$ is negligible. Despite the accuracy of the surrogate models, the performances of the optimization are very low since the introduced profiles cannot effectively interact with the cogging torque of the APMSM. These results definitely confirm the validity of the theoretical study and of the design formula (56).

Table 20. Results of the heuristic procedure with 100 random samples.

	N_{HL} x N_{HN}	Validation error [(Nm) ²]	$f(x_{opt})$ [Nm]	$f_{FEA}(x_{opt})$ [Nm]	Cogging Torque Reduction [%]	Average Cogging Torque Reduction [%]
1	4x4	4.028	6.049	8.369	8.3	
2	5x6	3.798	1.539	8.813	3.4	
3	3x4	0.663	0.803	8.529	6.5	
4	3x4	1.552	1.642	8.710	4.6	
5	5x4	0.745	2.344	8.812	3.4	
6	2x6	2.237	0.652	8.097	11.3	5.9
7	4x8	1.234	0.499	8.467	7.2	
8	2x4	0.445	0.882	8.608	5.7	
9	3x8	1.436	1.160	8.720	4.4	
10	5x4	0.454	0.611	8.712	4.5	

Table 21. Results of the heuristic procedure with 250 random samples.

	N_{HL} x N_{HN}	Validation error [(Nm) ²]	$f(x_{opt})$ [Nm]	$f_{FEA}(x_{opt})$ [Nm]	Cogging Torque Reduction [%]	Average Cogging Torque Reduction [%]
1	3x8	0.105	0.436	1.821	80	
2	3x14	0.144	0.275	0.932	89.8	
3	1x16	0.058	0.254	0.947	89.6	
4	1x18	0.200	0.042	1.224	86.6	
5	3x14	0.213	0.449	2.014	77.9	
6	2x14	0.081	0.571	2.125	76.7	85.3
7	2x12	0.255	0.375	0.523	94.3	
8	3x12	0.105	0.282	0.488	94.7	
9	3x12	0.178	0.670	1.597	82.5	
10	2x6	0.334	0.413	1.672	81.2	

Table 22. Results of the heuristic procedure with 400 random samples.

	N_{HL} x N_{HN}	Validation error [(Nm) ²]	$f(x_{opt})$ [Nm]	$f_{FEA}(x_{opt})$ [Nm]	Cogging Torque Reduction [%]	Average Cogging Torque Reduction [%]
1	3x12	0.130	0.074	1.311	85.6	
2	3x14	0.145	0.437	0.822	91.0	
3	3x12	0.057	0.195	0.529	94.2	
4	3x14	0.026	0.020	0.702	92.3	
5	3x14	0.157	0.410	0.389	95.7	
6	4x14	0.169	0.334	1.468	83.9	90.0
7	3x14	0.204	0.223	1.306	85.7	
8	2x14	0.056	0.160	1.848	79.7	
9	2x14	0.024	0.028	0.290	96.8	
10	3x14	0.031	0.300	0.491	94.6	

Table 23. Results of the heuristic procedure with 100 random samples using the TO.

	N_{HL} x N_{HN}	Validation error [(Nm) ²]	$f(x_{opt})$ [Nm]	$f_{FEA}(x_{opt})$ [Nm]	Cogging Torque Reduction [%]	Average Cogging Torque Reduction [%]
1	5x4	0.482	8.700	9.264	-1.5	
2	2x4	0.268	7.024	6.947	23.9	
3	2x2	0.431	8.565	7.282	20.2	
4	1x6	0.423	7.716	2.362	74.1	
5	2x4	0.272	7.983	6.582	27.9	
6	2x6	0.307	6.177	4.872	46.6	23.4
7	1x2	0.393	6.504	8.465	7.2	
8	3x4	0.288	7.598	8.655	5.2	
9	5x6	0.442	8.380	8.711	4.5	
10	2x6	0.270	6.707	6.755	26.0	

Table 24. Results of the heuristic procedure with 250 random samples using the TO.

	N_{HL} x N_{HN}	Validation error [(Nm) ²]	$f(x_{opt})$ [Nm]	$f_{FEA}(x_{opt})$ [Nm]	Cogging Torque Reduction [%]	Average Cogging Torque Reduction [%]
1	1x2	0.149	4.359	1.890	79.3	
2	1x2	0.112	4.169	2.407	73.6	
3	1x2	0.103	6.157	2.585	71.7	
4	1x2	0.227	6.639	2.224	75.6	
5	1x2	0.150	3.354	2.638	71.1	
6	1x2	0.259	8.396	6.542	28.3	67.0
7	1x2	0.182	5.647	2.089	77.1	
8	1x2	0.126	6.970	3.608	60.5	
9	1x10	0.261	6.587	3.172	65.2	
10	1x2	0.164	5.349	2.932	67.9	

Table 25. Results of the heuristic procedure with 400 random samples using the TO.

	N_{HL} x N_{HN}	Validation error [(Nm) ²]	$f(x_{opt})$ [Nm]	$f_{FEA}(x_{opt})$ [Nm]	Cogging Torque Reduction [%]	Average Cogging Torque Reduction [%]
1	2x4	0.135	3.074	2.959	67.6	
2	2x6	0.051	0.325	0.548	94.0	
3	2x8	0.126	4.277	1.889	79.3	
4	1x6	0.141	6.573	2.521	72.4	
5	1x2	0.110	6.517	8.190	10.3	
6	3x4	0.089	3.131	3.301	63.8	70.1
7	1x5	0.020	0.168	1.042	88.6	
8	1x4	0.191	0.363	1.509	83.5	
9	2x6	0.019	0.980	1.841	79.8	
10	1x2	0.224	7.700	3.523	61.4	

Table 26. Results of the heuristic procedure with 250 random samples in disagreement with the design formula.

	N_{HL} x N_{HN}	Validation error [(Nm) ²]	$f(x_{opt})$ [Nm]	$f_{FEA}(x_{opt})$ [Nm]	Cogging Torque Reduction [%]	Average Cogging Torque Reduction [%]
1	2x6	0.0028	7.093	7.135	21.8	
2	2x6	0.0032	7.026	7.210	21.0	
3	4x6	0.0009	7.164	7.160	21.5	21.6
4	3x8	0.0011	6.943	7.134	21.8	
5	5x8	0.0009	7.055	7.148	21.7	

3.6. Final considerations

Two novel design methods for the minimization of the cogging torque of PMSMs with modular stators have been presented. The first one is based on the topological optimization of multiple independent shapes of the tooth tips. The problem has been addressed with a semi-analytical approach. At first, by means of theoretical studies, a design formula has been developed, providing the number of the independent shapes to design based on the number of stator core segments and poles. Afterwards, the optimal shapes of the tooth tips have been achieved through a TO solved with an original and computationally-efficient multi-training heuristic procedure. This approach is based on a GA coupled with multilayer ANN-based surrogate models employed for the objective function evaluation. Substantial cogging torque reduction (>90%) are obtained with the proposed approach. The results demonstrate the validity of the developed design formula as well as the superiority of the proposed heuristic procedure over conventional approaches based on Gas directly coupled with FEA. A detailed comparison between the basic and optimized machines shows how the proposed method slightly reduces the average torque and the flux-linkage while there are no appreciable alterations in the flux-linkage THD and efficiency. Finally, a sensitivity analysis has been performed by considering manufacturing and

assembling tolerances with the non-UUM proving the robustness of the proposed approach.

The second method is based on the sinusoidal shaping of the stator tooth tips. Also in this case, the problem has been addressed with a semi-analytical approach. At first, an analytical study has been performed to derive the frequencies of the sinusoidal profiles to be introduced. Later, a conventional single-training heuristic procedure based on the use of a GA and multilayer ANN-based surrogate models has been adopted to optimize the amplitude and phase shift of the sinusoidal profiles. The results show a remarkable reduction of the cogging torque (>90%), proving the validity of the analytical studies.

A comparison between the two methods shows that the one based on the sinusoidal shaping of the tooth tips ensure better performances with the same computational effort. Moreover, the results show that the proposed multi-training heuristic procedure adopted to solve the TO is computationally more efficient than the conventional single-training one.

3.7. Publications

Part of the contents and results presented in this chapter have been published in [109] and [110].

4. Automated offline parameter identification of PMSMs

4.1. Introduction and State of the Art

PMSMs performances are subject to degradation due to aging, vibrations, overtemperature and overcurrents. However, thanks to the parameter identification the conditions of the PMSMs can be monitored and faults can be detected and prevented. For instance, variations in the electrical parameters such as dq -axis inductances, stator winding resistance and rotor flux linkage can detect inter-turn short circuits, demagnetization, or permanent magnet failures [111], [112].

To identify the parameters of PMSMs, offline or online approaches are employed. Offline approaches identify the parameters based on previously collected input/output data through dedicated tests with the machine usually disconnected from its load [113], [114]. While ensuring high accuracy, this approach needs specific laboratory equipment and human effort. Unfortunately, condition monitoring and fault diagnosis of PMSMs require periodic updates of the identified parameters, making offline methods not suitable for large-scale applications with many operating machines. Instead, online methods identify the PMSM parameters during its on-load operation using real-time implementations on the drive control unit. Existing online methods are mainly implemented using Adaline NNs [111], [115], [116], recursive least squares (RLS) [117], [118], evolutionary algorithms (EA) [112], [119]-[121], extended Kalman filter (EKF) [122], [123] model reference adaptive systems (MRAS) [124], and observer-based methods [125], [126].

The accuracy of existing online identification schemes is jeopardised by the rank-deficiency issue, i.e., the number of unknown parameters is higher than the

rank of the PMSM model, thus preventing accurate and simultaneous parameter identifications [111], [120]. Reducing the number of unknown parameters by setting some of them to nominal values is a possible solution [123], [127]. However, variations in PMSM operating conditions, aging and faults can increase the difference between nominal and actual values, thus adversely affecting the identification accuracy. Moreover, in large-scale multi-machine processes, the nominal value of each parameter may be difficult to retrieve. Alternatively, the rank of the model can be increased by using additional equipment, such as thermal sensors [128] and torque meters [129]. Clearly, costs, complexity, and risk of failures would be increased. Signal injection represents another solution to increase the rank of the system. For instance, current ([112], [116]-[121]), voltage ([130], [131]), and rotor position ([111], [120]) offsets signals are injected. However, to provide accurate estimations, high signal-to-noise ratios must be ensured in case of current or voltage injections, thus affecting system efficiency and stability while influencing the parameters to be identified [111], [120]. Moreover, custom control actions on the PMSM drive are required to implement signal injection, making such approach impractical in applications where many different commercial drives are present.

Generally, dq -axis reference voltages are employed in place of actual phase voltages, which are usually not measured. Hence, the estimation accuracy is further reduced due to the mismatch between reference and actual phase voltages, caused mainly by actuation delays and inverter nonlinearity (i.e., voltage drops on power devices and dead-time effect) [132]-[136]. The inverter nonlinearity can be compensated through an additional parameter in the PMSM model, i.e., the distorted voltage, which rarely overcomes $1.5 V$ [111], [112], [117]-[121], [128], [129]. Instead, to the author's best knowledge, the compensation for identification purposes of the actuation delay, i.e., the delay introduced by the digital implementation of the current regulators and by the PWM logic, has not yet received attention. While affecting the estimation of the

rotor flux linkage and stator resistance, the voltage distortion caused by the inverter nonlinearity does not affect the estimation of the q -axis inductance when the d -axis current is controlled to zero [135]. Instead, as it will be shown next, the actuation delay can also jeopardize the estimation accuracy of L_q during a zero d -axis current control and may have a greater impact on the identification of the rotor flux linkage and stator resistance. The voltage distortion due to the actuation delay increases as the ratios between electrical rotor speed and control sampling frequency increases, i.e., when high-speed PMSMs or PMSMs with a high number of poles are considered. It is worth mentioning how the main results of identification procedures relying on reference voltages show experiments with rotor speeds below 400 r/min , where the effects of actuation delays are negligible [111], [112], [115], [117]-[121], [124], [127], [128], [130].

Overcoming the limitations of existing solutions, the author proposes a novel approach highly suitable for large-scale industrial processes. Costs, machine downtimes, and human efforts are critical parameters to be minimized. Thus, realistic scenarios are considered, where:

- dedicated laboratory tests are not allowed;
- additional sensors (e.g., phase voltage transducers, thermal or torque sensors) are not allowed;
- the implementation of custom algorithms (e.g., signal injections, alteration of the PMSM on-load ordinary operations) on the drive is not allowed;
- nominal values of the parameters are not available.

The PMSM drives are employed just as measurement collectors. Then, collected data is processed offline by the proposed automated algorithm which provides rotor flux linkage, stator resistance and inductance estimations. By exploiting the data obtained in multiple operating conditions, the problem of rank deficiency is overcome without requiring additional sensors, nominal

values, or signal injections. Moreover, the actuation delay is also compensated ensuring accuracy in medium and high frequency applications as well.

Since the proposed method fits in large-scale applications, relies only on easily accessible data and does not require machine downtimes or custom drive programs, it is highly suitable for cloud computing implementations. In principle, the data coming from the PMSM drives during regular working operations are collected and stored on a cloud data lake, ready for further analysis. Code implementation, update, and maintenance is easier and more effective on a cloud environment in place of the control drive, where limitations are almost always present. Increasing efforts in developing cloud-oriented identification algorithms are required, as the advantages of a cloud implementation cannot be overlooked: it enables correlations and long-term analysis for predictive maintenance, cross-machines analysis, and implementation of digital twins without computational constraints.

4.2. PMSM Model with Actuation Delay

The steady-state equations of a PMSM in the dq -axis reference frame when the d -axis current is zero are

$$u_{dq} = \begin{bmatrix} u_d \\ u_q \end{bmatrix} = \begin{bmatrix} -L_q \omega i_q \\ R_s i_q + \psi_{PM} \omega \end{bmatrix} \quad (63)$$

The three unknown parameters, i.e., L_q , R_s , ψ_{PM} , cannot be identified simultaneously as the rank of (63) is at most two.

Since voltage measurements are usually not available, the dq -axis voltage reference, i.e., u_{dq}^* , is employed in place of u_{dq} , compromising the accuracy of the parameter identification. In particular, the distortion introduced by the actuation delay is considered. The actuation delay of u_{dq}^* is composed by the

time delay due to the digital implementation of the current control and the time delay due to the PWM logic. While the former is equal to a sampling period of the regulator [136], i.e., T_s , the latter is assumed to be half-sampling period [136], [137]. Hence, an actuation delay of $1.5 T_s$ is obtained. During this period $u_{dq}^*(k-1)$ is fixed in the stationary reference frame while the synchronous frame rotates, as shown in **Figure 35**. Thus, the actual voltages at the instant $(k+0.5)T_s$ are expressed by the components of the voltage references vector in the synchronous frame:

$$u_{dq}((k+0.5)T_s) = \begin{bmatrix} \cos(\Delta\theta) & \sin(\Delta\theta) \\ -\sin(\Delta\theta) & \cos(\Delta\theta) \end{bmatrix} u_{dq}^*((k-1)T_s) \quad (64)$$

where $\Delta\theta$ is the rotor angular displacement during to the actuation delay time.

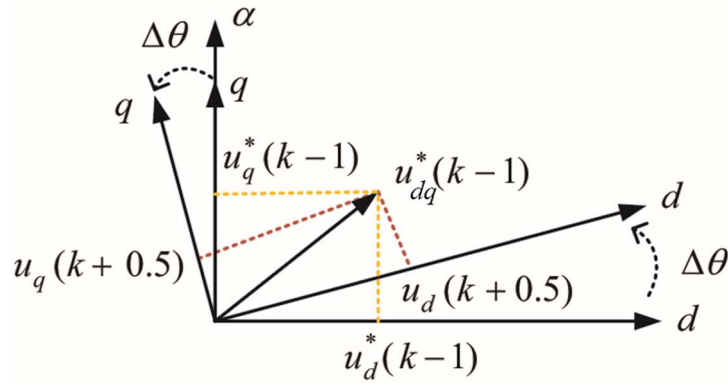


Figure 35. Diagram of voltage vectors.

By assuming constant speed during this period, it results that

$$\Delta\theta = \frac{3}{2}(\theta(k) - \theta(k-1)) \quad (65)$$

The author defines *compensated voltages* at time step k , i.e., $\tilde{u}_d(kT_s)$ and $\tilde{u}_q(kT_s)$, as the components of u_{dq} in (64).

Using (63)-(65) and assuming $\omega(kT_s) \approx \omega((k + 0.5)T_s)$ and $i_q(kT_s) \approx i_q((k + 0.5)T_s)$, the following model is established:

$$\begin{bmatrix} \tilde{u}_d(k) \\ \tilde{u}_q(k) \end{bmatrix} = \begin{bmatrix} -L_q \omega(k) i_q(k) \\ R_s i_q(k) + \psi_{PM} \omega(k) \end{bmatrix} \quad (66)$$

where T_s is omitted for the sake of brevity. Note that the compensated voltages can be calculated from (64) and (65) using only the samples of the rotor position and of the voltage references.

4.3. Proposed Automated Offline Parameter identification

Figure 36 summarizes the proposed PMSM automated offline parameter identification procedure. An SPMSM drive with a zero d -axis current control is considered. No ad hoc tests or alterations of the machine operations are performed to collect the measurement data. In particular, the author assumes that electrical rotor position and speed, the q -axis current and the voltage references are the available variables. Thus, the compensated voltages can be calculated using (64) and (65). An edge/cloud computing architecture like the one proposed in [138] can be adopted for the data collection and storage. The three phases of the offline data post-processing are described in the following subsections.

4.3.1. SPMSM Steady-States Identification

The proposed identification method is based on the model (66), which is valid only during the SPMSM steady states. Therefore, in the first phase of the offline application, the R-statistic algorithm is adopted to detect the SPMSM. R-statistic is a statistical method developed to automatically distinguish transient states from steady states in noisy processes. This method is based on the computation of the following statistical index [139]:

$$R_{\chi}(k) = 2 \frac{\sum_{i=k-N_w}^k \chi_n(i)^2 - \frac{1}{N_w} \left(\sum_{i=k-N_w}^k \chi_n(i)\right)^2}{\sum_{i=k-N_w+1}^k (\chi_n(i) - \chi_n(i-1))^2} \quad (67)$$

where R_{χ} is the index for the generic variable χ and N_w is the length of the moving window. χ_n is computed as follows:

$$\chi_n(k) = \chi(k) + w_{\chi}(k) \quad (68)$$

where w_{χ} is the noise signals based on the Box–Muller method:

$$w_{\chi}(k) = \sigma_{\chi}(k) \sqrt{-2 \ln(r_1(k))} \sin(2\pi r_2(k)) \quad (69)$$

in which σ_{χ} is the standard deviation, while r_1 and r_2 are independent samples chosen from the uniform distribution in the interval $[0, 1]$. The noise signals are introduced to avoid numerical issues [139].

R_{χ} tend to be around 1 as the process tends to the steady state. Instead, during transients, the indices are expected to be greater than 1. Hence, the process is in the steady state if $R_{\chi} \leq R_{crt}$, where R_{crt} is a critical threshold. In [139], the author suggests manually tuning R_{crt} according to the actual responses. R_{crt} , N_w , and σ_{χ} , are the tuning parameters of the R-statistic algorithm found with trial-and-error approach. The tuning of these parameters does not need to be repeated for different electrical drives since they do not depend upon physical parameters of the machine. This fact ensures the repeatability of the method in large scale applications limiting the human effort. To identify the SPMSM steady states, the R-statistic algorithm is applied to i_q and ω . The SPMSM is considered at steady state at the k -th sample only if $R_{i_q}(k) \leq R_{crt}$ and $R_{\omega}(k) \leq R_{crt}$.

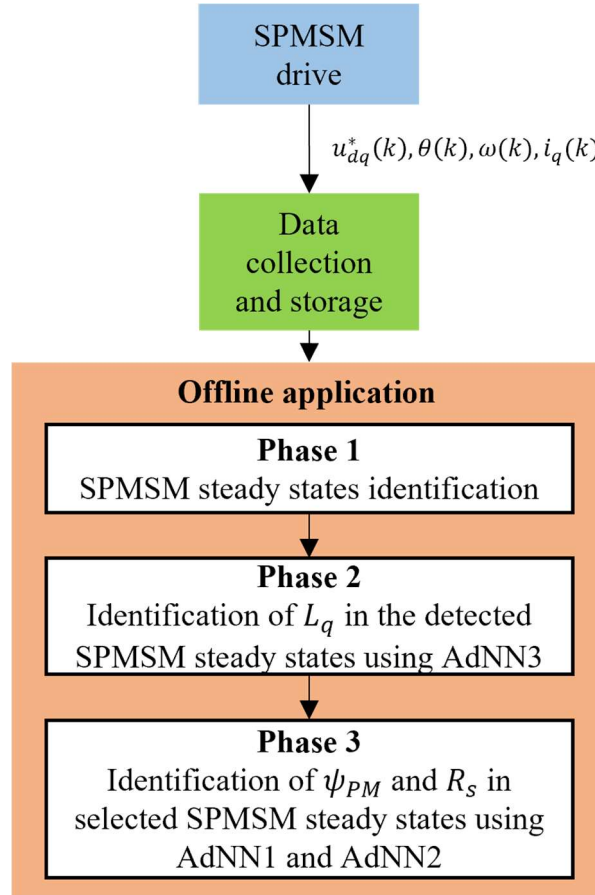


Figure 36. Parameter identification procedure.

4.3.2. Identification of the q -Axis Inductance

In the second phase, L_q is identified in each detected SPMSM steady state using an Adaline NN, called AdNN3. Note that the identification of L_q can be performed independently from ψ_{PM} and R_s , as can be deduced by the first equation of the model (66).

AdNN3 is based on the following equations:

$$\hat{L}_q(k) = \hat{L}_q(k-1) + 2\eta_{L_q}(k)\omega(k)i_q(k)(\tilde{u}_d(k) - \hat{u}_d(k)) \quad (70)$$

$$\hat{u}_d(k) = -\omega(k)i_q(k)\hat{L}_q(k-1) \quad (71)$$

$$\eta_{L_q}(k) = \frac{k_{L_q} - 1}{2\omega(k)^2 i_q(k)^2} \quad (72)$$

Note that ω and i_q are the inputs of AdNN3, \hat{u}_d is the estimated d -axis voltage, i.e., the output of AdNN3, \hat{L}_q is the estimated q -axis inductance, i.e., the only weight of AdNN3, η_{L_q} is the learning rate, and k_{L_q} is a real constant in the interval $[-1, 1]$. Equation (70) is the formula for updating the weight of AdNN3, which is an Adaline NN with a single neuron. Equation (72) automatically update the learning rate at each sample time to ensure the convergence of the estimations provided by AdNN3. In fact, by substituting (71) in (70), the following first-order difference equation is obtained:

$$\hat{L}_q(k) = \hat{L}_q(k-1) \left[1 + 2 \eta_{L_q}(k) \left(\omega(k) i_q(k) \right)^2 \right] + 2 \eta_{L_q}(k) \omega(k) i_q(k) \tilde{u}_d(k) \quad (73)$$

The solution of the homogeneous equation associated to (73) is

$$\hat{L}_{qh}(k) = c \left[1 + 2 \eta_{L_q}(k) \left(\omega(k) i_q(k) \right)^2 \right]^k, \quad c \in \mathbb{R} \quad (74)$$

Therefore, (72) is derived from the convergence condition:

$$\left| 1 + 2 \eta_{L_q}(k) \left(\omega(k) i_q(k) \right)^2 \right| < 1 \quad (75)$$

4.3.3. Identification of the Rotor Flux Linkage and Stator Resistance

In the last phase, ψ_{PM} and R_s are identified on selected SPMSM steady states using two coupled Adaline NNs, called AdNN1 and AdNN2, respectively. AdNN1 is based on the following equations:

$$\hat{\psi}_{PM}(k) = \hat{\psi}_{PM}(k-1) + 2 \eta_{\psi_{PM}}(k) \omega(k) (\tilde{u}_q(k) - \hat{u}_q(k)) \quad (76)$$

$$\hat{u}_q(k) = \hat{R}_s^*(j-1) i_q(k) + \hat{\psi}_{PM}(k-1) \omega(k) \quad (77)$$

$$\eta_{\psi_{PM}}(k) = \frac{1 - k_{\psi_{PM}}}{2\omega(k)^2} \quad (78)$$

In these equations, ω and i_q are the inputs of AdNN1, \hat{u}_q is the estimated q -axis voltage, i.e., the output of AdNN1, $\hat{\psi}_{PM}$ is the estimated rotor flux linkage, i.e., the only weight of AdNN1, $\eta_{\psi_{PM}}$ is the learning rate, and $k_{\psi_{PM}}$ is a real constant in the interval $[-1, 1]$. \hat{R}_s^* is the provisional stator resistance estimation provided by AdNN2 and is constant during the operation of AdNN1. The way in which \hat{R}_s^* is updated is described below.

Moreover, AdNN2 is based on the following equations:

$$\hat{R}_s(k) = \hat{R}_s(k-1) + 2 \eta_{R_s}(k) i_q(k) (\tilde{u}_q(k) - \hat{u}_q(k)) \quad (79)$$

$$\hat{u}_q(k) = \hat{R}_s(k-1) i_q(k) + \hat{\psi}_{PM}^*(j) \omega(k) \quad (80)$$

$$\eta_{R_s}(k) = \frac{1 - k_{R_s}}{2i_q(k)^2} \quad (81)$$

In these equations, ω and i_q are the inputs of AdNN2, \hat{u}_q is the estimated q -axis voltage, i.e., the output of AdNN2, \hat{R}_s is the estimated rotor flux linkage, i.e., the only weight of AdNN2, η_{R_s} is the learning rate, and k_{R_s} is a real constant in the interval $[-1, 1]$. $\hat{\psi}_{PM}^*$ is the provisional stator resistance estimation provided by AdNN1 and is constant during the operation of AdNN2. Also, the way in which $\hat{\psi}_{PM}^*$ is updated is described below. Note that (78) and (81) have been derived as (72).

The second equation of the model (66) shows that the identification of ψ_{PM} and R_s cannot be performed simultaneously using only a steady state due to the rank-deficiency issue. To overcome this issue, the author proposes to feed AdNN1 and AdNN2 with measurement data of two different SPMSM steady states. The author denotes SS1 and SS2 the steady states used to feed AdNN1 and AdNN2, respectively. The criterion adopted for the choice of SS1 and SS2 is discussed later. Moreover, to overcome the rank-deficiency issue, AdNN1 and AdNN2 are coupled using the approach described in **Algorithm 1**. After the initialization phase, at the j -th step, a rotor flux linkage and a stator resistance estimation is performed and the values of the provisional estimations $\hat{\psi}_{PM}^*$ and \hat{R}_s^* are updated. The provisional estimations are set equal to the last value of the estimations provided by AdNN1 and AdNN2 at the j -th step. This operation allows to couple the Adaline NNs, as shown by (77) and (80). The estimations \hat{R}_s and $\hat{\psi}_{PM}$ can be considered at the steady state when the last value is chosen to update the provisional estimations. The process is cyclically repeated until the stop criterion is satisfied, i.e.:

$$\left| \frac{\hat{\psi}_{PM}^*(j) - \hat{\psi}_{PM}^*(j-1)}{\hat{\psi}_{PM}^*(j-1)} \right| < \varepsilon \quad \wedge \quad \left| \frac{\hat{R}_s^*(j) - \hat{R}_s^*(j-1)}{\hat{R}_s^*(j-1)} \right| < \varepsilon \quad (82)$$

where ε is an arbitrary constant. Note that SS1 and SS2 are fixed during the execution of **Algorithm 1**.

Algorithm 1. Operation of the coupled Adaline NNs

1. **Choice of SS1 and SS2**
 2. **Provisional estimations initialization**
Set $\hat{\psi}_{PM}^*(0) = 0$, $\hat{R}_s^*(0) = 0$, and $j = 1$.
 3. **Rotor flux linkage identification**
 - a. Set $\hat{\psi}_{PM}(0) = \hat{\psi}_{PM}^*(j - 1)$
 - b. Use AdNN1 to identify ψ_{PM} on SS1
 - c. Set $\hat{\psi}_{PM}^*(j) = \hat{\psi}_{PM}(end)$
 4. **Stator resistance identification**
 - d. Set $\hat{R}_s(0) = \hat{R}_s^*(j - 1)$
 - e. Use AdNN2 to identify R_s on SS2
 - f. Set $\hat{R}_s^*(j) = \hat{R}_s(end)$
 5. **Convergence check**
If (82) is satisfied then stop, otherwise set $j = j + 1$ and go back to step 3.
-

4.3.4. Convergence Analysis

In this section, a convergence analysis of the **Algorithm 1** is carried out. Let be \tilde{u}_{q1} , i_{q1} and ω_1 the q -axis voltage, current and the electrical rotor speed during SS1. By substituting (77) in (76), a first-order difference equation is obtained. The steady-state solution of this equation at the j -th step of AdNN1 is:

$$\hat{\psi}_{PM}^*(j) = \hat{\psi}_{PM}(end) \approx \hat{\psi}_{PM}(\infty) = \frac{\tilde{u}_{q1} - \hat{R}_s^*(j - 1) i_{q1}}{\omega_1} \quad (83)$$

Neglecting measurements error and considering (66), \tilde{u}_{q1} can be expressed as:

$$\tilde{u}_{q1} = R_{s1} i_{q1} + \psi_{PM1} \omega_1 \quad (84)$$

where R_{s1} and ψ_{PM} are the actual values of the stator resistance and rotor flux linkage in the SS1. By substituting (84) in (83):

$$\hat{\psi}_{PM}^*(j) = \frac{R_{s1}i_{q1} + \psi_{PM1}\omega_1 - \hat{R}_s^*(j-1)i_{q1}}{\omega_1} \quad (85)$$

By repeating the same procedure for the stator resistance estimated at the $(j - 1)$ -th step by AdNN2 during SS2:

$$\hat{R}_s^*(j-1) = \frac{R_{s2}i_{q2} + \psi_{PM2}\omega_2 - \hat{\psi}_{PM}^*(j-1)\omega_2}{i_{q2}} \quad (86)$$

By substituting (86) in (85), the following first-order difference equation is achieved:

$$\hat{\psi}_{PM}^*(j) = \psi_{PM1} + \left[R_{s1} - R_{s2} + (\hat{\psi}_{PM}^*(j-1) - \psi_{PM2}) \frac{\omega_2}{i_{q2}} \right] \frac{i_{q1}}{\omega_1} \quad (87)$$

The solution of this equation is:

$$\hat{\psi}_{PM}^*(j) = c \left(\frac{i_{q1}\omega_2}{i_{q2}\omega_1} \right)^j + \hat{\psi}_{PM}^*(\infty), \quad j \geq 1 \quad (88)$$

where c is a constant and

$$\hat{\psi}_{PM}^*(\infty) = \psi_{PM1} + (\psi_{PM1} - \psi_{PM2}) \frac{r}{1-r} + (R_{s1} - R_{s2}) \frac{i_{q1}/\omega_1}{1-r} \quad (89)$$

with

$$r = \frac{i_{q1}\omega_2}{i_{q2}\omega_1} \quad (90)$$

By substituting (88) in (86), the following expression is achieved:

$$\hat{R}_s^*(j) = -c \frac{\omega_2}{i_{q2}} \left(\frac{i_{q1}\omega_2}{i_{q2}\omega_1} \right)^j + \hat{R}_s^*(\infty), \quad j \geq 1 \quad (91)$$

where

$$\hat{R}_s^*(\infty) = R_{s2} + (R_{s2} - R_{s1}) \frac{r}{1-r} + (\psi_{PM} - \psi_{PM}) \frac{\omega_2/i_{q2}}{1-r} \quad (92)$$

Equations (88) and (91) shows that, to ensure the convergence of the stator resistance and rotor flux linkage estimations, SS1 and SS2 should be selected to satisfy the following condition:

$$|r| = \left| \frac{i_{q1}\omega_2}{i_{q2}\omega_1} \right| < 1 \quad (93)$$

Equation (93) expresses the convergence condition of **Algorithm 1**.

4.3.5. Analysis and Minimization of the Estimation Errors

If the convergence condition (93) is satisfied, the values of the provisional estimations achieved by means of **Algorithm 1** are expressed by (89) and (92). The analysis of (89) and (92) shows that the estimations are affected by errors caused by the variations of ψ_{PM} and R_s in SS1 and SS2. For convenience, (89) and (92) can be rewritten as

$$\hat{\psi}_{PM}^*(\infty) = \psi_{PM1} + \varepsilon_\psi \quad (94)$$

$$\hat{R}_s^*(\infty) = R_{s1} + \varepsilon_R \quad (95)$$

with

$$\varepsilon_\psi = (\psi_{PM1} - \psi_{PM}) \frac{r}{1-r} + (R_{s1} - R_{s2}) \frac{i_{q1}/\omega_1}{1-r} \quad (96)$$

$$\varepsilon_R = (R_{s2} - R_{s1}) \frac{r}{1-r} + (\psi_{PM} - \psi_{PM1}) \frac{\omega_2/i_{q2}}{1-r} \quad (97)$$

Note that if an ideal SPMSM with constant parameters were considered, then $\psi_{PM} = \psi_{PM} = \psi_{PM}$ and $R_{s1} = R_{s2} = R_s$ and the estimations would be affected only by the presence of measurement errors. However, in a real PMSM, the values of the parameters vary with the operating condition and the errors expressed by (96) and (97) cannot be neglected. The methods which overcome the rank deficiency issue by means of the signal injection, aim to design additional steady states of the PMSM. In particular, the steady states are properly designed to minimize the variations of the parameters to be identified ensuring low estimation errors. Unfortunately, in the scenario considered in this work, this approach cannot be adopted and the only way to minimize the estimation errors is to properly select SS1 and SS2 among the available SPMSM steady states.

To minimize ε_ψ and ε_R , the following assumptions are made:

- $\psi_{PM} = \psi_{PM}(\Theta)$. The dependence on Θ is caused by the demagnetization effect of the temperature;
- $R_s = R_s(|\omega|, \Theta)$. The dependence on ω is caused by the skin and proximity effect while the dependence on Θ is caused by resistivity variation with the temperature;

- $\Theta = \Theta(|i_q|)$. The temperature depends only on the intensity of the currents;
- the effects of frequency variations higher than 100 Hz on the stator resistance are dominant compared to effects of the temperature variations. In fact, an increase of temperature of 100 °C causes an increase of the resistance of copper windings by about 70% compared to the value at room temperature. Instead, an increase of frequency higher than 100 Hz can increase the stator resistance over 100% compared to the DC value [140]-[143].

Under these assumptions, considering (96) and (97), the following criteria are established to select SS1 and SS2:

- **Criterion 1:** Should be $|r| < 1/2$, or minimize $|r|$ otherwise;
- **Criterion 2:** Should be $||\omega_1| - |\omega_2|| < 100 \cdot 2\pi$ or minimize $||\omega_1| - |\omega_2||$ otherwise;
- **Criterion 3:** Minimize $|r|$;
- **Criterion 4:** Minimize $||i_{q1}| - |i_{q2}||$;
- **Criterion 5:** Minimize $||\omega_1| - |\omega_2||$.

On the basis of the assumptions and criteria established, two different procedures are proposed to optimally select the SPMSM steady states. The first one is shown in **Figure 37** and allows to optimally select SS2 to minimize the estimation errors of ψ_{PM} . In this case SS1 is arbitrarily chosen among the available steady states. In particular, ψ_{PM} is considered dominant if $\psi_{PM} > 10R_S i_{q1}/\omega_1$. Instead, R_S is considered dominant if $R_S i_{q1}/\omega_1 > 10\psi_{PM}$. The second one is shown in **Figure 38** and allows to optimally select SS1 to minimize the estimation errors of R_S . In this case SS2 is arbitrarily chosen among the available steady-state and ψ_{PM} is considered dominant if $\psi_{PM}\omega_2/i_{q2} > 10R_S$. Instead, R_S is considered dominant if $R_S > 10\psi_{PM}\omega_2/i_{q2}$.

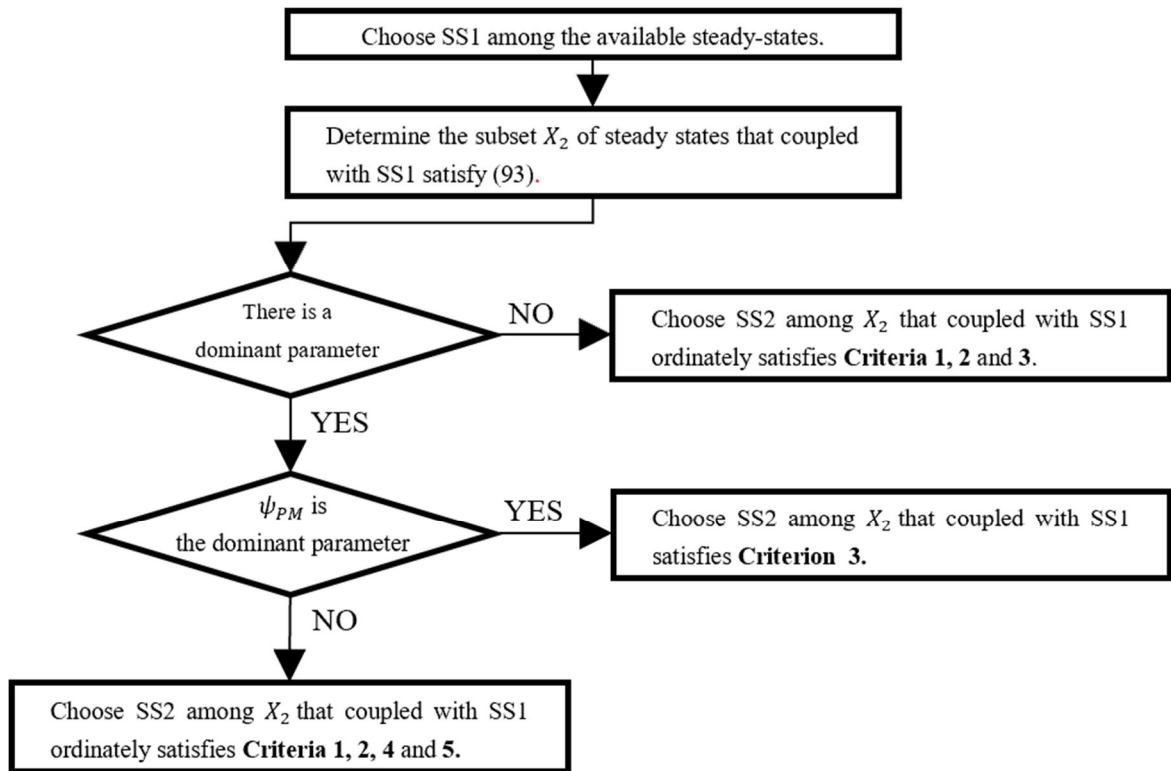


Figure 37. Identification of ψ_{PM} : procedure for the optimal choice of SS2.

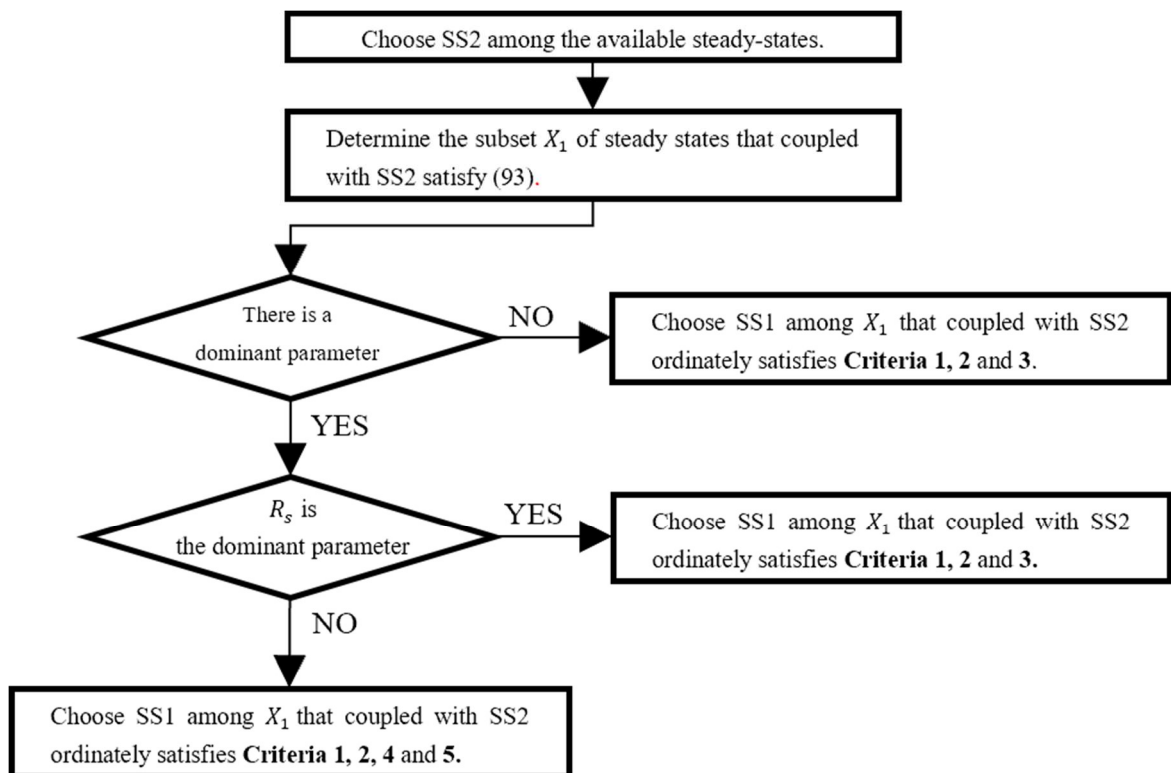


Figure 38. Identification of R_s : procedure for the optimal choice of SS1.

Before the implementation of the two procedures, the author proposes to perform a parameter identification by choosing SS1 and SS2 that minimize $|r|$.

This first parameter identification is needed to provide parameter estimations to detect the presence of dominant parameters.

4.4. Simulation Results

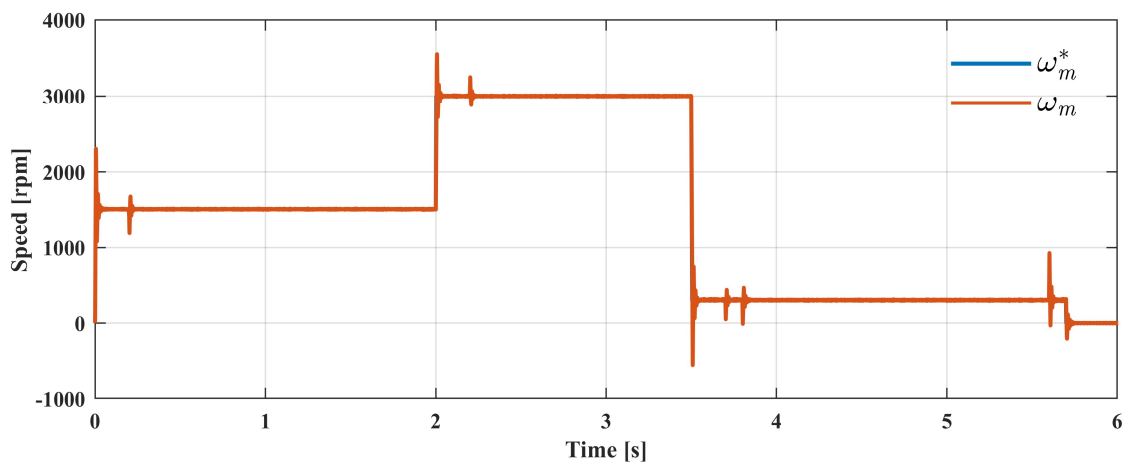
In this section are reported the results obtained by means of the application of the proposed method to data provided by the simulation of an SPMSM drive in Simulink environment. The values of the main parameters of the model are reported in **Table 27**.

Table 27. SPMSM drive parameters.

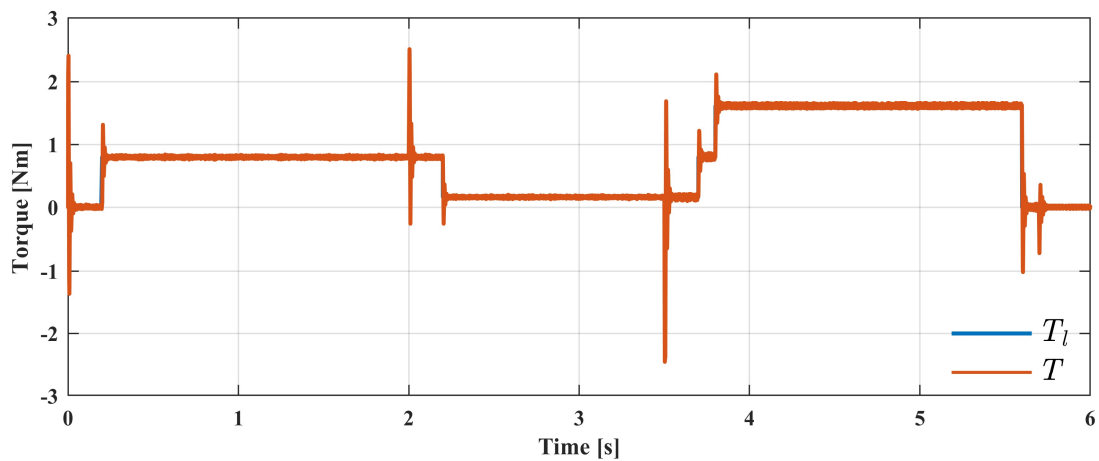
Parameters	Value
Rated power	0.5 kW
Rated current	1.33 A
Rated mechanical speed	3000 rpm
n_p	4
R_s	13.155 Ω
L_q	39.75 mH
ψ_{PM}	0.21 Wb
Phase current uncertainty	± 0.65 %
DC voltage uncertainty	± 0.8 %
Switching frequency	10 kHz
T_s	10^{-4} s

In particular, an SPMSM driven by an FOC controller and fed by a PWM three-phase inverter has been modeled. The FOC controller performs a speed control with zero d -axis current and is made by the cascade of speed and current PI regulators. In this model, the inverter nonlinearity is negligible while measurement uncertainties are added to the phase currents and on the DC-link voltage measurements. These uncertainties have been introduced considering datasheets of commercial transducers, i.e., LEM LA 55-P for the phase current transducers and LEM LV 25–1000 for the DC-link voltage transducer.

Moreover, a resolver has been modeled to provide rotor speed and angular position measurements. The SPMSM model with wye-wound stator is configured as a Bonfiglioli BMD 400V 65 surface magnet motors. The motors and inverter parameters are constant during the simulation. The model is used to simulate, at fixed sampling time step, a working cycle of six seconds with variable speed and load torque, as shown in **Figure 39**. This working cycle has been designed to obtain multiple operating conditions to be exploited by the proposed algorithm.



(a)

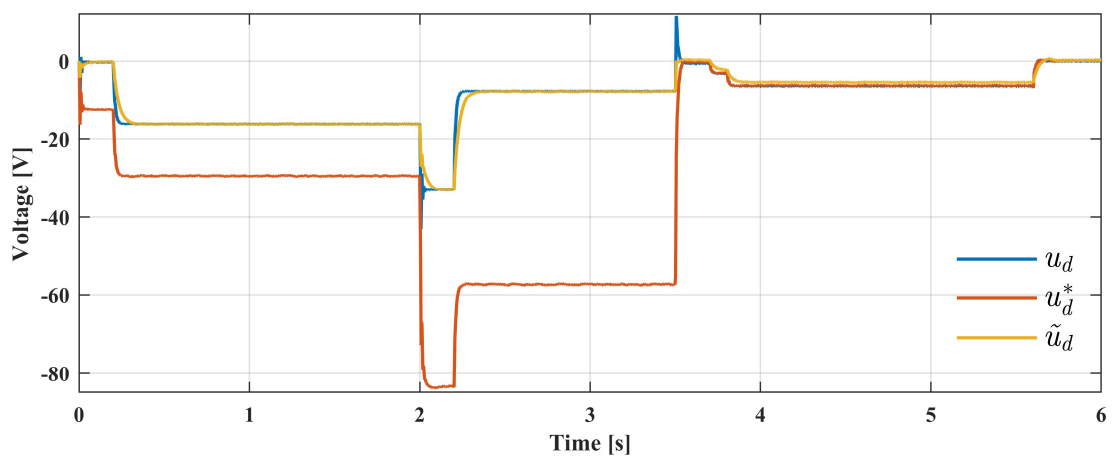


(b)

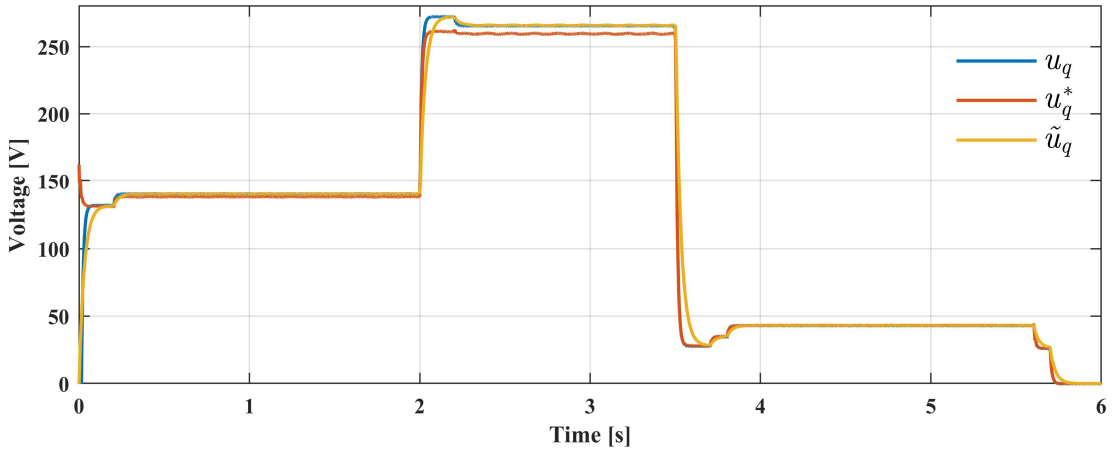
Figure 39. SPMSM working cycles: (a) Mechanical speed reference and actual speed; (b) Electromagnetic and load torque.

Figure 40 shows the voltage references, the actual voltages, and the compensated voltages. Note that the voltage references have been filtered with

a low-pass filter to eliminate the high-frequency harmonics generated by the PWM. In **Figure 41**, instead, the errors between the actual voltages and the voltage references and between the actual and the compensated voltages are reported. Note that, except for transients, the compensated voltages ensure a very good approximation of the actual voltages with errors lower than 1 V. The error of the voltage references is unacceptable, especially considering the d -axis voltage. In particular, in accordance with the theory, the error between the actual voltages and the voltage references increases during the high-speed operations of the SPMSM, as can be deduced by comparing **Figure 41** with **Figure 39 (a)**.

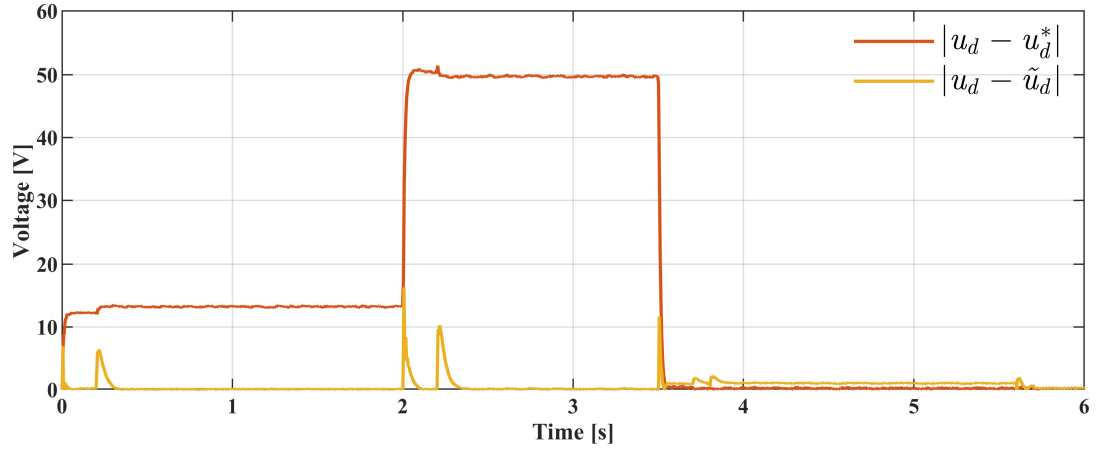


(a)

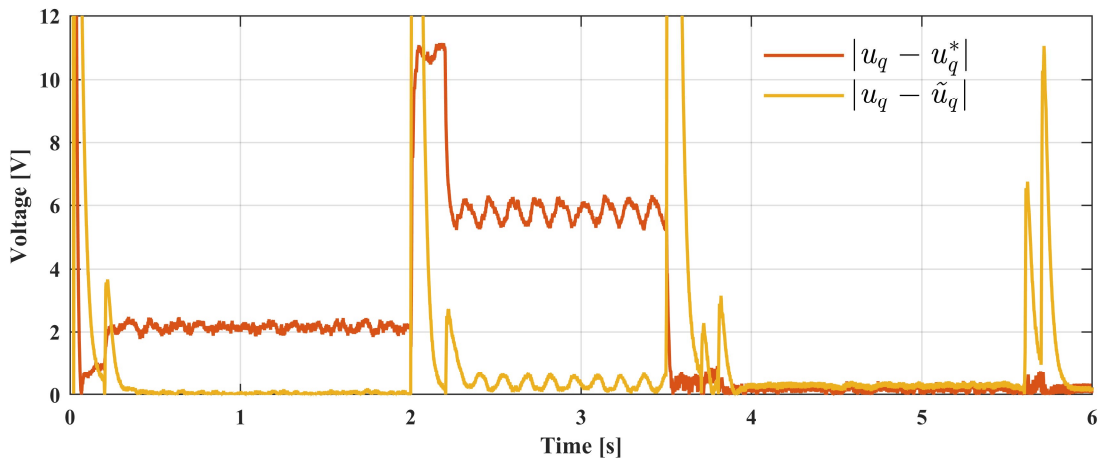


(b)

Figure 40. SPMSM voltages: (a) d -axis voltages; (b) q -axis voltages.



(a)



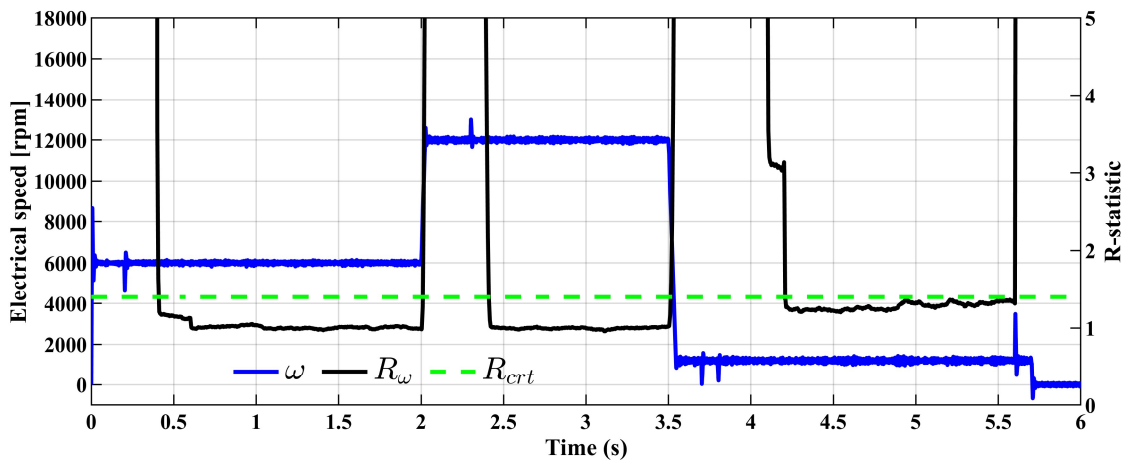
(b)

Figure 41. Voltage errors: (a) d -axis voltage errors; (b) q -axis voltage errors.

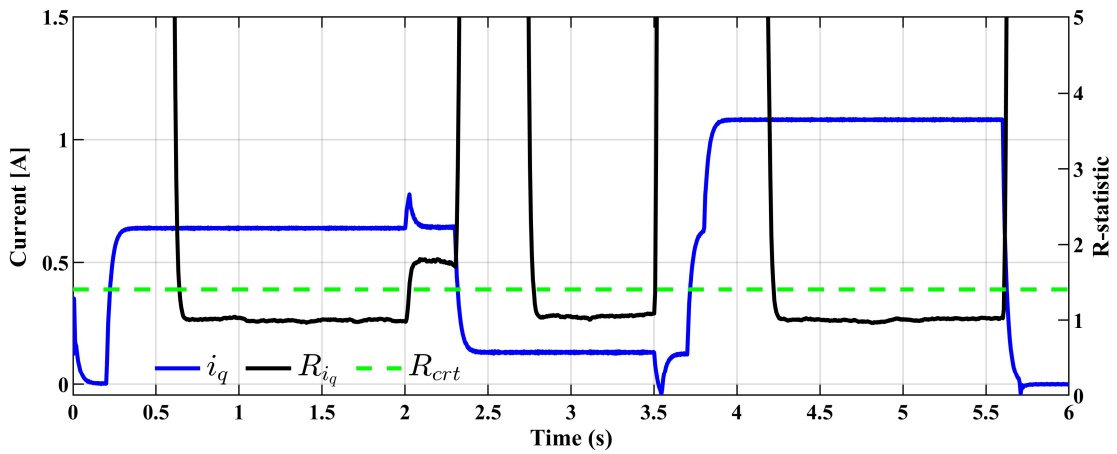
These results demonstrate the validity of the proposed voltages compensation based on (64) and (65).

Figure 42 shows the results of the R-statistic analysis, identifying the rotor speed and q -axis current steady states of the motor. The values of the R-statistic parameters used to achieve these results are reported in **Table 28**. In this figure, the R_ω , R_{i_q} and the critical value R_{crt} are shown. Note that the values of R_ω , R_{i_q} and R_{crt} are reported on the right y-axis of the figure. As expected, R_ω and R_{i_q} are greater than R_{crt} during the transient states, while are smaller than R_{crt} once the steady state is reached. The R-statistic identifies three rotor speed steady-state time intervals ([0.4s, 2s], [2.4s, 3.5s], and [4.2s, 5.6s]) and three q -axis current steady-state time intervals ([0.7s, 2s], [2.8s, 3.5s], and [4.2s, 5.6s]).

Therefore, the detected steady-state operating conditions of the motor are in the time intervals [0.7s, 2s], [2.8s, 3.5s], and [4.2s, 5.6s].



(a)



(b)

Figure 42. SPMSM steady-states identification: (a) Electrical rotor speed steady-states identification; (b) q -axis current steady-states identification.

Table 28. R-statistic parameters.

Parameters	Value
N_w	2000
R_{crt}	1.4
$\sigma_\omega(k)$	$0.1 \cdot \omega(k)$
$\sigma_{i_q}(k)$	$0.1 \cdot i_q(k)$

Figure 43 shows the results of the q -axis inductance identification in the three detected SPMSM steady-states. The estimation errors are 2.34%, 22.68%,

15.36%. Note that the operating condition in which the highest accuracy has been achieved is the one with the highest value of ωi_q . This can be explained considering the presence of model uncertainties and measurements errors. Let us consider the first equation of the model (66), introducing model uncertainties and measurement errors:

$$\tilde{u}_d + \varepsilon_u = -L_q(\omega + \varepsilon_\omega)(i_q + \varepsilon_i) + \varepsilon_m \quad (98)$$

where ε_u , ε_ω , ε_i and ε_m are the error of the voltage estimation, speed measurement, current measurement, and the model uncertainty, respectively. The model uncertainty takes into account a not perfect steady-state and a not perfect zero d -axis current. Note that these errors are also present in the Simulink model used to generate the data. By reversing (98), the following expression of the estimated q -axis inductance is achieved:

$$L_q = -\frac{\tilde{u}_d}{\omega i_q} - \frac{\varepsilon_u - \varepsilon_m}{\omega i_q} - L_q \left(\frac{\varepsilon_\omega}{\omega} + \frac{\varepsilon_i}{i_q} + \frac{\varepsilon_i \varepsilon_\omega}{\omega i_q} \right) \quad (99)$$

$$L_q = \hat{L}_q - \frac{\varepsilon_u - \varepsilon_m}{\omega i_q} - L_q \left(\frac{\varepsilon_\omega}{\omega} + \frac{\varepsilon_i}{i_q} + \frac{\varepsilon_i \varepsilon_\omega}{\omega i_q} \right) \quad (100)$$

$$\hat{L}_q = L_q + \frac{\varepsilon_u - \varepsilon_m}{\omega i_q} + L_q \left(\frac{\varepsilon_\omega}{\omega} + \frac{\varepsilon_i}{i_q} + \frac{\varepsilon_i \varepsilon_\omega}{\omega i_q} \right) \quad (101)$$

This analysis shows that the estimation errors of the q -axis inductance are minimized when the identification is performed on operating conditions with high values of ω and i_q .

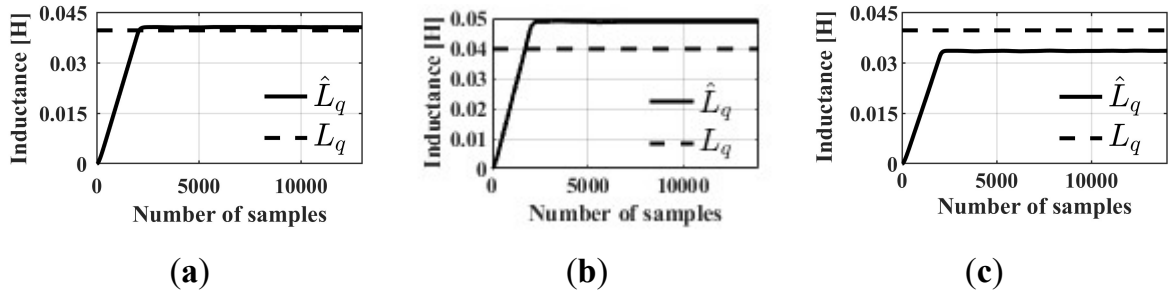


Figure 43. q -axis inductance identification: (a) 6000 rpm – 0.63 A; (b) 12000 rpm – 0.13 A; (c) 1200 rpm – 1.1 A.

In **Figure 44-Figure 46** the results of the rotor flux linkage and stator resistance identification in three different couples of SPMSM steady states are

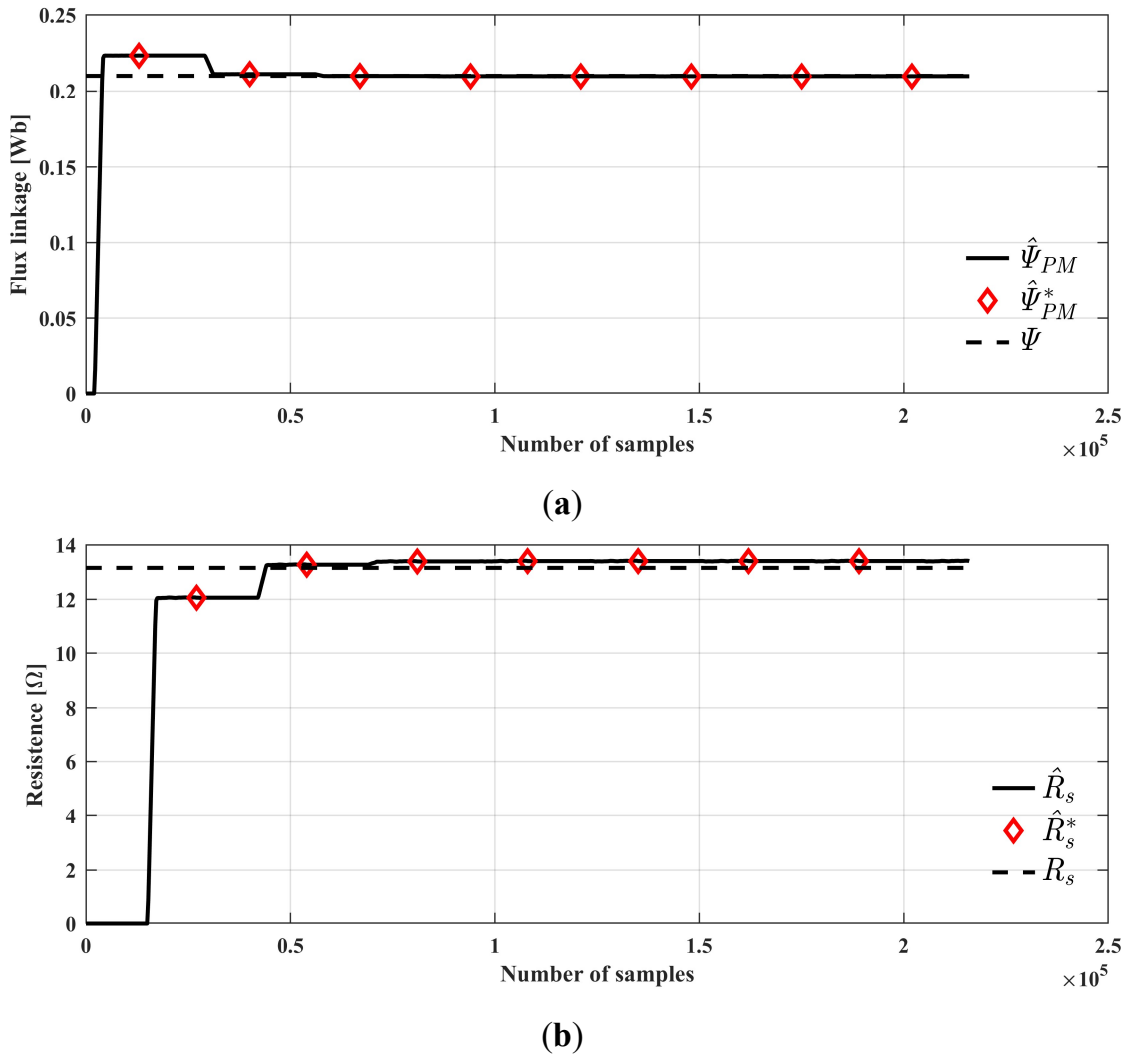
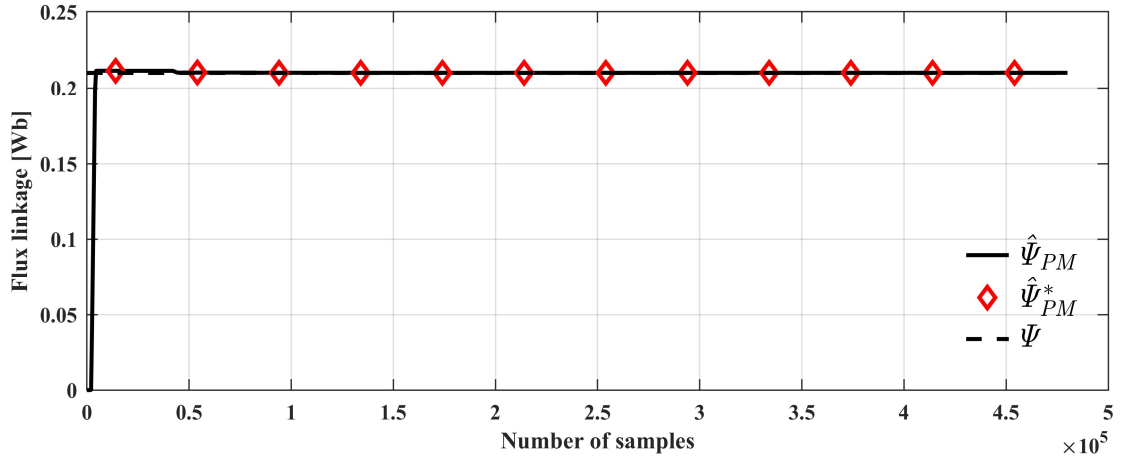
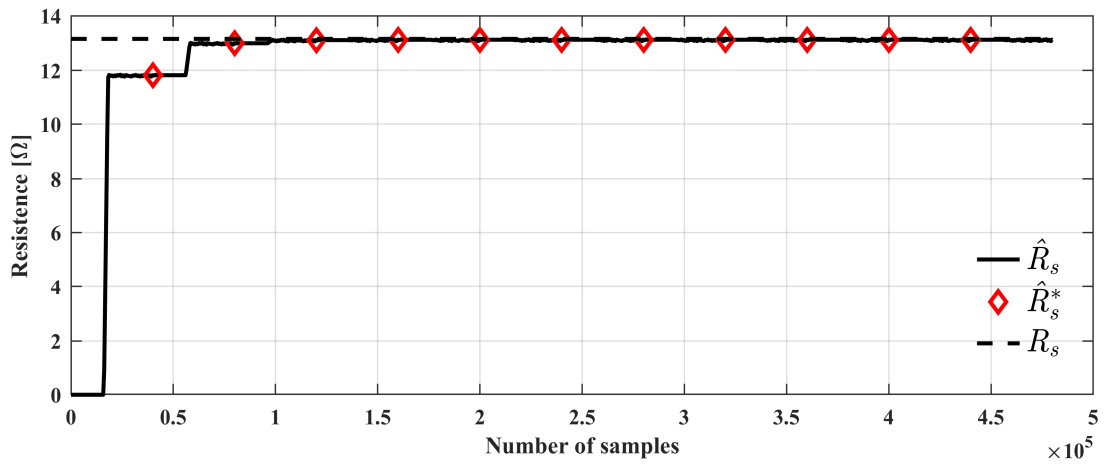


Figure 44. Parameter identification based on the coupled Adaline NNs: (a) Rotor flux linkage identification on SS1: 6000 rpm – 0.63 A; (b) Stator resistance identification on SS2: 1200 rpm – 1.1 A.



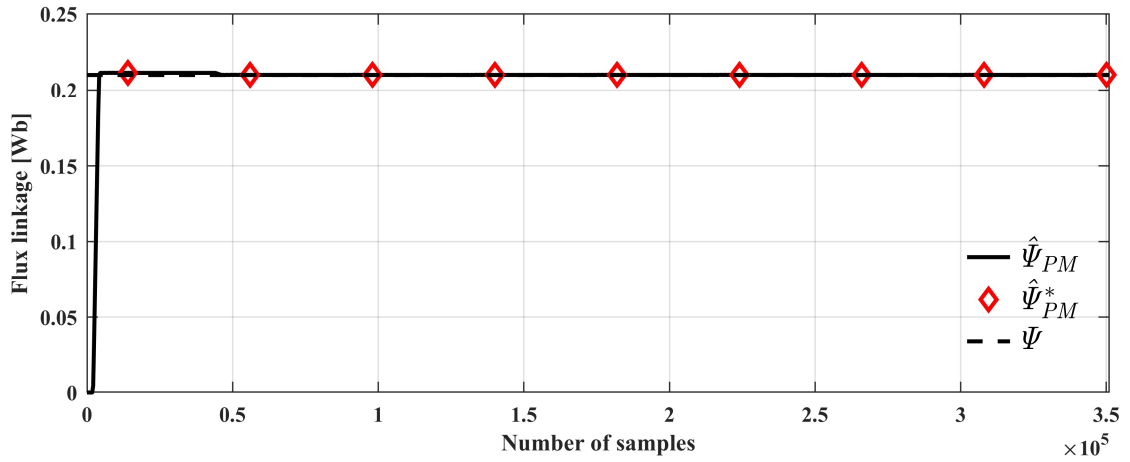
(a)



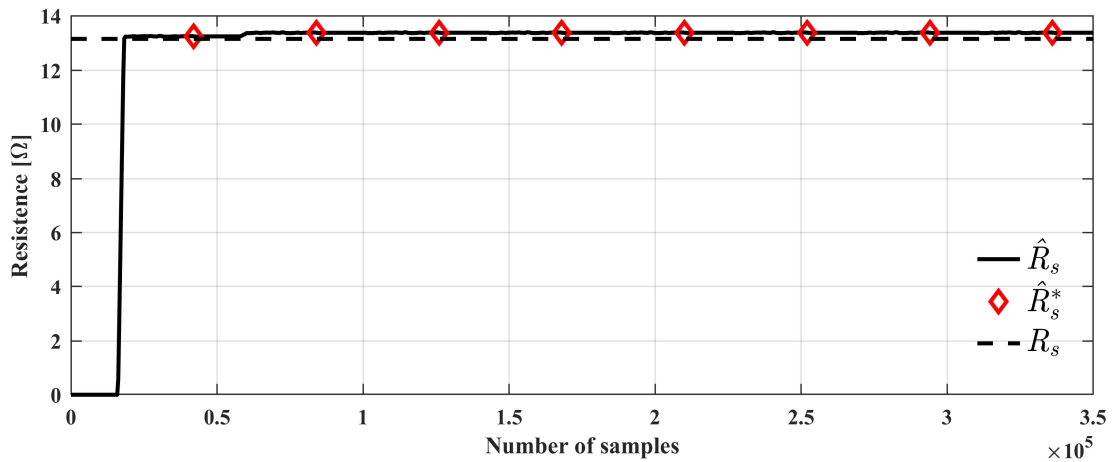
(b)

Figure 45. Parameter identification based on the coupled Adaline NNs: (a) Rotor flux linkage identification on SS1: 12000 rpm – 0.13 A; (b) Stator resistance identification on SS2: 6000 rpm – 0.63 A.

shown. In these three cases, SS1 and SS2 have been chosen to satisfy the convergence condition (93): $|r|$ is equal to 0.11, 0.10 and 0.01, respectively. In this case, since the SPMSM parameters are constant in all the operating conditions, the procedure to select SS1 and SS2 shown in **Figure 37** and **Figure 38** has not been applied. Note that, in all the cases, the provisional estimations $\hat{\psi}_{PM}^*$ and \hat{R}_s^* rapidly converge to stable values, proving the validity of the convergence analysis. Moreover, at the end of the identification procedure described in **Algorithm 1**, the estimation errors of the rotor flux linkage are 0.095%, 0.032%, and 0.020%, respectively; instead, the estimation errors of the stator resistance are 1.90%, 0.24%, and 1.70%, respectively.



(a)



(b)

Figure 46. Parameter identification based on the coupled Adaline NNs: (a) Rotor flux linkage identification on SS1: 12000 rpm – 0.13 A; (b) Stator resistance identification on SS2: 1200 rpm – 1.1 A.

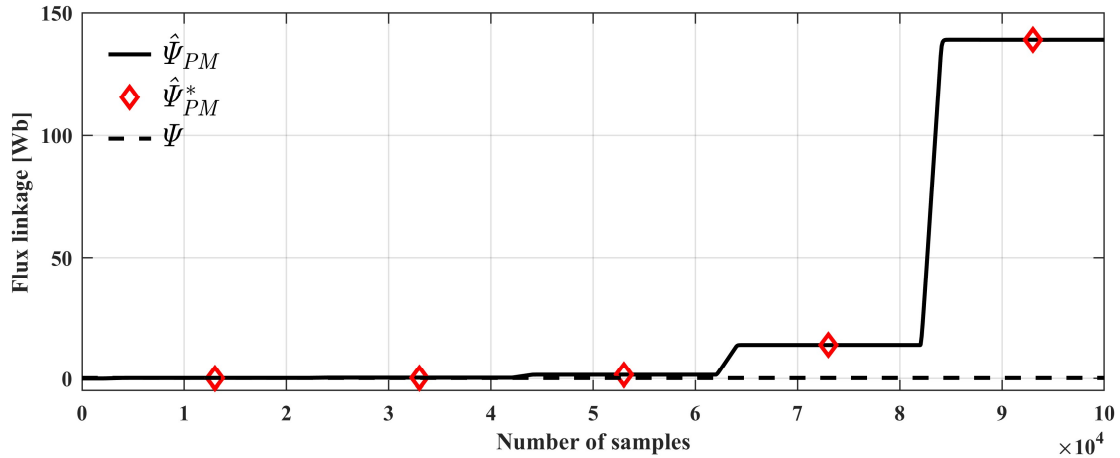
Instead, **Figure 47** shows the results of the rotor flux linkage and stator resistance identification with SS1 and SS2 chosen in disagreement with the convergence condition (93) ($|r| = 9.7$). In this case the provisional estimations are divergent, as expected by the theoretical study.

The simulation results clearly show the effectiveness and the validity of the proposed approach. In particular, the main achievements can be summarized as follows:

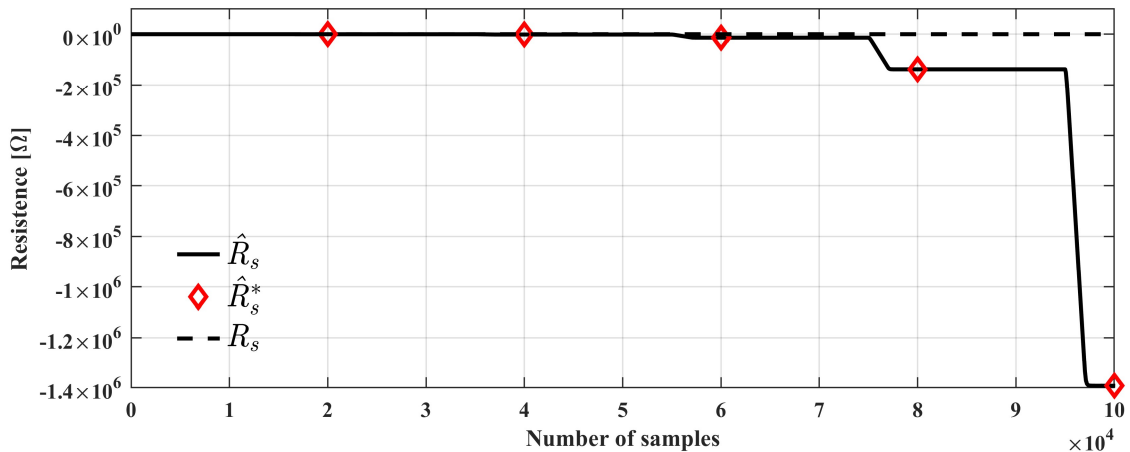
- the proposed compensation of the actuation delay is very effective;

- the convergence analysis of the proposed identification method based on the coupled Adaline NN has been validated.

The proposed method can overcome the rank deficiency issue providing very accurate estimations.



(a)



(b)

Figure 47. Parameter identification based on the coupled Adaline NNs: (a) Rotor flux linkage identification on SS1: 6000 rpm – 0.63 A; (b) Stator resistance identification on SS2: 12000 rpm – 0.13 A.

4.5. Experimental Results

In this section, the results of the parameter identification of a real high-speed SPMSM drive with zero d -axis current control are reported. A photo of the experimental setup is shown in **Figure 48**. The values of the parameters of the

motor are reported in **Table 29** while the available stationary operating condition (OC) of the motor are shown in **Table 30**.



Figure 48. Experimental test bench.

Table 29. SPMSM parameters.

Parameters	Value
Rated Power	8.5 kW
Maximum Speed	120 krpm
n_p	2
R_s	0.698 Ω
L_q	1.251 mH
ψ_{PM}	26.82 mWb
Switching frequency	40 kHz
T_s	$2.5 \cdot 10^{-5}$ s

Note that the value of the stator resistance is the direct current (DC) value at room temperature; the rotor flux linkage has been measured in no-load condition

at the room temperature and the stator inductance has been measured at low DC. The measured temperature of the SPMSM in the available OCs is reported in **Table 31**.

Table 30. SPMSM stationary operating conditions.

		i_q [A]			
		-3.5	-7	-10.5	-14
ω_m [rpm]	6000	OC 1.1	OC 1.2	OC 1.3	OC 1.4
	12000	OC 2.1	OC 2.2	OC 2.3	OC 2.4
	18000	OC 3.1	OC 3.2	OC 3.3	OC 3.4
	24000	OC 4.1	OC 4.2	OC 4.3	OC 4.4
	30000	OC 5.1	OC 5.2	OC 5.3	OC 5.4

Table 31. Temperature of the SPMSM.

		i_q [A]			
		-3.5	-7	-10.5	-14
ω_m [rpm]	6000	33 °C	46 °C	70 °C	112 °C
	12000	36 °C	49 °C	73 °C	114 °C
	18000	39 °C	52 °C	75 °C	115 °C
	24000	39 °C	51 °C	74 °C	113 °C
	30000	43 °C	55 °C	78 °C	119 °C

The voltage references and the compensated voltages in the OC 5.1 are reported in **Figure 49**. Since this is an OC with a high value of the speed, a significant difference between the two voltages is expected. In fact, a difference of about 35 and 11 V between the voltage references and compensated voltages of the d - and q -axis can be observed, respectively. In this case, the difference between u_q^* and \tilde{u}_q is negligible due to the low value of u_d^* . Moreover, note that the d -axis voltage reference is negative, which is obviously incorrect, since from (63), considering the sign of the q -axis current, a positive value is expected. Instead, the compensated d -axis voltage is positive. This result clearly shows the need to compensate the voltage references. **Figure 50** shows the voltage

references and the compensated voltages in the OC 1.4. Since, compared to the previous case, a lower speed is considered, a minor difference between the two voltages is expected. In fact, a difference of about 0.5 V and 1 V between the voltage references and compensated voltages of the d - and q -axis is obtained, respectively. Finally, **Figure 51** shows the voltage references and the compensated voltages in the OC 5.4. In this case, a difference of about 33 V and 20 V between the voltage references and compensated voltages of the d - and q -axis is obtained, respectively.

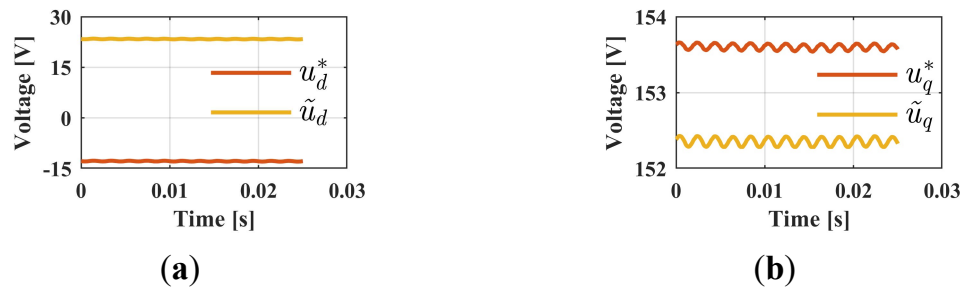


Figure 49. SPMSM voltages in the OC 5.1: (a) d -axis voltages; (b) q -axis voltages.

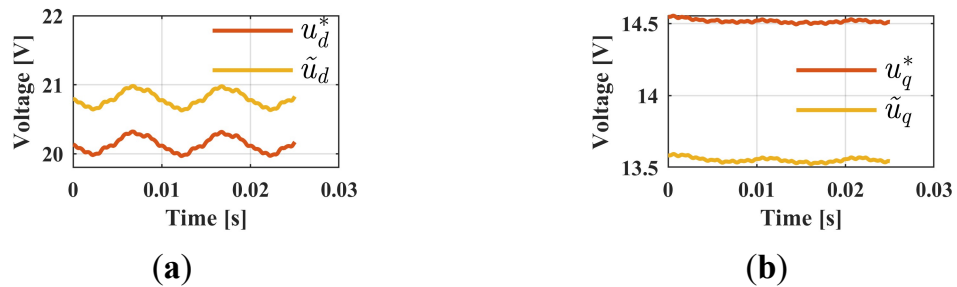


Figure 50. SPMSM voltages in the OC 1.4: (a) d -axis voltages; (b) q -axis voltages.

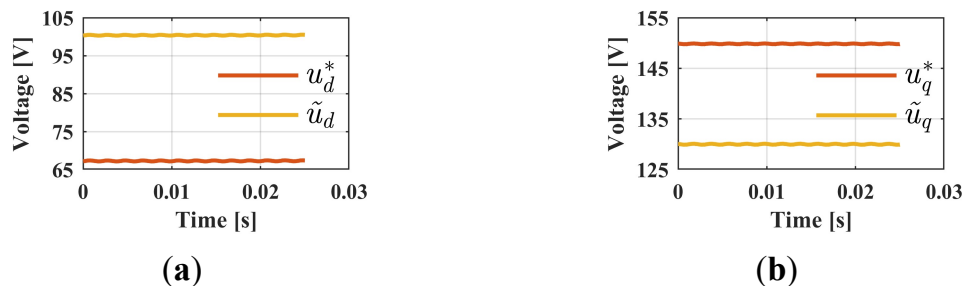


Figure 51. SPMSM voltages in the OC 5.4: (a) d -axis voltages; (b) q -axis voltages.

In **Figure 52**, the results of the q -axis inductance identification in all the available OCs are reported. Note that, despite the wide ranges of the current and speed, low variations of the estimations are obtained. This result confirms the

validity of the voltages compensation with the proposed approach. Note that, the estimated q -axis inductance slightly decreases with increasing speed. This is confirmed by [144]. For speed values between 6 and 18 krpm, the estimated q -axis inductance decreases when the current increases. The phenomenon is in accordance with the saturation effect. Instead, for speed values higher than 18 krpm, estimated q -axis inductance increases when the current increases. This unexpected behavior can be explained by the presence of neglected phenomena in the high frequency operations. To compare the results with the measured of value of L_q , a curve at 0 krpm has been extrapolated using 2nd degree polynomials. The estimation error between the value extrapolated at 0 A/0 krpm and the measured value is 1.8%. Therefore, a good accuracy of the q -axis inductance identification has been achieved.

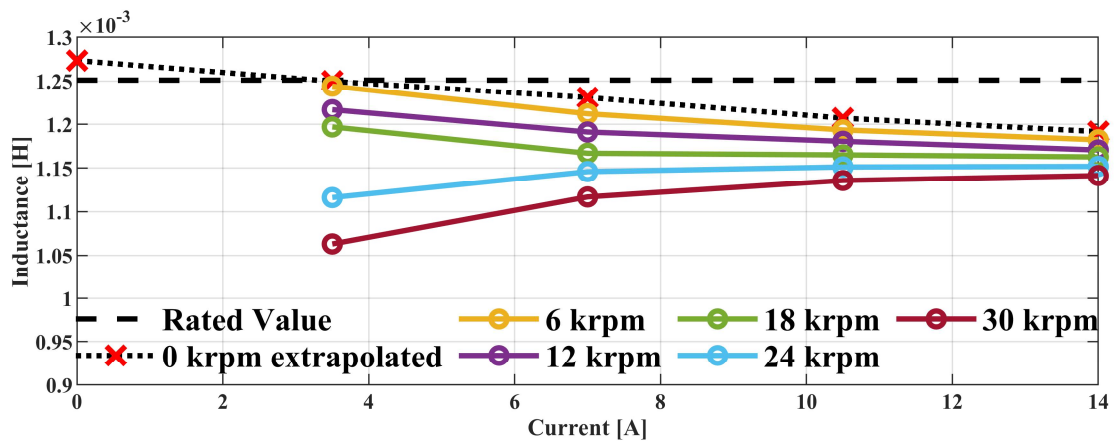


Figure 52. q -axis inductance identification.

The first identification of ψ_{PM} and R_s performed before the implementation of the procedures shown in **Figure 37** and **Figure 38** provides $\hat{\psi}_{PM}^*(end) = 23.69$ mWb and $\hat{R}_s^*(end) = 1.166$ Ω (SS1 = OC 5.1 and SS2 = OC 1.4). the presence of a dominant parameter can now be detected using these values.

Figure 53 shows the results of the rotor flux linkage identification performed following the procedure of **Figure 37** for the choice of SS2. The OC 1.4 is the only one in which the identification of ψ_{PM} cannot be performed. In fact, in this

case, there is no other OC that can be chosen as SS2 to satisfy the converge condition (93). Note that, except for the results at 6 krpm, the rotor flux linkage slightly decreases with increasing speed and current. These results are in accordance with the temperatures reported in **Table 31**. Instead, the results a 6 krpm are not reliable and can be explained analyzing the estimation errors. For example, when the estimation at SS1=OC 1.3 is performed, SS2=OC 1.4 is chosen according to **Figure 37**. In this case, the ratio $\frac{r}{1-r}$, that appears in (96), is equal to 3. Thus, in this condition, the error $(\psi_{PM1} - \psi_{PM2})$, which is a positive quantity, is amplified and an overestimation is obtained. To compare the results with the measured of value of ψ_{PM} , a curve at 0 krpm has been extrapolated using 1st degree polynomials (the results at 6 krpm have not been considered for this operation). The estimation error between the value extrapolated at 0 A/0 krpm and the measured value is 3.36%.

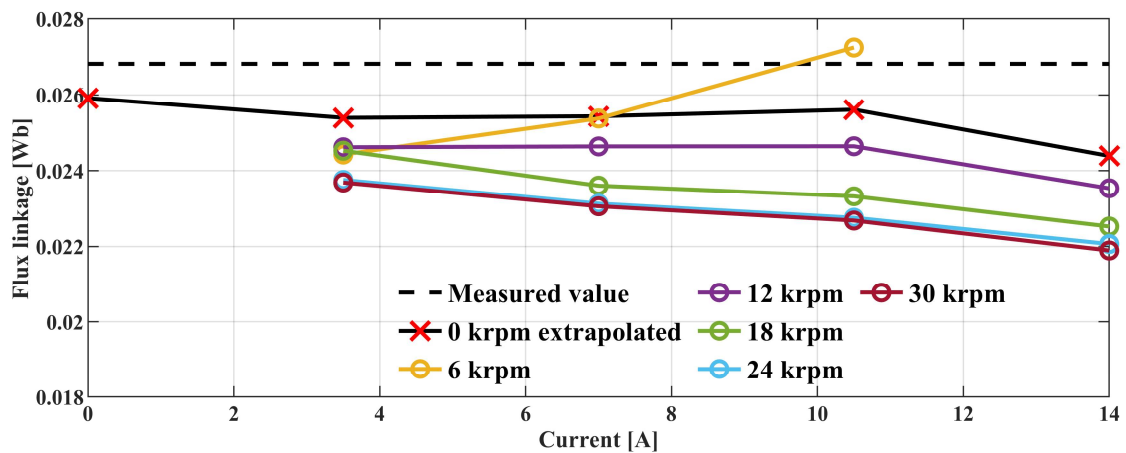


Figure 53. Rotor flux linkage identification in agreement with the optimal criterion.

Figure 54 shows the results of the stator resistance identification performed following the procedure of **Figure 38** for the choice of SS1. In this case, the OC 5.1 is the only one in which the identification of R_s cannot be performed. With few exceptions, an increase of the estimated resistance with the speed and current can be observed. Large estimation errors are achieved in the OC 2.1, OC 3.1, and OC 4.1 (SS1 = OC 5.1). Also in this case, these errors can be explained by

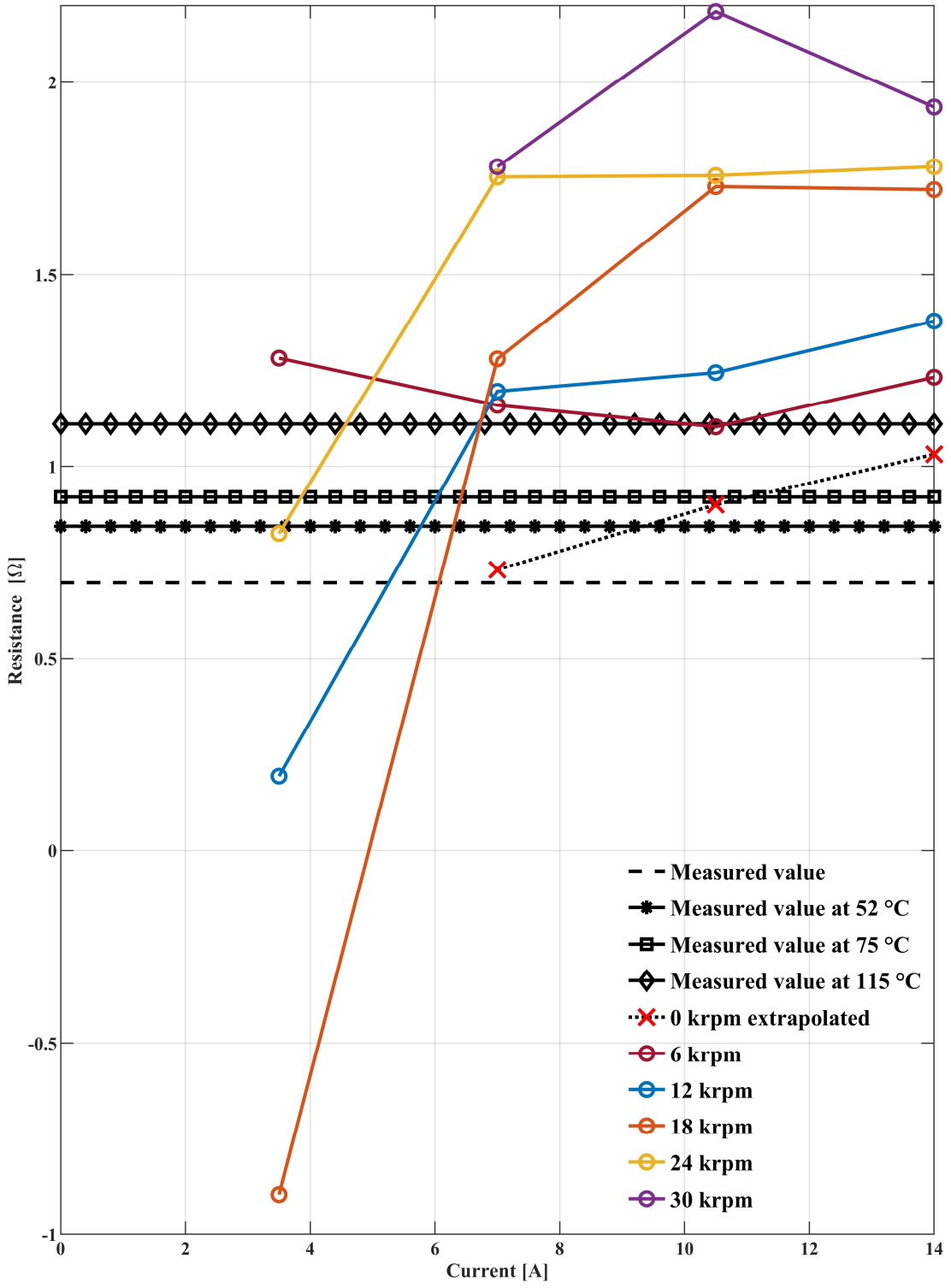


Figure 54. Stator resistance identification in agreement with the optimal criterion.

analyzing (97). In fact, the ratio $\frac{r}{1-r}$ is equal to 0.67, 1.5 and 4, respectively. The error $(R_{s2} - R_{s1})$, which is a negative quantity, is amplified and the stator resistance is underestimated. To compare the results with the measured value of R_s , a curve at 0 krpm has been extrapolated using 1st degree polynomials (the

results at 3.5 A have not been considered for this operation). In particular, the extrapolated values are compared with the measured DC values of the resistance at different temperatures. According to **Table 31**, the extrapolated values at 7, 10.5 and 14 A have been compared with measured DC values of the resistance at 52, 75 and 115 °C, respectively. The estimation errors are 13.36%, 2.18%, and 7.08%.

Finally, in **Figure 55** and **Figure 56**, the results of the identification ψ_{PM} and R_s in disagreement with the procedures reported in **Figure 37** and **Figure 38** have been reported. For the identification of ψ_{PM} , the criteria of maximising $|r|$ and minimizing $||\omega_1| - |\omega_2||$ have been followed. Instead, for the identification of R_s , the criteria of maximising $|r|$ and minimizing $||i_{q1}| - |i_{q2}||$ have been followed. The results clearly show that not reliable estimations are achieved, with larger estimation errors compared to the results reported in **Figure 53** and **Figure 54**. This further demonstrates the effectiveness of the proposed criteria for the choice of the steady-states.

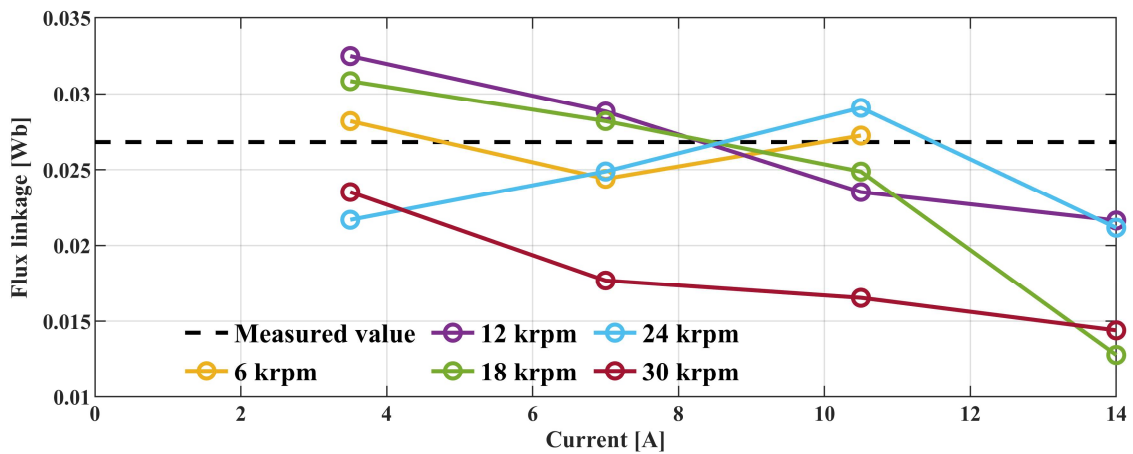


Figure 55. Rotor flux linkage identification in disagreement with the optimal criterion.

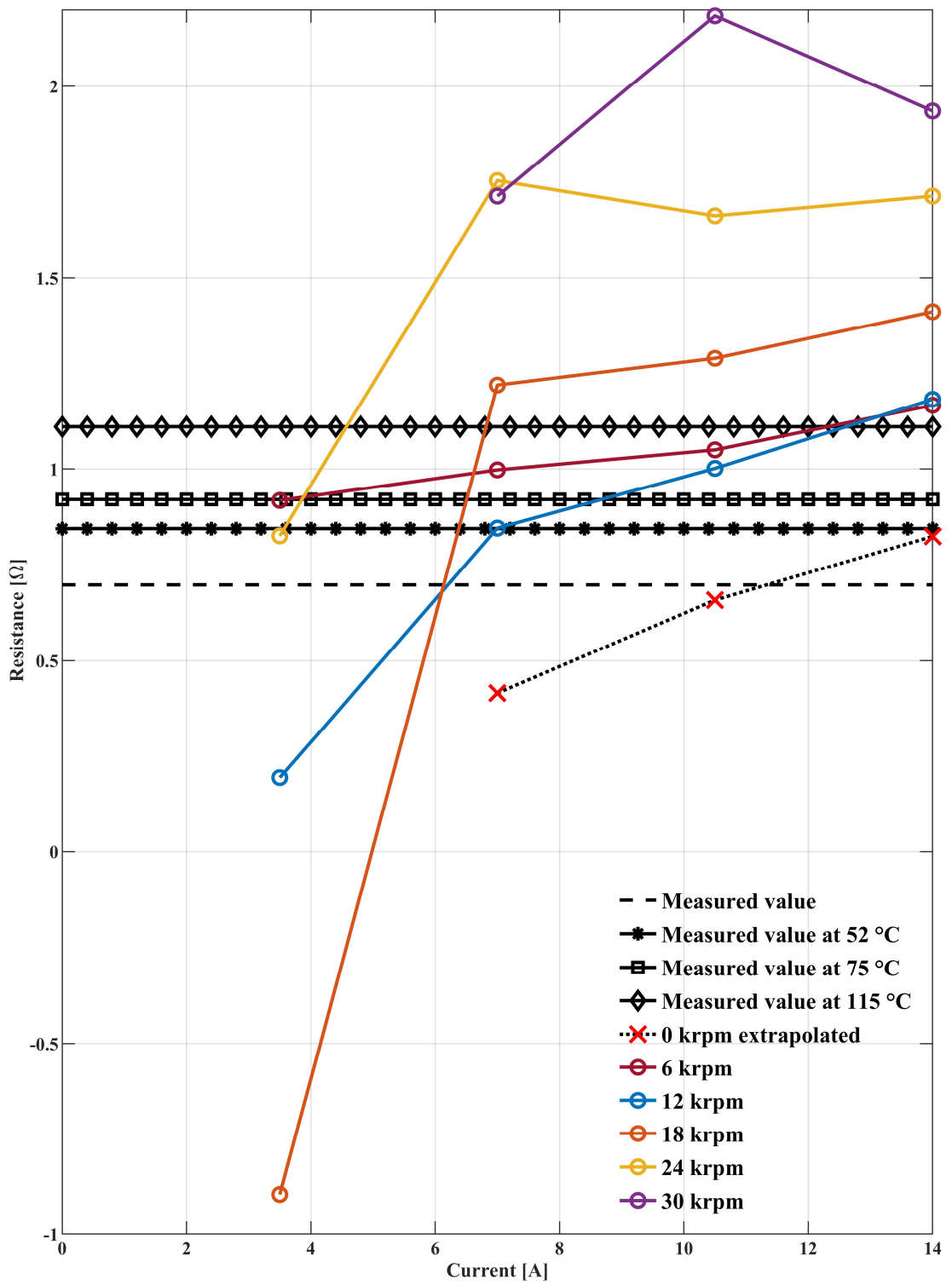


Figure 56. Stator resistance identification in disagreement with the optimal criterion.

4.6. Final Considerations

A novel method to perform an automated offline parameter identification of SPMSMs has been presented. Compared to the existing methods, the proposed one allows to identify the electrical parameters of the machine without ad hoc tests or perturbations of the operating conditions. The lack of voltage measurements has been overcome by using an original model which corrects the voltage references by means of the compensation of the actuation delay caused by the digital control and PWM inverter. Instead, to overcome the rank deficiency issue, an innovative strategy based on two coupled Adaline NNs has been designed. A detailed theoretical study has been performed to analyze the convergence of the proposed algorithm and the estimation errors. In particular, two optimal procedures have been developed to choose the SPMSM steady states to be used to feed the Adaline NNs.

Simulation and experimental results have been provided to evaluate the performances of the proposed method. The simulation tests have been performed by feeding the Adaline NNs with data obtained with a Simulink model of an SPMSM drive. Measurement errors have been introduced while no parameter variations have been simulated. The results show that the developed SPMSM model to compensate the actuation delay is very accurate. Instead, the presence of measurement errors slightly affects the accuracy of the q -axis inductance estimation, especially when the identification is performed in SPMSM operating condition with a low value of $\omega \cdot i_q$. Finally, the algorithm based on the two coupled Adaline NNs ensures outstanding performances with high accuracy of the estimations of ψ_{PM} and R_s .

The experimental results have been obtained by feeding the Adaline NNs with data provided by a custom high-speed SPMSM drive. These results underline the importance of the compensation of the actuation delay and the

comparison of the estimations with the measured values of the parameters shows a good accuracy of the results. Moreover, the analysis of the estimation errors further confirms the validity of the presented theoretical study and stresses the importance of a proper selection of the SPMSM steady states used to feed the Adaline NNs.

4.7. Publications

Part of the contents and results presented in this chapter have been published in [138], [145], and [146].

5. Conclusions and Future Developments

In this thesis, advancements in control, design, and parameter identification of permanent magnet synchronous machines have been presented. In particular novel challenges and opportunities offered by recent applications and technologies have been considered.

The problem of the control of a permanent magnet synchronous generator in a novel direct drive application is addressed in the chapter 2. In particular, a PMSG fully embedded within a small-scale variable speed DHAWT with a fixed pitch has been considered. The problem considered is the extension of the power generation capability of the DHAWT over a wide wind speed range, ensuring the respect of the safety mechanical limits of the system. An original control scheme has been designed, using a LO for the aerodynamic torque estimation and a Shallow NN for the wind speed estimation. Experimental tests have performed to assess the performances of the proposed solution. The main limits of the proposed control scheme are the complexity, the need for a shaft speed transducer and the training phase required by the wind speed estimator. An innovative sensorless control scheme which avoids the use of a wind speed estimator has been already designed by the author. The future goal is the validation with simulations and experiments.

The problem of the minimization of the cogging torque of novel modular PMSMs is treated in the chapter 3. Two innovative design methods based on the optimization of the shape of the stator tooth tips have been proposed. In both cases, the optimization problem has been partially solved by means of analytical studies. Moreover, to completely solve the problem, a heuristic approach based on the use of multilayer ANN-based surrogate models has been adopted. Simulations with the FEA considering manufacturing uncertainties have been carried out to validate the proposed methods.

Finally, the problem of the parameter identification of SPMSMs using data obtained without ad hoc tests or control actions is tackled in the chapter 4. An original algorithm based on the three Adaline NNs has been proposed. Two of those have been designed to solve the rank deficiency issue while a SPMSM model considering the actuation delay of the voltage references has been adopted to overcome the lack of voltage measurements. Simulation and experimental tests have been performed to assess the performances of the proposed solution. In the future, the method will be extended to interior PMSMs and the effect of the down sampling (a typical issue in cloud computing environments) of the measurement data on the accuracy of the parameter identification will be studied.

A. Nomenclature

Symbols

*	Apex for the variables references
^	Apex for the estimated variables
A_r	Wind turbine rotor swept area
B	Airgap flux density
C_p	Power coefficient
C_{pmax}	Maximum value of the power coefficient
<i>Depth</i>	Depth of the sub-teeth layer
d_{MAX}	Depth limit for the sub-teeth layer
F_m	Rotor magneto-motive force
f_{IHci}	Frequency of the introduced harmonic components
f_{sp_k}	Spatial frequency of the k -th sinusoidal profile
g	Airgap length (Outer radius of the rotor to the tooth tips)
g'	Actual airgap length taken into account the presence of stator slots and the shape of the tooth tips
i_d	d -axis current
i_q	q -axis current
J	Total moment of inertia
K_T	Torque constant
L_d	d -axis stator inductance
L_q	q -axis stator inductance
l_{ss}	Additional airgap flux-path due to the presence of stator slots
L_{stk}	Stack length
l_{tts}	Additional airgap flux-path due to the tooth tips shape
m	Number of stator core segments
N_{HL}	Number of hidden layers
N_{HN}	Number of hidden neurons
N_i	Number of independent tooth tips
N_{MAX}	Maximum number of sample data

n_p	Number of pole pairs
N_s	Number of stator slots
N_{sample}	Number of sample data used for the ANNs training
N_{sp}	Number of the introduced sinusoidal profiles
N_{start}	Number of sample data randomly generated
N_{step}	Number of steps of the transient-with-motion finite element analysis
N_{sub}	Number of sub-teeth
N_w	Length of the windows of the R-statistic method
P_{rated}	Rated power of the wind turbine
P_w	Wind power
R	Wind turbine blade tip radius
R_{crt}	R-statistic critical value
R_1	Outer radius of the PMSM rotor
R_2	Inner radius of the PMSM stator
R_s	Stator resistance
\hat{R}_s^*	Stator resistance provisional estimation
R_χ	R-statistic index for the generic variable χ
T	Electromagnetic torque
T_a	Aerodynamic torque
T_{AHC}	Additional harmonic components of the cogging torque
T_{av}	Dynamic friction loss torque
T_{cog}	Cogging torque
T_{cog_ANN}	Cogging torque computed by means of the artificial neural networks
T_{cog_FEA}	Cogging torque computed by means of the finite element analysis
T_l	Load torque
T_{IHC}	Introduced harmonic components of the cogging torque
T_{max}	Maximum aerodynamical torque of the wind turbine
T_{NHC}	Native harmonic components of the cogging torque
T_s	Sampling period
u_d	d -axis voltage
\tilde{u}_d	Compensated d -axis voltage

u_q	q -axis voltage
\tilde{u}_q	Compensated q -axis voltage
v	Unconstrained wind speed
v_{DC}	DC-link voltage
W	Stored magnetic energy
w_χ	Box-Muller noise added to the generic variable χ
\mathbf{x}	Vector of the design variables
\mathbf{x}_{opt}	Solution achieved by the optimization
α	Angular displacement along stator circumference
Θ	Temperature of the machine
θ	Electrical rotor position
θ_m	Mechanical rotor position
Λ	Airgap permeance function
Λ_{ss}	Airgap permeance function component associated to the stator slotting effect
Λ_{tts}	Airgap permeance function component associated to the modified shape of the tooth tips
λ	Tip-speed ration
λ_{max}	Optimal value of the tip-speed ratio
ρ	Air density
σ_χ	Standard deviation of the Box-Muller noise
χ_n	Generic variable with the addition of the Box-Muller noise
ψ_{PM}	Rotor flux linkage
$\hat{\psi}_{PM}^*$	Rotor flux linkage provisional estimation
ω	Electrical mechanical speed
ω_m	Rotor mechanical speed
ω_{rated}	Rated speed of the wind turbine

Acronyms

AdNN	Adaline neural network
AHC	Additional harmonic component
ANN	Artificial neural network
APMSG	Annular permanent magnet synchronous generator
APMSM	Annular permanent magnet synchronous machine
ATO	Aerodynamic torque observer
CFD	Computational fluid dynamics
CPC	Constant power control
CSC	Constant speed control
CTC	Constant torque control
DHAWT	Ducted horizontal axis wind turbine
FEA	Finite element analysis
FF	Feed forward
FOC	Field-oriented control
FPPF	Flux-path permeance function
GA	Genetic algorithm
GSC	Grid side converter
IHC	Introduced harmonic components
IPMSM	Interior permanent magnet synchronous machine
LCM	Least common multiple
LM	Levenberg–Marquardt
LO	Luenberger observer
LUT	Look-up table
MGN	Maximum generations number
MMF	Magneto-motive force
MPPT	Maximum power point tracking
MSC	Machine side converter
NHC	Native harmonic components
NN	Neural network

OC	Operating condition
PI	Proportional-integral
PID	Proportional-integral-derivative
PM	Permanent magnet
PMM	Permanent magnet machine
PMSG	Permanent magnet synchronous generator
PMSM	Permanent magnet synchronous machine
PS	Population size
PSF	Power signal feedback
PWM	Pulse width modulation
SPMSM	Surface permanent magnet synchronous machine
SSC	Segmented stator core
SynRM	Synchronous reluctance motor
TO	Topological optimization
TWM	Transient-with-motion
UUM	Uniform uncertainties method
VSC	Variable structure controller
VSFP	Variable-speed and fixed-pitch
WECS	Wind energy conversion system
WSE	Wind speed estimator

B. Mathematical Model of the PMSM

The mathematical model of the PMSM in the dq reference system is described by the following equations:

$$u_d = R_s i_d + L_d \frac{di_d}{dt} - n_p \omega_m L_q i_q \quad (\text{B.1})$$

$$u_q = R_s i_q + L_q \frac{di_q}{dt} + n_p \omega_m L_d i_d + n_p \omega_m \psi_{PM} \quad (\text{B.2})$$

These equations state a relationship between the dq -axis voltages (u_d, u_q), the dq -axis currents (i_d, i_q), and the mechanical rotor speed (ω_m). The parameters are the phase resistance R_s , dq -axis stator inductances L_d and L_q , rotor flux linkage ψ_{PM} , and number of pole pairs n_p . The dq -axis stator inductances of a SPMSM, which is the PMSM topology considered in this work, can be regarded as equal.

The electrical rotor speed ω and position θ can be defined as

$$\omega = n_p \omega_m \quad (\text{B.3})$$

$$\theta = n_p \theta_m \quad (\text{B.4})$$

In which θ_m is the mechanical rotor position.

The electromagnetic torque of a SPMSM, depends on the q -axis current, number of pole pairs, and rotor flux linkage:

$$T = \frac{3}{2} n_p \psi_{PM} i_q = K_T i_q \quad (\text{B.5})$$

where K_T is the torque constant.

The considered model is completed by a last equation, which expresses the rotational mass equilibrium:

$$T - T_l - T_{av} = J \frac{d\omega_m}{dt} \quad (\text{B.6})$$

where T_l is the load torque and T_{av} represents the dynamic friction loss torque.

C. Wind Speed Estimator

In this appendix, a study to support the design of the WSE is reported. In particular, this study demonstrates that there is no function such that $v = f(\hat{T}_a, \omega_m)$. Moreover, the study proves that there is a function such that $v = f_v(\hat{T}_a, \omega_m, i_q)$. This result allows to properly design the WSE based on the Shallow NN, ensuring a good accuracy of the wind speed estimations, while reducing the computational requirements.

Considering the parameter uncertainties relative to J and K_T , (18) can be rewritten as

$$\hat{B} = B + \Delta B \quad (\text{C.1})$$

Therefore, the differential error expressed by (20) can now be expressed as

$$\dot{\mathbf{e}} = A\mathbf{e} - LC\mathbf{e} + \Delta B\mathbf{u} = (A - LC)\mathbf{e} + \Delta B\mathbf{u} \quad (\text{C.2})$$

The solution of this first-order differential equation can be expressed by the sum of a component asymptotically convergent to zero ($\mathbf{e}_1(t)$) and a component that depends on \mathbf{u} ($\mathbf{e}_2(\mathbf{u})$):

$$\mathbf{e} = \mathbf{e}_1(t) + \mathbf{e}_2(\mathbf{u}) = \mathbf{e}_1(t) + \mathbf{e}_2(i_q) \quad (\text{C.3})$$

Neglecting the dynamic of the error of the LO, i.e., $\mathbf{e}_1(t) = 0$, the following equation is established:

$$\hat{T}_a = J \frac{d\omega_m}{dt} + K_T K_T i_q + \mathbf{e}_2(i_q) \quad (\text{C.4})$$

This equation is based on the model of the system observed by the LO and on the estimation error due to parameter uncertainties.

Theorem 1. There is no function f_v such that $v = f_v(\hat{T}_a, \omega_m)$.

Proof of Theorem 1.

Let us assume that, during the test of the WECS with the anemometer, the following values of the measured wind and shaft speed, q -axis current, and estimated aerodynamic torque are registered in two different time instants t_1 and t_2 :

$$\begin{aligned} & (\omega_{m1}, v_1, i_{q1}, \hat{T}_{a1}) \\ & (\omega_{m2}, v_2, i_{q2}, \hat{T}_{a2}) \end{aligned} \tag{C.5}$$

Moreover, let us assume that:

$$\omega_{m1} = \omega_{m2} = \omega_{m12}$$

$$v_1 \neq v_2$$

$$i_{q1} \neq i_{q2}$$

Figure 7 (b) shows that, in this case, the actual aerodynamic torque values in t_1 and t_2 instants are different:

$$T_{a1}(\omega_{m12}, v_1) \neq T_{a2}(\omega_{m12}, v_2) \tag{C.6}$$

However, because of the presence of the estimation error $e_2(i_q)$, the following can be verified:

$$\hat{T}_{a1} = \hat{T}_{a2} = \hat{T}_{a12} \quad (\text{C.7})$$

In fact, in t_1 and t_2 , (C.7) is satisfied:

$$J \left. \frac{d\omega_m}{dt} \right|_{t_1} = T_{a1} - K_T K_T i_{q1} - T_{av}(\omega_{m1}) \quad (\text{C.8})$$

$$J \left. \frac{d\omega_m}{dt} \right|_{t_2} = T_{a2} - K_T K_T i_{q2} - T_{av}(\omega_{m1}) \quad (\text{C.9})$$

Moreover, from (C.4), (C.8) and (C.9) results:

$$\begin{aligned} \hat{T}_{a1} = J \left. \frac{d\omega_m}{dt} \right|_{t_1} + K_T K_T i_{sq1} + e_2(i_{q1}) &= T_{a1} - T_{av}(\omega_{m12}) + \\ &e_2(i_{q1}) \end{aligned} \quad (\text{C.10})$$

$$\begin{aligned} \hat{T}_{a2} &= J \left. \frac{d\omega_m}{dt} \right|_{t_2} + K_T K_T i_{sq2} + e_2(i_{q2}) \\ &= T_{a2} - T_{av}(\omega_{m12}) + e_2(i_{q2}) \end{aligned} \quad (\text{C.11})$$

Therefore, $\hat{T}_{a1} = \hat{T}_{a2}$ if and only if

$$T_{a1} + e_2(i_{q1}) = T_{a2} + e_2(i_{q2}) \quad (\text{C.12})$$

Different combinations of T_{a1} , T_{a2} , i_{q1} and i_{q2} that satisfy (C.12) may exist.

Therefore, two time instants may exist such that:

$$\omega_{m1} = \omega_{m2}$$

$$\hat{T}_{a1} = \hat{T}_{a2}$$

$$v_1 \neq v_2$$

Thus, there is no function f_v such that $v = f_v(\hat{T}_a, \omega_m)$.

This result suggests that setting \hat{T}_a and ω_m as inputs of the WSE is not a good choice. To ensure the accuracy of the WSE, a possible choice is to set as inputs all the available variables, i.e.

$$v = f_v(u_d, u_q, \hat{T}_a, \omega_m, i_q) \quad (\text{C.13})$$

However, the following theorem demonstrates that the choice of \hat{T}_a , ω_m , and i_q as inputs ensures a correct design of the WSE, reducing the computational requirements compared to the solution expressed by (C.13).

Theorem 2. There is a function f_v such that $v = f_v(\hat{T}_a, \omega_m, i_q)$.

Proof of Theorem 2.

Let us consider two time instants, as in (C.5), and assume that:

$$\omega_{m1} = \omega_{m2} = \omega_{m12}$$

$$i_{q1} = i_{q2} = i_{q12} \quad (\text{C.14})$$

$$v_1 \neq v_2$$

By repeating the previous procedure, it can be stated that $\hat{T}_{a1} = \hat{T}_{a2}$ is verified if and only if

$$T_{a1} + e_2(i_{q12}) = T_{a2} + e_2(i_{q12}) \Rightarrow T_{a1} = T_{a2} \quad (\text{C.15})$$

However, (C.15) cannot be satisfied since $T_{a1} \neq T_{a2}$ from (C.7). Thus, two operating conditions in which

$$\begin{aligned} \omega_{m1} &= \omega_{m2} \\ i_{q1} &= i_{q2} \\ \hat{T}_{a1} &= \hat{T}_{a2} \\ v_1 &\neq v_2 \end{aligned} \quad (\text{C.16})$$

cannot exist. Therefore, there exists a function f_v such that $v = f_v(\hat{T}_a, \omega_m, i_q)$

References

- [1] Commission Staff Working Document Impact Assessment Accompanying the Document Commission Regulation (EU) 2019/1781 Laying Down Ecodesign Requirements for Electric Motors and Variable Speed Drives Pursuant to Directive 2009/125/EC of the European Parliament and of the Council and Repealing Commission Regulation (EC) No 640/2009. SWD/2019/0343 Final. Available online: <https://ec.europa.eu/transparency/regdoc/rep/10102/2019/EN/SWD-2019-343-F1-EN-MAIN-PART-1.PDF> (accessed on 20 January 2022).
- [2] Induction Motor Market: Global Industry Trends, Share, Size, Growth, Opportunity and Forecast 2021-2026. Available online: <https://www.imarcgroup.com/induction-motor-market> (accessed on 23 January 2022).
- [3] Global Permanent Magnet Synchronous Motor (PMSM) Market 2021 by Manufacturers, Regions, Type and Application, Forecast to 2026. Available online: <https://www.globalinfresearch.com/reports/525819/permanent-magnet-synchronous-motor-pmsm> (accessed on 23 January 2022).
- [4] Trends and developments in electric vehicle markets. Available online: <https://www.iea.org/reports/global-ev-outlook-2021/trends-and-developments-in-electric-vehicle-markets> (accessed on 23 January 2022).
- [5] Electric Motors for Electric Vehicles 2022-2032. Available online: <https://www.idtechex.com/en/research-report/electric-motors-for-electric-vehicles-2022-2032/842> (accessed on January 23 2022).
- [6] PERMANENT MAGNET MOTOR MARKET - GROWTH, TRENDS, COVID-19 IMPACT, AND FORECASTS (2022 - 2027). Available online: <https://www.mordorintelligence.com/industry-reports/permanent-magnet-motor-market> (accessed on January 23 2022).
- [7] James Edmondson, "Will Rare-Earths be Eliminated in Electric Vehicle Motors?" Nov. 2020, available online: <https://www.idtechex.com/en/research-article/will-rare-earths-be-eliminated-in-electric-vehicle-motors/21972> (accessed on 23 January 2022).
- [8] C. J. J. Labuschagne and M. J. Kamper, "Wind Generator Impedance Matching in Small-Scale Passive Wind Energy Systems," *IEEE Access*, vol. 9, pp. 22558-22568, 2021.
- [9] W. Liang and W. Liu, "Key technologies analysis of small scale non-grid-connected wind turbines: A review," *2010 World Non-Grid-Connected Wind Power and Energy Conference*, 2010, pp. 1-6.
- [10] L. B. K. Fisch and M. L. Heldwein, "10-MW Direct-Drive PMSG-Based Wind Energy Conversion System Model," *2020 IEEE 21st Workshop on Control and Modeling for Power Electronics (COMPEL)*, 2020, pp. 1-8.
- [11] W. Gul, Q. Gao and W. Lenwari, "Optimal Design of a 5-MW Double-Stator Single-Rotor PMSG for Offshore Direct Drive Wind Turbines," *IEEE Transactions on Industry Applications*, vol. 56, no. 1, pp. 216-225, 2020.

- [12] S. Tao, L. Zhao, Y. Liu and K. Liao, "Impedance Network Model of D-PMSG Based Wind Power Generation System Considering Wind Speed Variation for Sub-Synchronous Oscillation Analysis," *IEEE Access*, vol. 8, pp. 114784-114794, 2020.
- [13] S. Ye, D. Zhou, X. Yao and F. Blaabjerg, "Component-Level Reliability Assessment of a Direct-Drive PMSG Wind Power Converter Considering Two Terms of Thermal Cycles and the Parameter Sensitivity Analysis," *IEEE Transactions on Power Electronics*, vol. 36, no. 9, pp. 10037-10050, 2021.
- [14] H. Malik and A. Almutairi, "Modified Fuzzy-Q-Learning (MFQL)-Based Mechanical Fault Diagnosis for Direct-Drive Wind Turbines Using Electrical Signals," *IEEE Access*, vol. 9, pp. 52569-52579, 2021.
- [15] M. K. K. Prince, M. T. Arif, A. Gargoom, A. M. T. Oo and M. E. Haque, "Modeling, Parameter Measurement, and Control of PMSG-based Grid-connected Wind Energy Conversion System," *Journal of Modern Power Systems and Clean Energy*, vol. 9, no. 5, pp. 1054-1065, 2021.
- [16] G. Song, B. Cao and L. Chang, "An Electrical Stall Control Algorithm for Small-Scale Wind Generation System using Aerodynamic Observer," *2020 IEEE 11th International Symposium on Power Electronics for Distributed Generation Systems (PEDG)*, 2020, pp. 77-84.
- [17] L. Saihi and A. Boutera, "Robust control of a variable-speed wind turbine with fixed pitch angle and strategy MPPT control associated on a PMSG," *2016 8th International Conference on Modelling, Identification and Control (ICMIC)*, 2016, pp. 326-331.
- [18] J. M. Guerrero, C. Lumberras, D. D. Reigosa, P. Garcia and F. Briz, "Control and Emulation of Small Wind Turbines Using Torque Estimators," *IEEE Transactions on Industry Applications*, vol. 53, no. 5, pp. 4863-4876, 2017.
- [19] A. Shafiei, B. M. Dehkordi, A. Kiyomarsi and S. Farhangi, "A Control Approach for a Small-Scale PMSG-Based WECS in the Whole Wind Speed Range," *IEEE Transactions on Power Electronics*, vol. 32, no. 12, pp. 9117-9130, 2017.
- [20] G. J. Li, B. Ren, Z. Q. Zhu, Y. X. Li and J. Ma, "Cogging Torque Mitigation of Modular Permanent Magnet Machines," *IEEE Transactions on Magnetics*, vol. 52, no. 1, pp. 1-10, 2016.
- [21] E. Fleurot, F. Scuiller, and J. -F. Charpentier, "Analytical Models for Fast and Accurate Calculation of Electromagnetic Performances of Segmented Permanent Magnet Synchronous Machines with Large Angular Gaps," *Applied Sciences*, vol. 11, no. 1: 459, 2021.
- [22] G. Dajaku and D. Gerling, "Low costs and high-efficiency electric machines," *2012 2nd International Electric Drives Production Conference (EDPC)*, 2012, pp. 1-7.
- [23] G. J. Li, Z. Q. Zhu, M. Foster and D. Stone, "Comparative Studies of Modular and Unequal Tooth PM Machines Either with or Without Tooth Tips," *IEEE Transactions on Magnetics*, vol. 50, no. 7, pp. 1-10, 2014.

- [24] Y. Sui et al., "Multiphase Modular Fault-Tolerant Permanent-Magnet Machine With Hybrid Single/Double-Layer Fractional-Slot Concentrated Winding," *IEEE Transactions on Magnetics*, vol. 55, no. 9, pp. 1-6, 2019.
- [25] G. J. Li and Z. Q. Zhu, "Analytical Modeling of Modular and Unequal Tooth Width Surface-Mounted Permanent Magnet Machines," *IEEE Transactions on Magnetics*, vol. 51, no. 9, pp. 1-9, 2015.
- [26] W. Jara, I. Petrov, J. Tapia, P. Lindh and J. Pyrhönen, "Analytical model of tooth-coil winding permanent magnet synchronous machines with modular U-Shape stator," *2016 XXII International Conference on Electrical Machines (ICEM)*, 2016, pp. 145-151.
- [27] J. Rens, S. Jacobs, L. Vandenbossche and E. Attrazic, "Effect of Stator Segmentation and Manufacturing Degradation on the Performance of IPM Machines Using iCARE® Electrical Steels," *World Electric Vehicle Journal*, vol. 8, pp. 450-460, 2016.
- [28] G. -J. Li, Z. -Q. Zhu, M. P. Foster, D. A. Stone and H. -L. Zhan, "Modular Permanent-Magnet Machines with Alternate Teeth Having Tooth Tips," *IEEE Transactions on Industrial Electronics*, vol. 62, no. 10, pp. 6120-6130, 2015.
- [29] G. J. Li, B. Ren, Z. Q. Zhu, M. P. Foster and D. A. Stone, "Demagnetization Withstand Capability Enhancement of Surface Mounted PM Machines Using Stator Modularity," *IEEE Transactions on Industry Applications*, vol. 54, no. 2, pp. 1302-1311, 2018.
- [30] J. -X. Shen, S. Cai, J. Yuan, S. Cao and C. -W. Shi, "Cogging torque in SPM machine with segmented stator," *COMPEL – The international journal for computation and mathematics in electrical and electronic engineering*, vol. 35, no. 2, pp. 641-654, 2016.
- [31] D. Gonzalez-Jimenez, J. del-Olmo, J. Poza, F. Garramiola and P. Madina, "Data-Driven Fault Diagnosis for Electric Drives: A Review," *Sensors*, vol. 21: 4024, 2021.
- [32] C. Lumbreras, J. M. Guerrero, D. Fernandez, D. D. Reigosa, C. González-Moral and F. Briz, "Analysis and Control of the Inductorless Boost Rectifier for Small-Power Wind-Energy Converters," *IEEE Transactions on Industry Applications*, vol. 55, no. 1, pp. 689-700, 2019.
- [33] D. Micallef and G. Van Bussel, "A Review of Urban Wind Energy Research: Aerodynamics and Other Challenges," *Energies*, vol. 11, no. 9: 2204, 2018.
- [34] O. Rodriguez-Hernandez, M. Martinez, C. Lopez-Villalobos, H. Garcia and R. Campos-Amezcu, "Techno-Economic Feasibility Study of Small Wind Turbines in the Valley of Mexico Metropolitan Area," *Energies*, vol. 12, no. 5: 890, 2019.
- [35] M. Gough, M. Lotfi, R. Castro, A. Madhlopa, A. Khan and J. P.S. Catalão, "Urban Wind Resource Assessment: A Case Study on Cape Town," *Energies*, vol. 12, no. 8: 1479, 2019.
- [36] M. Elnaggar, E. Edwan and M. Ritter, "Wind Energy Potential of Gaza Using Small Wind Turbines: A Feasibility Study" *Energies*, vol. 10, no. 8: 1229, 2017.
- [37] J. L. Acosta, K. Combe, S. Ž. Djokic and I. Hernando-Gil, "Performance Assessment of Micro and Small-Scale Wind Turbines in Urban Areas," *IEEE Systems Journal*, vol. 6, no. 1, pp. 152-163, 2012.

- [38] L. Szabó, "A Survey on Modular Variable Reluctance Generators for Small Wind Turbines," *IEEE Transactions on Industry Applications*, vol. 55, no. 3, pp. 2548-2557, 2019.
- [39] M. Palmieri, S. Bozzella, G. L. Cascella, M. Bronzini, M. Torresi and F. Cupertino, "Wind Micro-Turbine Networks for Urban Areas: Optimal Design and Power Scalability of Permanent Magnet Generators," *Energies*, vol. 11, no. 10: 2759, 2018.
- [40] A. Shafiei, B. M. Dehkordi, S. Farhangi and A. Kiyoumarsı "Overall power control strategy for small-scale WECS incorporating flux weakening operation," *IET Renewable Power Generation*, vol. 10, no. 9, pp. 1264-1277, 2016.
- [41] R. A. Maher, A. K. Abdelsalam, Y. G. Dessouky, and A. Nouman, "High performance state-flow based MPPT technique for micro WECS," *IET Renewable Power Generation*, vol. 13, no. 16, pp. 3009-3021, 2019.
- [42] C. Lumbreras, J. M. Guerrero, P. García, F. Briz and D. D. Reigosa, "Control of a Small Wind Turbine in the High Wind Speed Region," *IEEE Transactions on Power Electronics*, vol. 31, no. 10, pp. 6980-6991, 2016.
- [43] J. Lee and Y. -S.Kim, "Sensorless fuzzy-logic-based maximum power point tracking control for a small-scale wind power generation systems with a switched-mode rectifier," *IET Renewable Power Generation*, vol.10, pp. 194-202, 2016.
- [44] J. Chen, J. Chen and C. Gong, "New Overall Power Control Strategy for Variable-Speed Fixed-Pitch Wind Turbines Within the Whole Wind Velocity Range," *IEEE Transactions on Industrial Electronics*, vol. 60, no. 7, pp. 2652-2660, 2013.
- [45] Z. M. Dalala, Z. U. Zahid and J. Lai, "New Overall Control Strategy for Small-Scale WECS in MPPT and Stall Regions with Mode Transfer Control," *IEEE Transactions on Energy Conversion*, vol. 28, no. 4, pp. 1082-1092, 2013.
- [46] J. C. Y. Hui, A. Bakhshai and P. K. Jain, "An Energy Management Scheme with Power Limit Capability and an Adaptive Maximum Power Point Tracking for Small Standalone PMSG Wind Energy Systems," *IEEE Transactions on Power Electronics*, vol. 31, no. 7, pp. 4861-4875, 2016.
- [47] X. Gong, X. Yang and W. Qiao, "Wind Speed and Rotor Position Sensorless Control for Direct-Drive PMG Wind Turbines," *2010 IEEE Industry Applications Society Annual Meeting*, 2010, pp. 1-8.
- [48] H. Liu, F. Locment and M. Sechilariu, "Experimental analysis of impact of maximum power point tracking methods on energy efficiency for small-scale wind energy conversion system, " *IET Renewable Power Generation*, vol. 11, no. 2, pp. 389-397, 2017.
- [49] I. Yazıcı, and E. K. Yaylacı, "Discrete-time integral terminal sliding mode based maximum power point controller for the PMSG-based wind energy system," *IET Power Electronics*, vol. 12, no. 14, pp. 3688-3696, 2019.
- [50] H. Zhao, Q. Wu, C.N. Rasmussen, and M. Blanke, "L1 Adaptive Speed Control of a Small Wind Energy Conversion System for Maximum Power Point Tracking," *IEEE Transaction on Energy Conversion*, vol. 29, pp. 576-584, 2014.

- [51] S. A. M. Saleh, "Testing the Performance of a Resolution-Level MPPT Controller for PMG-Based Wind Energy Conversion Systems," *IEEE Transactions on Industry Applications*, vol. 53, no. 3, pp. 2526-2540, 2017.
- [52] J. Chen, T. Lin, C. Wen and Y. Song, "Design of a Unified Power Controller for Variable-Speed Fixed-Pitch Wind Energy Conversion System," *IEEE Transactions on Industrial Electronics*, vol. 63, no. 8, pp. 4899-4908, 2016.
- [53] İ. Yazici, and E. K. Yaylaci, "Maximum power point tracking for the permanent magnet synchronous generator-based WECS by using the discrete-time integral sliding mode controller with a chattering-free reaching law," *IET Power Electronics*, vol. 10, pp. 1751-1758, 2017.
- [54] N. A. Orlando, M. Liserre, V. G. Monopoli and A. Dell'Aquila, "Speed sensorless control of a PMSG for small wind turbine systems," *2009 IEEE International Symposium on Industrial Electronics*, 2009, pp. 1540-1545.
- [55] Z. Zhang, Y. Zhao, W. Qiao and L. Qu, "A Space-Vector-Modulated Sensorless Direct-Torque Control for Direct-Drive PMSG Wind Turbines," *IEEE Transactions on Industry Applications*, vol. 50, no. 4, pp. 2331-2341, 2014.
- [56] S. Nouali and A. Ouali, "Multi-Layer neural network for sensorless MPPT control for Wind Energy Conversion System using Doubly Fed Twin Stator Induction Generator," *Eighth International Multi-Conference on Systems, Signals & Devices*, 2011, pp. 1-7.
- [57] J. Hussain and M. K. Mishra, "An Efficient Wind Speed Computation Method Using Sliding Mode Observers in Wind Energy Conversion System Control Applications," *IEEE Transactions on Industry Applications*, vol. 56, no. 1, pp. 730-739, 2020.
- [58] M. A. S. Ali, K. K. Mehmood, S. Baloch and C. H. Kim, "Wind-Speed Estimation and Sensorless Control for SPMSG-Based WECS Using LMI-Based SMC," *IEEE Access*, vol. 8, pp. 26524–26535, 2020.
- [59] D. -Y. Li, W. -C. Cai, P. Li, Z. -J. Jia, H. -J. Chen and Y. -D. Song, "Neuroadaptive Variable Speed Control of Wind Turbine with Wind Speed Estimation," *IEEE Transactions on Industrial Electronics*, vol. 63, no. 12, pp. 7754-7764, 2016.
- [60] T. D. Do, "Disturbance Observer-Based Fuzzy SMC of WECSs Without Wind Speed Measurement," *IEEE Access*, vol. 5, pp. 147-155, 2017.
- [61] M. L. Corradini, G. Ippoliti and G. Orlando, "Robust Control of Variable-Speed Wind Turbines Based on an Aerodynamic Torque Observer," *IEEE Transactions on Control Systems Technology*, vol. 21, no. 4, pp. 1199-1206, 2013.
- [62] A. Merabet, "Adaptive Sliding Mode Speed Control for Wind Energy Experimental System," *Energies*, vol. 11, no. 9: 2238, 2018.
- [63] A. Martyanov, N. Martyanov and E. Sirotkin, "State Observer for Variable Speed Wind Turbine," *2018 International Ural Conference on Green Energy (UralCon)*, 2018, pp. 97-100.
- [64] H. Liu, F. Locment and M. Sechilariu, "Integrated Control for Small Power Wind Generator," *Energies*, vol. 11, no. 5: 1217, 2018.

- [65] J. C. Y. Hui, A. Bakhshai and P. K. Jain, "A Sensorless Adaptive Maximum Power Point Extraction Method with Voltage Feedback Control for Small Wind Turbines in Off-Grid Applications," *IEEE Journal of Emerging and Selected Topics in Power Electronics*, vol. 3, no. 3, pp. 817-828, 2015.
- [66] R. Syahputra and I. Soesanti. "Performance Improvement for Small-Scale Wind Turbine System Based on Maximum Power Point Tracking Control." *Energies*, vol. 12, no. 20: 3938, 2019.
- [67] M. Nasir Uddin and N. Patel, "Maximum Power Point Tracking Control of IPMSG Incorporating Loss Minimization and Speed Sensorless Schemes for Wind Energy System," *IEEE Transactions on Industry Applications*, vol. 52, no. 2, pp. 1902-1912, 2016.
- [68] C. Wei, Z. Zhang, W. Qiao and L. Qu, "An Adaptive Network-Based Reinforcement Learning Method for MPPT Control of PMSG Wind Energy Conversion Systems," *IEEE Transactions on Power Electronics*, vol. 31, no. 11, pp. 7837-7848, 2016.
- [69] J. S. L. Senanayaka, H. R. Karimi and K. G. Robbersmyr, "A novel soft-stall power control for a small wind turbine," *2017 IEEE 26th International Symposium on Industrial Electronics (ISIE)*, 2017, pp. 940-94.
- [70] C. Jiawei, W. Changyun and S. Yongduan, "Power control strategy for variable-speed fixed-pitch wind turbines," *2014 13th International Conference on Control Automation Robotics & Vision (ICARCV)*, 2014, pp. 559-564.
- [71] S. Morimoto, H. Nakayama, M. Sanada and Y. Takeda, "Sensorless output maximization control for variable-speed wind generation system using IPMSG," *IEEE Transactions on Industry Applications*, vol. 41, no. 1, pp. 60-67, 2005.
- [72] Y. -F. Wang, L. Yang, C. -S. Wang, W. Li, W. Qie and S. -J. Tu, "High Step-Up 3-Phase Rectifier with Fly-Back Cells and Switched Capacitors for Small-Scaled Wind Generation Systems," *Energies*, vol. 8, no. 4, pp. 2742-2768, 2015.
- [73] M. Werle and W. Presz, "Ducted Wind/Water Turbines and Propellers Revisited," *Journal of Propulsion and Power*, vol. 24, pp. 1146–1150, 2008.
- [74] M. Torresi, N. Postiglione, P. F. Filianoti, B. Fortunato and S. M. Camporeale, "Design of a ducted wind turbine for offshore floating platforms," *Wind Engineering*, vol. 40, pp. 468–474, 2016.
- [75] T.A Khamlaj and M. P. Rumpfkeil, "Analysis and optimization of ducted wind turbines," *Energy*, vol. 162, pp. 1234–1252, 2018.
- [76] A. Grant, C. Johnstone and N. Kelly, "Urban wind energy conversion: The potential of ducted turbines. Renew," *Energy*, vol. 33, pp. 1157–1163, 2008.
- [77] B. M. Wilamowski and H. Yu, "Improved Computation for Levenberg–Marquardt Training," in *IEEE Transactions on Neural Networks*, vol. 21, no. 6, pp. 930-937, 2010.
- [78] X. Qian, H. Huang, X. Chen and T. Huang, "Generalized Hybrid Constructive Learning Algorithm for Multioutput RBF Networks," *IEEE Transactions on Cybernetics*, vol. 47, pp. 3634–3648, 2017.

- [79] D. Calabrese, G. Tricarico, E. Brescia, G. L. Cascella, V. G. Monopoli and F. Cupertino, "Variable Structure Control of a Small Ducted Wind Turbine in the Whole Wind Speed Range Using a Luenberger Observer," *Energies*, vol. 13, no.18: 4647, 2020.
- [80] F. Libert and J. Soulard, "Manufacturing Methods of Stator Cores with Concentrated Windings," *2006 3rd IET International Conference on Power Electronics, Machines and Drives - PEMD 2006*, 2006, pp. 676-680.
- [81] J. Brettschneider, R. Spitzner and R. Boehm, "Flexible mass production concept for segmented BLDC stators," *2013 3rd International Electric Drives Production Conference (EDPC)*, 2013, pp. 1-8.
- [82] J. Yuan, C. Shi and J. Shen, "Analysis of cogging torque in surface-mounted permanent magnet machines with segmented stators," *2014 17th International Conference on Electrical Machines and Systems (ICEMS)*, 2014, pp. 2513-2516.
- [83] X. Ge, Z. Q. Zhu, G. Kemp, D. Moule and C. Williams, "Optimal Step-Skew Methods for Cogging Torque Reduction Accounting for Three-Dimensional Effect of Interior Permanent Magnet Machines," *IEEE Transactions on Energy Conversion*, vol. 32, no. 1, pp. 222-232, 2017.
- [84] M. G. Angle, J. H. Lang, J. L. Kirtley, S. Kim and D. Otten, "Cogging torque reduction in permanent-magnet synchronous machines with skew," *2016 XXII International Conference on Electrical Machines (ICEM)*, 2016, pp. 207-211.
- [85] G. Zhao, W. Hua, X. Zhu and G. Zhang, "The Influence of Dummy Slots on Stator Surface-Mounted Permanent Magnet Machines," *IEEE Transactions on Magnetics*, vol. 53, no. 6, pp. 1-5, 2017.
- [86] H. Yu, B. Yu, J. Yu and C. Lin, "A Dual Notched Design of Radial-Flux Permanent Magnet Motors with Low Cogging Torque and Rare Earth Material," *IEEE Transactions on Magnetics*, vol. 50, no. 11, pp. 1-4, 2014.
- [87] D. Wu and Z. Q. Zhu, "Design Tradeoff Between Cogging Torque and Torque Ripple in Fractional Slot Surface-Mounted Permanent Magnet Machines," *IEEE Transactions on Magnetics*, vol. 51, no. 11, pp. 1-4, 2015.
- [88] S.-M. Hwang, J. -B. Eom, G. -B. Hwang, W. -B. Jeong and Y. -H. Jung, "Cogging torque and acoustic noise reduction in permanent magnet motors by teeth pairing," *IEEE Transactions on Magnetics*, vol. 36, no. 5, pp. 3144-3146, 2000.
- [89] A. R. Pramurti and O. Y. Hutajulu, "The Design of Radial Flux Permanent Magnet Generator on Low Speed Wind Turbine to Reduce Cogging Torque," *2018 Electrical Power, Electronics, Communications, Controls and Informatics Seminar (EECCIS)*, 2018, pp. 68-72.
- [90] Z. Q. Zhu, Z. Azar and G. Ombach, "Influence of Additional Air Gaps Between Stator Segments on Cogging Torque of Permanent-Magnet Machines Having Modular Stators," *IEEE Transactions on Magnetics*, vol. 48, no. 6, pp. 2049-2055, 2012.
- [91] K. -J. Han, H. -S. Cho, D. -H. Cho and H. -K. Jung, "Optimal core shape design for cogging torque reduction of brushless DC motor using genetic algorithm," *IEEE Transactions on Magnetics*, vol. 36, no. 4, pp. 1927-1931, 2000.

- [92] S. Ruangsinchaiwanich, Z. Q. Zhu and D. Howe, "Influence of magnet shape on cogging torque and back-emf waveform in permanent magnet machines," *2005 International Conference on Electrical Machines and Systems*, 2005, pp. 284-289.
- [93] B. Ladghem-Chikouche, K. Boughrara, and R. Ibtouen, "Cogging Torque Minimization of Surface-Mounted Permanent Magnet Synchronous Machines Using Hybrid Magnet Shapes," *Progress In Electromagnetics Research B*, vol. 62, pp. 49-61, 2015.
- [94] M. Flankl, A. Tüysüz and J. W. Kolar, "Cogging Torque Shape Optimization of an Integrated Generator for Electromechanical Energy Harvesting," *IEEE Transactions on Industrial Electronics*, vol. 64, no. 12, pp. 9806-9814, 2017.
- [95] S. L. Ho, N. Chen and W. N. Fu, "An Optimal Design Method for the Minimization of Cogging Torques of a Permanent Magnet Motor Using FEM and Genetic Algorithm," *IEEE Transactions on Applied Superconductivity*, vol. 20, no. 3, pp. 861-864, 2010.
- [96] Y. Park, J. Cho and D. Kim, "Cogging Torque Reduction of Single-Phase Brushless DC Motor with a Tapered Air-Gap Using Optimizing Notch Size and Position," *IEEE Transactions on Industry Applications*, vol. 51, no. 6, pp. 4455-4463, 2015.
- [97] D. Lee, S. Lee, J. -W. Kim, C. -G. Lee and S. -Y. Jung, "Intelligent Memetic Algorithm Using GA and Guided MADS for the Optimal Design of Interior PM Synchronous Machine," *IEEE Transactions on Magnetics*, vol. 47, no. 5, pp. 1230-1233, 2011.
- [98] S. Barmada, N. Fontana, L. Sani, D. Thomopoulos and M. Tucci, "Deep Learning and Reduced Models for Fast Optimization in Electromagnetics," *IEEE Transactions on Magnetics*, vol. 56, no. 3, pp. 1-4, 2020.
- [99] M. H. Mohammadi, T. Rahman, R. Silva, M. Li and D. A. Lowther, "A Computationally Efficient Algorithm for Rotor Design Optimization of Synchronous Reluctance Machines," *IEEE Transactions on Magnetics*, vol. 52, no. 3, pp. 1-4, 2016.
- [100] Y. Yang, N. Bianchi, G. Bramerdorfer, C. Zhang and S. Zhang, "Methods to Improve the Cogging Torque Robustness Under Manufacturing Tolerances for the Permanent Magnet Synchronous Machine," *IEEE Transactions on Energy Conversion*, vol. 36, no. 3, pp. 2152-2162, 2021.
- [101] Y. Yang, N. Bianchi, C. Zhang, X. Zhu, H. Liu and S. Zhang, "A Method for Evaluating the Worst-Case Cogging Torque Under Manufacturing Uncertainties," *IEEE Transactions on Energy Conversion*, vol. 35, no. 4, pp. 1837-1848, 2020.
- [102] G. Dajaku and D. Gerling, "Stator Slotting Effect on the Magnetic Field Distribution of Salient Pole Synchronous Permanent-Magnet Machines," *IEEE Transactions on Magnetics*, vol. 46, no. 9, pp. 3676-3683, 2010.
- [103] L. Gašparin A. Černigoj and R. Fišer, "Additional cogging torque components due to asymmetry in stator back iron of PM synchronous motors," *COMPEL - The international journal for computation and mathematics in electrical and electronic engineering*, vol. 30, no. 3, pp. 894-905, 2011.
- [104] Y. Yang, X. Wang, R. Zhang, T. Ding and R. Tang, "The optimization of pole arc coefficient to reduce cogging torque in surface-mounted permanent magnet motors," *IEEE Transactions on Magnetics*, vol. 42, no. 4, pp. 1135-1138, 2006.

- [105] Z. Q. Zhu and D. Howe, "Instantaneous magnetic field distribution in brushless permanent magnet DC motors. III. Effect of stator slotting," *IEEE Transactions on Magnetics*, vol. 29, no. 1, pp. 143-151, Jan. 1993.
- [106] B. Ackermann, J.H.H. Janssen, R. Sottek and R.I. van Steen, "New technique for reducing cogging torque in a class of brushless DC motors," *IEEE Proc. B Electr. Power Appl.*, 1992, pp. 315–320.
- [107] Y. -K. Kim, J. -P. Hong and J. Hur, "Torque characteristic analysis considering the manufacturing tolerance for electric machine by stochastic response surface method," *IEEE Transactions on Industry Applications*, vol. 39, no. 3, pp. 713-719, 2003.
- [108] M. Torresi, N. Postiglione, P. F. Filianoti, B. Fortunato and S. M. Camporeale, "Design of a ducted wind turbine for offshore floating platforms," *Wind Engineering*, vol. 40, no. 5, pp. 468–47, 2016.
- [109] E. Brescia, D. Costantino, P. R. Massenio, V. G. Monopoli, F. Cupertino and G. L. Cascella, "A Design Method for the Cogging Torque Minimization of Permanent Magnet Machines with a Segmented Stator Core Based on ANN Surrogate Models," *Energies*, vol. 14, no. 7: 1880, 2021.
- [110] E. Brescia, M. Palmieri, G. L. Cascella and F. Cupertino, "Optimal Tooth Tips Design for Cogging Torque Suppression of Permanent Magnet Machines with a Segmented Stator Core," *2020 International Conference on Electrical Machines (ICEM)*, 2020, pp. 1930-1936.
- [111] K. Liu and Z. Q. Zhu, "Position-offset-based parameter estimation using the adaline nn for condition monitoring of permanent-magnet synchronous machines," *IEEE Transactions on Industrial Electronics*, vol. 62, no. 4, pp. 2372–2383, 2015.
- [112] Z. -H. Liu, H. -L. Wei, X. -H. Li, K. Liu, and Q.-C. Zhong, "Global identification of electrical and mechanical parameters in pmsm drive based on dynamic self-learning pso," *IEEE Transactions on Power Electronics*, vol. 33, no. 12, pp. 10 858–10 871, 2018.
- [113] K. M. S. Rafiq and J. -W. Jung, "A comprehensive review of state-of-the-art parameter estimation techniques for permanent magnet synchronous motors in wide speed range," *IEEE Transactions on Industrial Informatics*, vol. 16, no. 7, pp. 4747–4758, 2020.
- [114] Z. Q. Zhu, D. Liang and K. Liu, "Online parameter estimation for permanent magnet synchronous machines: An overview," *IEEE Access*, vol. 9, pp. 59 059–59 084, 2021.
- [115] K. Liu, Z. Q. Zhu and D. A. Stone, "Parameter estimation for condition monitoring of pmsm stator winding and rotor permanent magnets," *IEEE Transactions on Industrial Electronics*, vol. 60, no. 12, pp. 5902–5913, 2013.
- [116] K. Liu, Q. Zhang, J. Chen, Z. Q. Zhu and J. Zhang, "Online multiparameter estimation of nonsalient-pole pm synchronous machines with temperature variation tracking," *IEEE Transactions on Industrial Electronics*, vol. 58, no. 5, pp. 1776–1788, 2011.

- [117] Z. Li, G. Feng, C. Lai, D. Banerjee, W. Li and N. C. Kar, "Current injection-based multi-parameter estimation for dual three-phase ipmsm considering vsr nonlinearity," *IEEE Transactions on Transportation Electrification*, vol. 5, no. 2, pp. 405–415, 2019.
- [118] G. Feng, C. Lai, K. Mukherjee and N. C. Kar, "Current injection-based online parameter and vsr nonlinearity estimation for pmsm drives using current and voltage dc components," *IEEE Transactions on Transportation Electrification*, vol. 2, no. 2, pp. 119–128, 2016.
- [119] K. Liu and Z. Q. Zhu, "Quantum genetic algorithm-based parameter estimation of pmsm under variable speed control accounting for system identifiability and vsr nonlinearity," *IEEE Transactions on Industrial Electronics*, vol. 62, no. 4, pp. 2363–2371, 2015.
- [120] K. Liu and Z. Q. Zhu, "Position offset-based parameter estimation for permanent magnet synchronous machines under variable speed control," *IEEE Transactions on Power Electronics*, vol. 30, no. 6, pp. 3438–3446, 2015.
- [121] Z. -H. Liu, J. Zhang, S. -W. Zhou, X. -H. Li and K. Liu, "Coevolutionary particle swarm optimization using ais and its application in multiparameter estimation of pmsm," *IEEE Transactions on Cybernetics*, vol. 43, no. 6, pp. 1921–1935, 2013.
- [122] T. Boileau, N. Leboeuf, B. Nahid-Mobarakeh and F. Meibody-Tabar, "Online identification of pmsm parameters: Parameter identifiability and estimator comparative study," *IEEE Transactions on Industry Applications*, vol. 47, no. 4, pp. 1944–1957, 2011.
- [123] Y. Shi, K. Sun, L. Huang and Y. Li, "Online identification of permanent magnet flux based on extended kalman filter for ipmsm drive with position sensorless control," *IEEE Transactions on Industrial Electronics*, vol. 59, no. 11, pp. 4169–4178, 2012.
- [124] O. C. Kivanc and S. B. Ozturk, "Sensorless pmsm drive based on stator feedforward voltage estimation improved with mras multiparameter estimation," *IEEE/ASME Transactions on Mechatronics*, vol. 23, no. 3, pp. 1326–1337, 2018.
- [125] M. A. Hamida, J. De Leon, A. Glumineau and R. Boisliveau, "An adaptive interconnected observer for sensorless control of pm synchronous motors with online parameter identification," *IEEE Transactions on Industrial Electronics*, vol. 60, no. 2, pp. 739–748, 2013.
- [126] R. Tami, D. Boutat, G. Zheng, F. Kratz and R. E. Gouri, "Rotor speed, load torque and parameters estimations of a permanent magnet synchronous motor using extended observer forms," *IET Control Theory Applications*, vol. 11, pp. 1485–1492, 2017.
- [127] X. Xiao, C. Chen and M. Zhang, "Dynamic permanent magnet flux estimation of permanent magnet synchronous machines," *IEEE Transactions on Applied Superconductivity*, vol. 20, no. 3, pp. 1085–1088, 2010.
- [128] K. Liu and Z. Q. Zhu, "Online estimation of the rotor flux linkage and voltage-source inverter nonlinearity in permanent magnet synchronous machine drives," *IEEE Transactions on Power Electronics*, vol. 29, no. 1, pp. 418–427, 2014.

- [129] B. Stumberger, B. Kreca and B. Hribernik, "Determination of parameters of synchronous motor with permanent magnets from measurement of load conditions," *IEEE Transactions on Energy Conversion*, vol. 14, no. 4, pp. 1413–1416, 1999.
- [130] C. Lai, G. Feng, K. Mukherjee, V. Loukanov and N. C. Kar, "Torque ripple minimization for interior pmsm with consideration of magnetic saturation incorporating online parameter identification," *IEEE Transactions on Magnetics*, vol. 53, no. 6, pp. 1–4, 2017.
- [131] S. D. Wilson, P. Stewart and B. P. Taylor, "Methods of resistance estimation in permanent magnet synchronous motors for real-time thermal management," *IEEE Transactions on Energy Conversion*, vol. 25, no. 3, pp. 698–707, 2010.
- [132] H. -W. Kim, M. -J. Youn, K. -Y. Cho and H. -S. Kim, "Nonlinearity estimation and compensation of pwm vsf for pmsm under resistance and flux linkage uncertainty," *IEEE Transactions on Control Systems Technology*, vol. 14, no. 4, pp. 589–601, 2006.
- [133] H. -S. Kim, K. -H. Kim and M. -J. Youn, "On-line dead-time compensation method based on time delay control," *IEEE Transactions on Control Systems Technology*, vol. 11, no. 2, pp. 279–285, 2003.
- [134] J.-W. Choi and S.-K. Sul, "Inverter output voltage synthesis using novel dead time compensation," *IEEE Transactions on Power Electronics*, vol. 11, no. 2, pp. 221–227, 1996.
- [135] K. Liu, Z. Q. Zhu, Q. Zhang and J. Zhang, "Influence of nonideal voltage measurement on parameter estimation in permanent-magnet synchronous machines," *IEEE Transactions on Industrial Electronics*, vol. 59, no. 6, pp. 2438–2447, 2012.
- [136] B. -H. Bae and S. -K. Sul, "A compensation method for time delay of full-digital synchronous frame current regulator of pwm ac drives," *IEEE Transactions on Industry Applications*, vol. 39, no. 3, pp. 802–810, 2003.
- [137] R. Pena-Alzola, M. Liserre, F. Blaabjerg, R. Sebastián, J. Dannehl and F. W. Fuchs, "Analysis of the passive damping losses in lcl-filter-based grid converters," *IEEE Transactions on Power Electronics*, vol. 28, no. 6, pp. 2642–2646, 2013.
- [138] E. Brescia, D. Costantino, F. Marzo, P. R. Massenio, G. L. Cascella and D. Naso, "Automated Multistep Parameter Identification of SPMSMs in Large-Scale Applications Using Cloud Computing Resources," *Sensors*, vol. 21, no. 14: 4699, 2021.
- [139] R. R. Rhinehart, "Automated steady and transient state identification in noisy processes," *2013 American Control Conference*, 2013, pp. 4477–4493.
- [140] H. Hämäläinen, J. Pyrhönen and J. Nerg, "AC Resistance Factor in One-Layer Form-Wound Winding Used in Rotating Electrical Machines," *IEEE Transactions on Magnetics*, vol. 49, no. 6, pp. 2967–2973, 2013.
- [141] Y. Wang, J. Pries, K. Zhou, H. Hofmann and D. Rizzo, "Computationally Efficient AC Resistance Model for Stator Winding with Rectangular Conductors," *IEEE Transactions on Magnetics*, vol. 56, no. 4, pp. 1–9, 2020.

- [142] S. Nalakath, M. Preindl, B. Bilgin, B. Cheng and A. Emadi, "Modeling and analysis of AC resistance of a permanent magnet machine for online estimation purposes," *2015 IEEE Energy Conversion Congress and Exposition (ECCE)*, 2015, pp. 314-319.
- [143] S. Xu and H. Ren, "Analytical Computation for AC Resistance and Reactance of Electric Machine Windings in Ferromagnetic Slots," *IEEE Transactions on Energy Conversion*, vol. 33, no. 4, pp. 1855-1864, 2018.
- [144] N. Voyer, G. Bueno-Mariani, A. Besri, V. Quemener, Y. Okamoto and A. Satake, "High Frequency Modelling of Permanent Magnet Synchronous Machine," *2018 8th International Electric Drives Production Conference (EDPC)*, 2018, pp. 1-6.
- [145] D. Costantino, E. Brescia, P. R. Massenio, P. Serafino, G. L. Cascella and F. Cupertino, "SuMRAS: a new SPMSM Parameter Identification in Cloud Computing Environment," *2021 IEEE Workshop on Electrical Machines Design, Control and Diagnosis (WEMDCD)*, 2021, pp. 297-302.
- [146] E. Brescia, P. Serafino, D. Cascella, G. Comitangelo, G. Conte and L. Chieco, "Automated Parameter Identification of SPMSMs Based on Two Steady States Using Cloud Computing Resources," *2021 International Conference on Electrical, Computer and Energy Technologies (ICECET)*, 2021.